Universidad Pontificia Comillas de Madrid
Escuela Técnica Superior de Ingeniería (ICAI)

Instituto de Investigación Tecnológica (IIT)

Control of grid-forming VSC-based generators to improve transient stability in power systems with 100 % non-synchronous generation

Thesis submitted for the Degree of Doctor (PhD) on Power Systems

Author: Régulo Enrique Ávila Martínez

Supervisors: Dr. Francisco Javier Renedo Anglada
Prof. Dr. Luis Rouco Rodríguez

February 2, 2024

Madrid, Spain

Summary

The aim of this thesis is to investigate supplementary control strategies in Grid-forming voltage source converters (GFM-VSCs) to improve transient stability in power systems with 100% non-synchronous generation.

The motivation behind this study is to address the challenges associated with integrating renewable energy sources into power systems, leading to a higher presence of non-synchronous generators. With the increasing integration of non-synchronous generation sources such as wind and solar, stability becomes challenging due to the fast dynamics of the voltage source converters (VSCs) connecting non-synchronous sources to the grid. These generators have different characteristics compared to traditional synchronous generators, which can affect the stability of power systems. As more renewable energy sources are integrated into the grid, the overall inertia of the system decreases, significantly affecting the system's stability. This scenario poses a significant challenge to power system stability, particularly transient stability. Thus, there is a need to adapt to this changing landscape to ensure grid stability. The study aims to contribute to understanding the analysis of the transient stability improvement in electrical power systems with 100% non-synchronous generation, providing valuable insights for control of GFM-VSCs in future power systems.

The use of GFM-VSCs in these types of systems creates a need for control strategies that can improve transient stability. Therefore, this thesis aims to address this need by analysing the transient stability of power systems with 100% non-synchronous generation and proposing control strategies based on active- and voltage/reactive-power control in GFM-VSCs for transient stability improvement.

This thesis compares various self-synchronisation mechanisms of GFM-VSCs under different scenarios, analysing their impact on transient stability. Moreover, two proposed Fast Voltage Booster (FVB) strategies based on voltage/reactive-power controls aim to enhance transient stability by ad-

justing the voltage set-point without significant changes to primary energy source set-points. One control strategy (FVB-L) uses local measurements, while the other (FVB-WACS) uses global measurements of the frequency of the center of inertia (COI). The thesis also analyses the impact of FVBs when employing different current limiters (current saturation algorithms and hybrid current limiters) in GFM-VSC-based generators. Additionally, a local active-power control strategy (TSP-L) is introduced and compared with two existing control strategies from the literature, aiming to further improve transient stability in power systems with 100% non-synchronous generators.

The proposed strategies provide valuable insights for control of GFM-VSCs in future power systems. By addressing this issue, this research hopes to contribute to the development of more stable and reliable power systems, which are essential for the transition towards a sustainable energy future.

Agradecimientos

Quiero expresar mi más profundo agradecimiento a mis directores de tesis, el Dr. Javier Renedo Anglada y el Prof. Dr. Luis Rouco Rodríguez, por su guía constante, dirección, paciencia y dedicación a lo largo de este extenso trabajo. Al Dr. Javier Renedo, sin cuya orientación, ayuda persistente y paciencia esta tesis no habría sido posible. Sus oportunos comentarios y sugerencias, junto con su dedicación, han contribuido significativamente a mejorar la calidad de este trabajo. Al Prof. Dr. Luis Rouco, agradezco su paciencia y dedicación, así como las revisiones sobre el documento cuyos comentarios han sido fundamentales para la finalización de esta tesis. Realmente es un honor contar con su supervisión. Las valiosas sugerencias y comentarios proporcionados por ambos han sido esenciales para el desarrollo y la conclusión exitosa de esta tesis doctoral. Sin su constancia, conocimientos y confianza en mí, no habría sido posible finalizar este proyecto.

Al Prof. Dr. Aurelio García Cerrada por su atención a los avances de la tesis y por sus comentarios oportunos en sistemas de control. También, al Dr. Lukas Sigrist por su valiosa ayuda y consejo en momentos cruciales.

Al Prof. Dr. Xavier Guillaud por abrirme las puertas de L2EP en Lille, Francia, y cuya rigurosidad profundizó aún más mis conocimientos en convertidores electrónicos de potencia. Agradezco al Dr. Taoufik Qoria, cuyos comentarios y aportes han enriquecido significativamente el contenido de esta tesis.

A los Dres. Enrique Lobato, Francisco Echevarren e Ignacio Egido por sus comentarios constructivos sobre el manuscrito.

A Javier García Aguilar por la gran ayuda brindada con Matlab en las primeras etapas del doctorado, así como el apoyo y comentarios oportunos de Andrés Tomas en temas relacionados con Matlab y Simulink.

Al Dr. Javier Roldan, amigo y mentor, con quien di mis primeros pasos en la investigación y por su inspiración y motivación para embarcarme en este gran viaje de doctorado.

A Christopher Turner por sus grandes consejos y sugerencias en la redacción del inglés académico, ya que han sido de gran utilidad en la elaboración de este trabajo.

A Isabel Tamudo, Cristina Ruiz y Guillermina Vazquez por su incondicional ayuda durante mi proceso de estancia.

A mis actuales compañeros y amigos del IIT, por los momentos compartidos y la amistad forjada en este corto tiempo.

Agradezco al Instituto de Investigación Tecnológica (IIT) perteneciente a la Escuela Técnica Superior de Ingeniería (ETSI-ICAI) de la prestigiosa Universidad Pontificia Comillas de Madrid, por abrirme sus puertas y brindarme la oportunidad de seguir desarrollando mi formación profesional y personal.

Mi más sincero agradecimiento a mis padres, Cruz y Régulo, pilares fundamentales de mi vida, por su amor incondicional. Agradezco especialmente por cuidar a Diego durante las horas dedicadas a mi tesis. Son, sin duda, los mejores padres.

A mi hermano Regulito y a mi cuñada Ana por su constante apoyo y paciencia a lo largo de estos años. Sin ellos, esta meta no sería posible. A mi hermana Erlinda por su apoyo durante este proceso.

A mi sobrino Juan, un hermano más, por su gran apoyo incondicional durante este tiempo, especialmente en los inicios de esta gran aventura.

A mi amado hijo Diego, quien con su amor y cariño da sentido a cada paso que doy en esta travesía académica.

A mis amados sobrinos-hijos, Santiago y Nicolás, pequeños ángeles que llegaron para alegrar los días de nuestra familia.

Al amor de mi vida, Rosa, gracias por tu paciencia y tu ayuda en las correcciones y comentarios sobre el documento de la tesis. Sin tu apoyo, esta meta tampoco hubiera sido posible.

Finalmente, deseo expresar mi agradecimiento al Ministerio de Ciencia e Innovación (MCI), la Agencia Estatal de Investigación (AEI) y el Fondo Europeo de Desarrollo Regional (FEDER), por la financiación del proyecto que respaldó esta tesis doctoral:

- Ayuda predoctoral PRE2019-088084 financiada por MCIN/ AEI/ 10. 13039/ 501100011033 y por FSE invierte en tu futuro.

- Modelado, tecnologías, control y operación de redes eléctricas híbridas (CA/CC) con poca o nula generación síncrona convencional y fuerte penetración de renovables (ref. RTI2018-098865-B-C31), MCIN/AEI/ 10.13039/501100011033/ y por FEDER Una manera de hacer Europa.

Y a la Comunidad de Madrid, por la financiación del proyecto que ha apoyado a nuestro equipo de trabajo en temas afines a esta tesis dando lugar a interesantes discusiones:

- Programa Microrredes Inteligentes Comunidad de Madrid (PROMINT-CM) (ref. S2018/EMT-4366), financiado por la Comunidad de Madrid, España.

Adicionalmente, agradezco nuevamente al Instituto de Investigación Tecnológica (IIT) de la ETSI ICAI, Universidad Pontifica Comillas por haber financiado el desarrollo de esta tesis doctoral durante mi primer año :

- Programa de líneas de investigación estrategias del IIT.

Contents

List of Tables

List of Figures

Acronyms

CCT: Critical Clearing Time.

CIG: Converter-Interfaced Generation.

CL: Current Limiter.

COI: Center Of Inertia.

CSA: Current Saturation Algorithm.

DFIG: Double Feed Induction Generator.

EB: Excitation Booster.

ESS: Energy Storage System.

FACTS: Flexible alternating current transmission system.

FRT: Fault Ride Through.

FVB: Fast Voltage Boosters strategy based on Voltage/Reactive-Power droop control.

FVB-L: Local Fast Voltage Boosters control strategy.

FVB-WACS: Fast Voltage Boosters using a Wide-Area Control System.

GFL-VSC: Grid-Following Voltage Source Converter.

GFM-VSC: Grid-Forming Voltage Source Converter.

HCL: Hybrid Current Limiter.

HPF: High-Pass Filter.

HVDC: High voltage direct current.

IP controller: Integral-Proportional controller.

LPF: Low-Pass Filter.

PCC: Point of Common Coupling.

PFC: Primary Frequency Controller.

PLL: Phase-Locked Loop.

Q-V: Voltage/Reactive-Power droop control.

TSP: Active-Power control strategy for Transient Stability.

TSP-L: Local Active-Power control strategy.

TSP-TDM: Local Active-Power control strategy using Transient Damping Method.

TSP-WACS: Active-power control strategy using a Wide-Area Control System.

TSO: Transmission System Operator.

VAPC: Virtual Active Power Control.

VI-CL: Virtual Impedance-based Current Limiter.

VSC: Voltage Source Converter.

VSM: Virtual Synchronous Machine.

List of Symbols

GFM-VSC connected via L-filter

Symbol	Description
$\bar{e}_{m,i}$	Modulated voltage magnitude (pu)
$\bar{e}_{m,i}^{ref'0}$	Modulated voltage set-points (pu)
$\bar{e}_{m,i}^{0}$	Initial operation set-points of modulated Voltage (pu)
$\bar{m}_i$	Modulation index
m_i^{max}	Maximun modulation index
$v_{dc,i}$	DC voltage of the bus DC-link (pu)
$V_{dc,B}$	DC voltage base value (pole to pole) (V)
$V_{ac,B}$	AC voltage base value (phase to phase) (V)
$\bar{v}_{g,i}$	Voltage magnitude at the bus g (pu)
$\bar{v}_{e,i}$	Voltage magnitude of the infinite grid (pu)
$\bar{i}_{g,i}$	Output current (pu)
$\bar{i}_{g,i}^{ref'}$	Unsaturated current set-point (pu)
$\bar{i}_{g,i}^{ref}$	Current set-point (pu)
$\bar{i}_{c_f,i}$	Current of the filter capacitor (pu)
$\delta_{m,i}$	Modulated voltage angle (rad)
θ_i	Angle of the Park's Transformation (rad)
ω_i	Angular speed of the $d-q$ reference frame (frequency) (pu)
$p_{m,i}$	Active-power of the GFM-VSC (pu)
$q_{m,i}$	Reactive-power of the GFM-VSC (pu)
$p_{g,i}$	Active-power at the bus g (pu)
$q_{g,i}$	Reactive-power at the bus g (pu)
$r_{c,i}$	Transformer resistance (L-filter) (pu)
$L_{c,i}$	Transformer inductance (L-filter) (pu)
x_c	Conextion reactance (pu)

Symbol	Description
x_v	Virtual reactance (pu)
x_{cv}	Virtual equivalent reactance (pu)
$r_{g,i}$	Grid resistance (pu)
$L_{g,i}$	Grid inductance (pu)

GFM-VSC connected via LC-filter

Symbol	Description
$\bar{e}_{m,i}$	Modulated voltage magnitude (pu)
$\bar{e}_{m,i}^{ref'0}$	Modulated voltage set-points (pu)
$\bar{m}_i$	Modulation index
m_i^{max}	Maximun modulation index
$v_{dc,i}$	DC voltage of the bus DC-link (pu)
$V_{dc,B}$	DC voltage base value (pole to pole) (V)
$V_{ac,B}$	AC voltage base value (phase to phase) (V)
$\bar{v}_{g,i}$	Voltage magnitude at the bus g (pu)
$\bar{v}_{f,i}$	Voltage magnitude at the bus f (pu)
$\bar{v}_{f,i}^{ref}$	Voltage magnitude set-point f (pu)
$\bar{i}_{g,i}$	Grid current (pu)
$\bar{i}_{f,i}^{ref'}$	Unsaturated current set-point (pu)
$\bar{i}_{s,i}^{ref}$	Current set-point (pu)
$\bar{i}_{s,i}^{ref}$	Output current (pu)
$\bar{i}_{c_f,i}$	Current of the filter capacitor (pu)
δ_i	Angle of the $d-q$ reference frame (rad)
$\delta_{f,i}$	Voltage angle of the GFM-VSC at the PCC (LC-filter) (rad)
θ_i	Angle of the Park's Transformation (rad)
ω_i	Angular speed of the $d-q$ reference frame in pu (frequency)
$p_{m,i}$	Active-power of the GFM-VSC (pu)
$q_{m,i}$	Reactive-power of the GFM-VSC (pu)
$p_{g,i}$	Active-power at the bus g (pu)
$q_{g,i}$	Reactive-power at the bus g (pu)
$p_{f,i}$	Active-power at the bus f (pu)
$q_{f,i}$	Reactive-power at the bus f (pu)
$r_{c,i}$	Transformer resistance (L-filter) (pu)

Symbol	Description
$L_{c,i}$	Transformer inductance (L-filter) (pu)
x_c	Conextion reactance (pu)
$r_{f,i}$	LC-Filter resistance (pu)
$L_{f,i}$	LC-Filter inductance (pu)
$C_{f,i}$	LC-Filter capacitor (pu)

GFM-VSC self-synchronisation control

Symbol	Description
$R_{PFR,i}$	Primary Frequency Response Droop Constant (pu)
$H_{GFM,i}$	Emulated Inertia Constant (s)
$D_{GFM,i}$	Damping Factor Coefficient (pu)
$\Delta\omega_i$	Frequency increment of the GFM-VSC output frequency (pu)
$p^0_{g,i}$	Constant Active-Power Set-Point (pu)
$p_{g,i}$	Active-Power delivered by the GFM-VSC at the PCC (pu)
ω_0	Nominal Frequency in radians per second (rad/s)
ω_b	Base Frequency in radians per second (rad/s)
$\omega_{0,pu}$	Nominal Frequency in pu
$\hat{\omega}_{g,PLL,i}$	Estimated grid frequency by the PLL (pu)
ω_n	Natural frequency (rad/s)
$T_{WD,i}$	Wash-out filter time constant (s)
K_p	IP-controller proportional gain (pu)
$\overline{s}_{g,i}$	Complex power injected by the GFM-VSC (pu)
$\Delta\theta_i$	Phase angle deviation (rad)
θ_i	Phase angle of the VSC voltage (rad)
$\theta_{g,i}$	Voltage phase angle at the PCC (rad)
$\pm\Delta p^{max}_{g,i}$	Active-power saturation limit of the PFC loop (pu)
$\pm\Delta p^{ref,PFR}_{g,i}$	Active-power set-point of the PFC loop (pu)
$T_{PFR,i}$	Time constant of the PFC (s)
$K_{PFR,i}$	Proportional gain of the PFR (pu)
$p^{virt}_{g,i}$	Virtual active power (pu)

FVB and TSP Controllers

Symbol	Description
$v_{f,i}^{ref}$	Voltage set point (pu)
$\Delta v_{f,i}^{ref,TS}$	Supplementary voltage set point (pu)
$v_{f,i}^{0}$	Initial voltage set point (pu)
$\Delta v_{f,i}^{max}$	Saturation parameter supplementary voltage set point (pu)
H_{tot}	Total inertial of all converters of the system (s)
ω_{COI}	Frequency of the centre of inertia (pu)
$\omega_{i}^{ref,TS}$	Frequency set point (pu)
ω_{i}	VSC frequency (pu)
$\omega_{thres,i}$	Frequency threshold (pu)
$T_{f,i}$	Low-pass filter time constant (s)
$T_{W,i}$	Wash-out filter time constant (s)
$K_{FVB,i}$	FVB-WACS proportional gain (pu)
$v_{A,i}$	Hysteresis lower limit voltage (pu)
$v_{B,i}$	Hysteresis upper limit voltage (pu)
$\Delta p_{g,i}^{ref,TS}$	Supplementary power set point (pu)
$\Delta p_{g,i}^{max}$	Power saturation limit of the supplementary set point (pu)
$K_{TSP,i}$	TSP proportional gain (pu)

Chapter 1

Introduction

1.1 Thesis topic

1.1.1 Power systems with large amounts of non-synchronous generation

Electrical power systems have traditionally been dominated by conventional synchronous generation. However, this scenario is changing with the increasing integration of renewable energy sources. In recent years, several countries, including Denmark, Germany, Spain, the United States, and the United Kingdom, have incorporated large amounts of renewable energy sources using converter-based generation within their power systems. Wind and solar photovoltaic generation are connected to the grid through voltage source converters (VSCs) and are often called non-synchronous generation. Depending on the specific technology, they can be fully (e.g., type-4 full-converter wind turbines or PV generators) or partially (type-3 doubly-fed induction generators (DFIG) wind turbines) interfaced with the grid [**Singh'11**].

Stability is a great challenge in power systems with high penetration of non-synchronous generation. Models and methods for stability analysis assessment of conventional power systems dominated by synchronous generation are well-established. However, the massive integration of non-synchronous generation technologies, such as wind and solar, introduces new challenges. These challenges arise from the fast dynamics of the VSCs that connect non-synchronous sources to the grid.

Synchronous-generation-based power systems are dominated by the slow electromechanical dynamics of synchronous generators, where the time constants of interest are about $0.1 - 10$ s [**Milano'10**]. Models used in stability

assessment of synchronous generation-based stability power systems include dynamic representations of the synchronous machine dynamics and their controllers. They also include simplified representations of FACTS and HVDC devices. However, the dynamic of the machine stator transients and the grid are not represented. In contrast, electrical power systems with a high penetration of non-synchronous generators are dominated by the fast dynamics of the VSCs. The dynamics of VSCs are much faster than the electromechanical dynamics. For example, the outer controllers of a VSC typically have time constants in the range $10 - 100$ ms [**Beerten'14**].

Even with significant penetration of non-synchronous generation, stability may still be dominated by the slow dynamics of synchronous machines. Nevertheless, the main issue is the changing dynamic behaviour of power systems with high penetration of non-synchronous generation. As more renewable energy sources are integrated into the grid, the overall inertia of the system decreases, significantly affecting the system's stability. As the power system is rapidly incorporating renewable energy sources, it brings new challenges to the transmission system operators (TSOs) responsible for maintaining the stability of the power system. Therefore, in scenarios close to 100% non-synchronous generation, TSOs must adapt to this changing landscape in order to ensure grid stability.

A power system is stable if it is capable of maintaining in a steady-state equilibrium point under normal conditions and it reaches a new equilibrium point when disturbances occur [**Kundur'04**]. This can be achieved by maintaining the frequency within an admissible range (Frequency stability) and the synchronism of generators (Angle stability) in case of disturbances. In conventional power systems dominated by synchronous generators, the rotating inertia determines the angle and frequency stability phenomena. As the penetration of non-synchronous generation increases, the total inertia of the power system will decrease. In large-scale power systems with a high penetration or even 100% non-synchronous generation, the stability of the power system is a much more complex problem because the dynamics of the system will depend strongly on how the VSC generators are controlled.

A VSC can be controlled in different ways. Most extended approaches are [**Guerrero'11**; **Guerrero'13**a; **Guerrero'13**b]:

- **Grid-following voltage source converter (GFL-VSC)**, also named grid-feeding VSC: is modelled as a current-controlled VSC, as shown in Figure 1.1, which controls the current injection (linked to the active- and reactive-power injections) into the AC grid. Grid-following con-

verters would synchronise with the frequency measured at their AC buses using a phase-locked loop (PLL). The converter synchronises to the grid voltage at its AC bus using a PLL, so it is important to remark that the converter requires an AC grid to be connected. GFL-VSCs may also have supplementary controllers for active and reactive power injections to provide support frequency and voltage to the system [**Rocabert'12**].

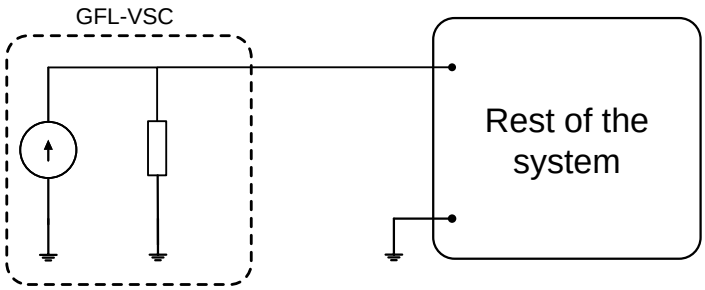

Figure 1.1: The GFL-VSC is modelled as a current controller.

- **Grid-forming voltage source converter (GFM-VSC)**: is modelled as a voltage-controlled VSC, as shown in Figure 1.2, that controls the voltage and the frequency of the AC grid. In this case, a converter can create a grid supplying passive loads, and the frequency of the system is the result of a control algorithm, and it is not necessarily linked to any electromechanical interaction. GFM-VSCs need synchronisation methods to synchronise with a grid without other types of generators. GFM-VSC converters can be synchronised by emulating the behaviour of synchronous machines (with the so-called virtual-synchronous-machine (VSM) and power/frequency-droop control techniques) [**DArco'14**; **Rocabert'12**; **Yu'16**].

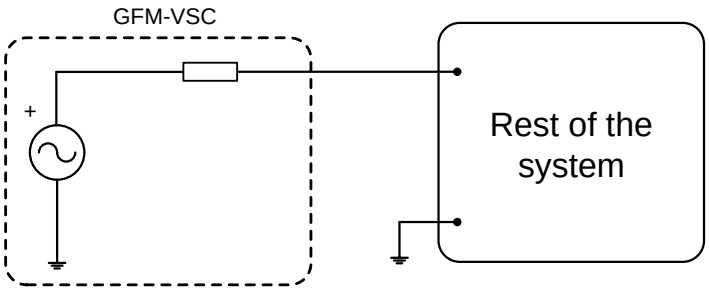

Figure 1.2: The GFM-VSC is modelled as a voltage controller.

Supplementary controllers can be implemented in either of the two ways of controlling a VSC, which will significantly impact power system stability, especially when considering scenarios with high penetration of non-synchronous generation. In scenarios where multiple GFM-VSCs operate in a power system, it is essential to have a self-synchronisation mechanism to ensure that all converters reach the same frequency in steady state. Fortunately, unlike grid-following VSCs, synchronisation can be achieved without the use of a phase-locked loop (PLL) by using additional control strategies. The majority of those supplementary control strategies mimic the behaviour of conventional synchronous generators. The most common option in alternating-current (AC) power systems is the so-called power-frequency (P-f) droop [**Rocabert'12**; **Olivares'14**]. Meanwhile, controllers for emulation of synchronous machines have become the most common option in modern large power systems, and they are so-called synchronverters [**Zhong'11**] or virtual synchronous machines (VSM) [**DArco'15**; **Roldán-Pérez'19**]. Furthermore, the work in [**DArco'14**] proved that P-f droop supplementary controllers and VSM supplementary controllers are equivalent. A different approach for self-synchronisation of GFM-VSCs is the concept of reactive-power synchronisation, proposed recently in [**RodriguezA'21**].

1.1.2 GFM-VSCs in power systems

The grid-forming VSC (GFM-VSC) is considered the key technology for the operation of future electrical power systems, ranging from small microgrids [**Rocabert'12**; **Olivares'14**] to large transmission systems [**Milano'18**; **Paolone'20**]. The main characteristic of a GFM-VSC is that it is capable of

creating a grid by controlling its output voltage magnitude and frequency. This is not possible with most extended grid-following VSCs, which need an external grid to be connected.

In power systems with 100% non-synchronous generation, synchronisation of VSC converters becomes particularly necessary. While large power systems with 100% non-synchronous generation are not yet a reality, concepts proposed for microgrids can be applicable. Microgrids with 100% non-synchronous generation require VSC converters to be synchronised using supplementary control strategies. An important concept is that any system with 100% non-synchronous generation must have at least one converter controlled as GFM-VSC, which means that it is mandatory to have at least one device capable of imposing the frequency of the system ("creating the grid"). In GFM-VSC converters with virtual synchronous machines (VSM) or power-frequency control droop, this grid-forming role can be distributed among multiple converters, due to self-synchronisation mechanisms.

Research studies such as those conducted in the European project MIGRATE [**Qoria'18**a] have analysed the stability and performance of power systems with 100% non-synchronous generation, emphasising the need for GFM-VSC converters and different control variants. For example, a study [**Ramasubramanian'18**] investigated a power system with 100% VSC-based generation and demonstrated stable system operation through the use of grid-forming converters with grid-following converters implementing frequency and angle power droop. Another work [**Watson'19**] examined the stability of a small power system with two VSC generators, concluding that passivity techniques could be employed to design supplementary controllers and ensure system stability.

The transition from conventional synchronous generation to systems with 100% non-synchronous generation poses challenges regarding the inertial response of power systems. Conventional power systems rely on rotating inertia provided by synchronous generators to maintain angle and frequency stability. However, with an increasing share of non-synchronous generation, the overall inertia of the power system decreases, impairing the inertial response of the power system. Low-inertia systems combine conventional and non-synchronous generation, presenting operational and stability challenges [**Milano'18**]. Insights into stability issues faced by modern low-inertia systems, particularly frequency stability, can be obtained from existing low-inertia systems such as geographic islands [**Sigrist'12**]. Small-signal stability analyses have been carried out to study stability in low-inertia power systems with VSC converters controlled as grid-forming or grid-following [**Collados-**

Rodriguez'20; **Mauricio'20**; **Markovic'21**]. The research [**Markovic'21**] presented a detailed framework for stability analysis, while other studies [**Collados-Rodriguez'20**; **Mauricio'20**] proposed solutions to enhance inter-area oscillation damping in power systems with high VSC-based or non-synchronous generation. The works [**Chamorro'16**b; **Chamorro'16**a] investigate the impact of non-synchronous generation on power systems coherency, analysing the effects of renewable energy integration on power systems dynamics and the methods used for coherent group identification. The study also evaluates the impact of non-synchronous generation on power systems and provides valuable insights for dynamic studies and transmission capability improvement.

1.1.3 Transient stability of power systems with 100% non-synchronous generation

Transient stability is a complex phenomenon in multi-machine and multi-converter systems, and it is still considered a limiting factor for stressed power systems. By definition, transient stability (or angle stability with large disturbances) is defined as the ability of the generators in the system to remain in synchronism under normal operating conditions and to recover synchronism when large disturbances occur [**Kundur'04**; **Hatziargyriou'20**a]. Instances of large disturbances are short circuits, large generators, or load tripping. This definition assumes that the system contains synchronous generators since the phenomenon is related to the rotor angle of these types of machines. However, in the technical literature, the term "transient stability" is also used to refer to the phenomenon of loss of synchronism in systems with high or 100% penetration of non-synchronous generation [**Du'19**; **Zhao'20**b; **He'22**].

The phenomenon of transient stability appears in power systems with a high penetration of renewable energy that still contains synchronous generators [**Wang'20**; **Amano'18**]. Power electronic converters introduce fast and non-linear dynamics into the system, which can affect the overall stability of such a system. This type of stability refers to instability phenomena that may arise due to the interaction between power electronic converters and the electrical system in cases of large disturbances. Recent publications have shown that transient stability is also a concern in power systems with 100% GFM-VSC-based generation [**Du'19**; **Zhao'20**b; **He'22**]. Therefore, power electronic converters can directly impact the transient stability of power systems. In other words, if GFM-VSCs emulate synchronous machines, they

can also lose synchronism in the case of severe-enough faults. Angle stability against large disturbances, in particular the phenomenon of loss of synchronism, is thus a critical consideration in systems with high penetration or 100% non-synchronous generation.

The work in [**Andrade'11**] observed that the loss-of-synchronism phenomenon can occur in AC microgrids with GFM-VSC generators equipped with P-f droop control and transient stability was assessed by means of Lyapunov's theory. Further studies are presented in [**Xin'16**; **Eskandari'20**], where the impact of current saturation [**Xin'16**] and fault-ride-through (FRT) capability [**Eskandari'20**] of GFM-VSCs on transient stability is analysed. References [**Shuai'18**; **Cheng'20**] analysed transient stability in power systems with GFM-VSC controlled as VSMs. A similar approach is followed in [**Pan'20**], where a thorough analysis of transient stability of GFM-VSCs is provided.

According to [**Hatziargyriou'20**a], a Task Force was established in 2016 [**Hatziargyriou'20**b] to re-examine and extend the classic definitions and classifications of power system stability terms previously established in the reference [**Kundur'04**] to incorporate the effects of power electronic devices. The new classification [**Hatziargyriou'20**a] incorporates the category of *Converter-driven Stability* (see Figure 1.3) as a consequence of the increasing penetration of converter-interfaced generation technologies (CIGs) in modern power systems. This category of stability refers to the stability phenomena that can arise due to the interaction between power electronic devices and the power system, and it is characterised by the presence of fast and poorly damped oscillations in the system. The classification of power system stability in [**Hatziargyriou'20**a], is based on the intrinsic system dynamics, characterised by different time scales associated with physical phenomena. The proposal distinguishes between two broad categories of stability within power electronic converters: fast and slow interactions.

- **Fast-Interaction Converter-driven Stability** is a type of instability of power systems that arises due to the fast dynamic interactions between the control systems of power electronic-based devices (such as VSCs, HVDC, and FACTS) and fast-response components of the power system (such as the transmission network, the stator dynamics of synchronous generators, or other power electronic-based devices). This type of stability can lead to system-wide stability problems driven by fast dynamic interactions of the control systems of power electronic-based systems with fast-response components of the power system.

These instabilities can be difficult to control and can lead to system collapse if not properly addressed. This type of stability category is associated with timescales that are typically in the range of $10 - 100$ ms (and possibly in the range of $1 - 100$ ms).

- **Slow-Interaction Converter-driven Stability** is a type of instability of power systems that arises due to the slow dynamic interactions between the control systems of power electronic-based devices and the slow-response components of the power system, such as the electromechanical dynamics of synchronous generators and some generator controllers. This type of stability can lead to system-wide instabilities, which can be driven by the interaction between power electronic devices and the slow-response components of the power system. These instabilities can be difficult to control and can lead to system collapse if not properly addressed. This category of stability is associated with timescales typically greater than 10 ms, for example, in the range of 10 ms to hundreds of seconds (e.g. $0.1 - 10$ s).

Unfortunately, the new proposal in [**Hatziargyriou'20**a] still needs to provide specific details on the classification of the phenomenon of loss of synchronise involving electronic power converters. The definition of rotor angle stability presented in [**Kundur'04**] remains unchanged even after the integration of CIGs. However, as conventional synchronous generators are replaced by CIGs, the total inertia of the system decreases, which has a significant impact on the rotor angle stability as well as the electromechanical modes of the system [**Tielens'16**]. This type of instability arises in power systems due to insufficient or negative synchronising torque, resulting in non-oscillatory transient instability.

There is no particular category that encompasses these types of instabilities within a single class in power systems with 100% non-synchronous generation. According to the classification [**Hatziargyriou'20**b; **Hatziargyriou'20**a], the phenomenon of loss of synchronism in power systems with a high penetration of VSC power converter can be categorised into two main types, as shown in Fig 1.3:

- ***Converter-driven Stability - Slow-Interaction***.
- ***Rotor angle stability - Transient***.

Figure 1.4 represents the power system timescales of the current classification [**Hatziargyriou'20**a]. The category of *Rotor Angle Stability* is

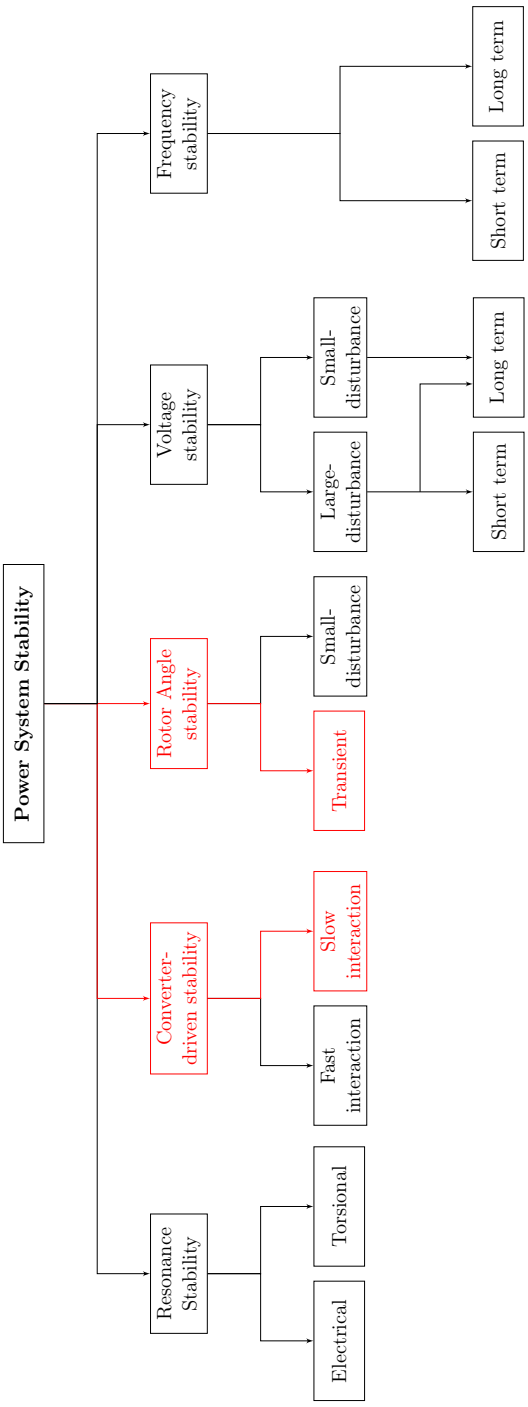

Figure 1.3: Classification of power system stability [**Hatziargyriou'20**b; **Hatziargyriou'20**a].

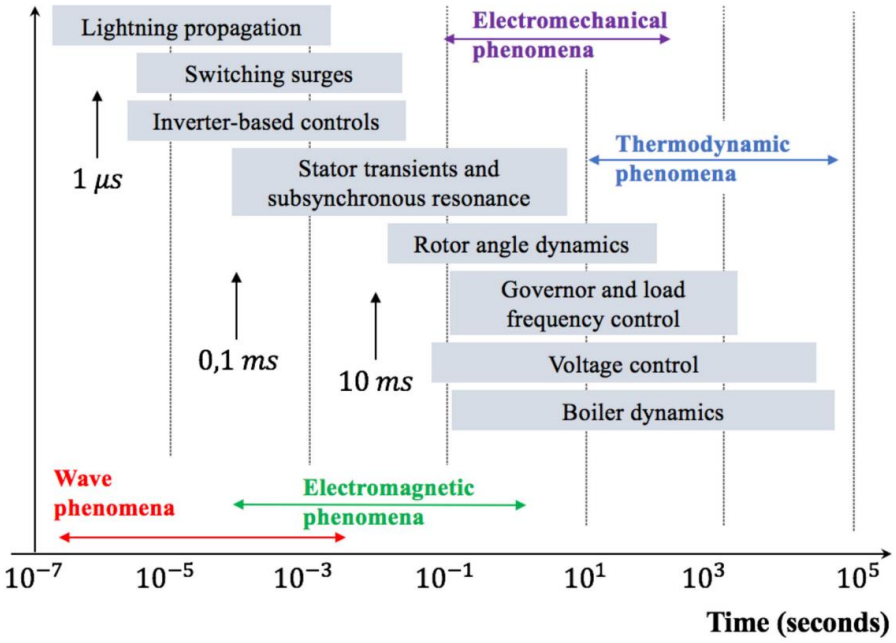

Figure 1.4: Power system times scales. Taken from [**Hatziargyriou'20**b; **Hatziargyriou'20**a].

typically associated with timescales ranging from a few seconds to tens of seconds, while converters' dynamic responses to loss synchronism can vary from a few milliseconds to several seconds. Therefore, these dynamic responses of the converters can be considered as *Slow Interaction* types belonging to the *converter-driven stability* category, as shown in Figure 1.3 [**Hatziargyriou'20**a].

1.1.4 Methods to improve transient stability for GFM-VSCs

Previous studies [**Andrade'11**; **Xin'16**; **Shuai'18**; **Cheng'20**; **Pan'20**; **Eskandari'20**] have examined the impact of various control approaches on transient stability in GFM-VSC-based systems. These publications have explored the effects of droop control, current saturation, fault-ride-through capability, and voltage source modulation. The research [**Kanakesh'21**] studied the impact of current limiters on transient stability in grid-forming converters, specif-

ically when these converters operate at or near their current limit. Furthermore, loss of synchronism in large power systems has been extensively studied, and numerous control strategies have been proposed to improve transient stability in power systems with 100% GFM-VSC-based generators [**Zhao'20**a; **Zhao'22**]. Maintaining transient stability is crucial for ensuring the reliability of the power system, as it is susceptible to disturbances such as sudden load changes, faults, and switching operations.

In recent years, significant research has been dedicated to improving the transient stability of power systems. In particular, researchers have conducted extensive studies on improving the transient stability of power systems with GFM-VSCs. In order to tackle this challenge, control strategies involving suitable current-limitation algorithms and active-power injection control have been proposed. Various approaches have been proposed, such as adaptive emulated inertia in GFM-VSCs [**Qoria'20**c], active power control strategies [**Choopani'19**; **Choopani'20**; **Xiong'21**a] and the implementation of current limiters [**Qoria'20**b; **Qoria'20**a; **Rokrok'21**].

The methods for transient stability improvement can be divided into four main categories: Self-synchronisation strategies, which use supplementary controllers for synchronisation and they can also help to improve the transient stability [**Zhao'20**a; **Zhao'22**]; Current Limiters (CL) [**Qoria'20**b; **Qoria'20**a; **Rokrok'21**], which limit the fault current and reduce the rotor angle deviation; active-power control strategies [**Choopani'19**; **Choopani'20**; **Xiong'21**a] and voltage/reactive-power control strategies [**Chen'22**], which apply external control signals to modify set-points of operating conditions. Figure 1.5 summarises these four methods of improving the transient stability of power systems with GFM-VSCs. This figure provides a visual representation of the methods used and gives an organised overview of the different strategies and control techniques involved in each category.

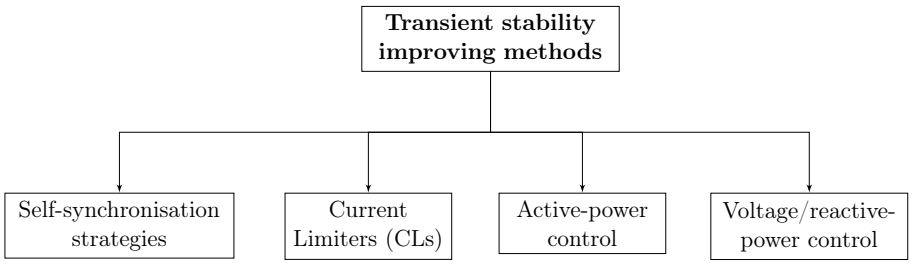

Figure 1.5: Methods for improving the transient stability in GFM-VSCs

The implementation of current limitation algorithms in GFM-VSCs serves one main objective: it aims to restrict the current within safe limits to protect the converters from overcurrent conditions, thereby preventing potential damage to the semiconductor switches. In addition, current-limitation algorisms in GFM-VSCs can have an impact on transient stability, and novel algorisms would be used to improve it [**Qoria'20**a; **Rokrok'21**]. By effectively managing and controlling the current flow, they help maintain system stability during transient events and improve overall power system performance. The use of current limiters has demonstrated their potential in reducing fault current contribution and improving transient stability [**Qoria'20**b].

Active power control strategies in GFM-VSC are employed to mitigate these instabilities and improve the transient stability of the power system. Most of the active power-based control strategies proposed in the literature to improve the transient stability of GFM-VSCs require fast adjustments of the primary energy sources. However, this feasibility depends on the generator technology, which may limit their implementation. To overcome this limitation, the integration of Energy Storage Systems (ESS) can provide a solution.

Another alternative approach is to use control strategies based on voltage/reactive-power control in GFM-VSCs. Although, these control strategies have been successfully applied in synchronous generators with excitation boosters [**Lee'86**; **Kundur'94**; **Díez-Maroto'19**b; **Diez-Maroto'17**; **Díez-Maroto'19**a; **Díez-Maroto'20**], shunt FACTS devices [**Haque'04**], and VSC-HVDC systems [**Fuchs'14**; **Sigrist'15**; **Renedo'17**]; their use in GFM-VSCs for improving transient stability in power systems with 100% non-synchronous generation remains understudied [**Chen'22**]. Thus, there is a remarkable open area of research and development in the design of control mechanisms specifically focused on voltage/reactive-power control strategies in GFM-VSCs. Moreover, the effect of converter output voltages and reactive power injections on transient stability has been studied in [**Pan'19**]. The study examines the behaviour of a GFM-VSC connected to an infinite grid and shows that increasing the steady-state reactive power set-point improves the transient stability margin. The use of voltage/reactive-power control strategies sets the voltage set-point of the GFM-VSCs influencing the reactive power injections. The advantage of these types of approaches is that it does not require significant changes to the primary energy source set-points.

To advance the field and improve transient stability in power systems with GFM-VSCs, it is crucial to conduct further research and develop effective reactive power control strategies. Bridging this open area of research holds

significant potential for improving performance and reliability. Addressing this research gap can benefit power systems using GFM-VSCs technology by improving transient stability, ultimately leading to improved overall system performance and increased reliability.

This motivates the investigation of supplementary controllers in GFM-VSCs to improve the transient stability analysis of large power systems with 100% non-synchronous generation. A summary of the main topics of this thesis is as follows:

- Understanding the self-synchronisation mechanisms of GFM-VSCs connected to the grid and their impact on transient stability.
- Analysis the transient stability of power systems with 100% GFM-VSC-based generation.
- Proposal and development of control strategies for GFM-VSCs to improve transient stability in power systems with 100% non-synchronous generation

1.2 Thesis objectives

In light of these considerations, the objective of this thesis is to understand and analyse the transient stability of power systems with 100% non-synchronous generators with GFM-VSCs, which is becoming increasingly relevant due to the integration of renewable energy sources. The thesis will focus on analysing transient stability of power systems with a significant presence of non-synchronous generation and developing control strategies based on active- and voltage/reactive-power control in GFM-VSCs to improve transient stability. By addressing these objectives, this research will contribute to a better understanding of power system stability of power system with 100% VSC-based generators.

The main objectives of this thesis are:

- Objective 1: Compare different control self-synchronisation strategies employed in GFM-VSCs under different scenarios and analyse their impact on transient stability.
- Objective 2: Investigate voltage/reactive-power (Q-V)-based control strategies for GFM-VSCs to improve transient stability in power systems with 100 % non-synchronous generators.

- Objective 3: Examine the impact of Q-V control strategies, using different current limiters applied to GFM-VSCs, on transient stability in power systems with 100% non-synchronous generators..

- Objective 4: Investigate active-power-based control strategies for GFM-VSCs to improve transient stability in power systems with 100% non-synchronous generators.

By addressing these objectives, this study aims to contribute to understanding the analysis of the transient stability improvement in electrical power systems with 100% non-synchronous generation, providing valuable insights for control of GFM-VSCs in future power systems.

1.3 Thesis roadmap

The thesis has been organised into seven chapters. In order to provide a clear outline of the document and to make it easier for the reader to navigate through the contents, the containing of the following chapters is:

- **Chapter 2** presents the modelling and control of GFM-VSCs along with their implementation in Matlab/Simulink/SimPowerSystems.

- **Chapter 3** evaluates the performance of different self-synchronisation methods for GFM-VSCs in various operating scenarios, and analyses their impact on transient stablity. It focuses on comparing the virtual synchronous machine (VSM) approach with and without a phase-locked loop (PLL) and the IP controller approach. The chapter includes a theoretical analysis of the equivalence between VSM and IP controllers and examines their performance under different power system scenarios.

- **Chapter 4** proposes and analyses Fast Voltage Boosters (FVBs) strategies based on voltage/reactive-power control in GFM-VSC for transient stability improvement in power systems with 100% non-synchronous generators. The proposed strategies do not modify the set points linked to the frequency/active-power injection. One control strategy (FVB-L) uses local measurements, while the other (FVB-WACS) uses global measurements of the frequency of the center of inertia (COI). It presents theoretical analysis and simulation results to validate the effectiveness of the proposed strategies.

- **Chapter 5** studies the impact of hybrid current limiters (HCLs) and fast voltage boosters (FVBs) on transient stability in power systems. It reviews previous work on current limiter strategies and presents the combination of the current saturation algorithm (CSA) and current limiter based on virtual impedance (VI-CL) as HCLs. The chapter evaluates the effectiveness of HCLs and FVBs through short-circuit simulations and critical clearing time analysis, demonstrating their ability to improve transient stability.

- **Chapter 6** proposes a local Active-power control (TSP-L) strategy in GFM-VSCs for transient stability improvement in power systems with 100% non-synchronous generators. The proposed strategy is compared with two existing active-power control strategies (TSP-WACS and TSP-TDM) in the literature. The chapter investigates the effectiveness of these strategies through simulation results, demonstrating their ability to enhance transient stability and critical clearing time during short-circuit events.

- **Chapter 7** provides the conclusions of the thesis, summarising its contributions and suggesting areas for further research.

- **Appendix A** contains the detailed information necessary to replicate the results presented in the previous chapters.

Chapter 2

Modelling and control of GFM-VSCs

2.1 Introduction

This chapter presents the modelling and control aspects of a GFM-VSC. The GFM-VSC controls the voltage magnitude and frequency at the point of common coupling (PCC) and ensures synchronisation with the grid. The control strategies discussed in this chapter enable VSCs to operate in grid-forming mode and contribute to system stability by capturing the dynamic behaviour of the converter and its interaction with the grid. The model includes the equivalent circuit diagram of the GFM-VSC, consisting of an ideal voltage source connected to the system through an LC filter and a connection transformer. The control system incorporates voltage and current controllers, virtual transient resistance, voltage modulation, and a grid-forming mechanism for self-synchronisation.

The rest of the chapter is organised as follows: Section 2.2 presents the model of a grid-forming voltage source converter, including its equivalent circuit model and the general control scheme of a GFM-VSC. Section 2.3 discusses the self-synchronisation control strategy for GFM-VSCs and provides an overview of different methods, particularly emphasising the virtual synchronous machine (VSM) control. Section 2.4 introduces the current limiter, specifically the Current Saturation Algorithm (CSA), used to limit the converter current during grid faults. Section 2.5 explores the concept of virtual impedance and its role in grid-forming VSCs. Finally, the summary of the chapter is provided in Section 2.7.

2.2 Modelling and control

This section presents the model of a GFM-VSC, based on the references [**Qoria'18**b; **Paolone'20**; **Rokrok'20**; **Qoria'20**c; **Pereira'20**]. In this thesis, two models of converters have been used:

- GFM-VSC connected to an infinite grid via an L-filter.
- GFM-VSC connected to the system via an LC-filter.

The LC filter consists of an inductor and a capacitor in series, while the L filter consists of a single inductor. For a detailed understanding of the control system, please refer to [**Qoria'18**b; **Paolone'20**; **Rokrok'20**; **Qoria'20**c], while this chapter provides a summary of its key aspects.

2.2.1 GFM-VSC connected to an infinite grid via an L-filter

Figure 2.1 shows the model diagram of a GFM-VSC connected to an infinite grid through an L-filter. The converter is represented as an ideal voltage source ($\bar{e}_{m,i}$) connected to the grid at bus g via a connection transformer and an L-filter. The L-filter and connection transformer are represented by the series resistance $r_{c,i}$ and inductance $L_{c,i}$ ($r_{c,i} + x_{c,i}$), which is the coupling and connection impedance with the grid and it helps to suppress high-frequency harmonics. The voltage at the PCC (bus g) is denoted as $v_{g,i}$, whereas the converter output current is denoted as $i_{g,i}$, which serves as the feedback signal for the current control loop.

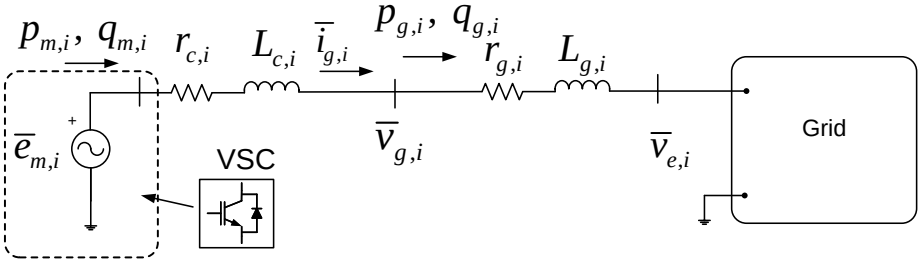

Figure 2.1: Equivalent model of a Grid-Forming Voltage Source Converter GFM-VSC.

According to the equivalent model of the GFM-VSC from Figure 2.1, the instantaneous voltages and currents may be expressed by the following differential equation written in the internal $d-q$ axes:

$$\bar{e}_{m,i} - r_{c,i}\bar{i}_{g,i} - L_{c,i}\frac{d\bar{i}_{g,i}}{dt} - j\omega_i L_{c,i}\bar{i}_{s,i} - \bar{v}_{g,i} = 0 \tag{2.1}$$

where ω_i is the angular speed of the $d-q$ reference frame. The voltage source $\bar{e}_{m,i}$ represents the internal dynamics and control mechanisms of the GFM-VSC.

The control of the GFM-VSC aligns the voltage magnitude $\bar{e}_{m,i}$ with the $d-$axis of the $d-q$ reference frame of the GFM-VSC, as shown in Figure 2.2. The control of the GFM-VSC in Figure 2.1 imposes its output voltage magnitude $\bar{e}_{m,i}$ and its frequency ω_i to synchronise the converter to the PCC (bus g). This implies that the GFM-VSC controls the voltage angle δ_i.

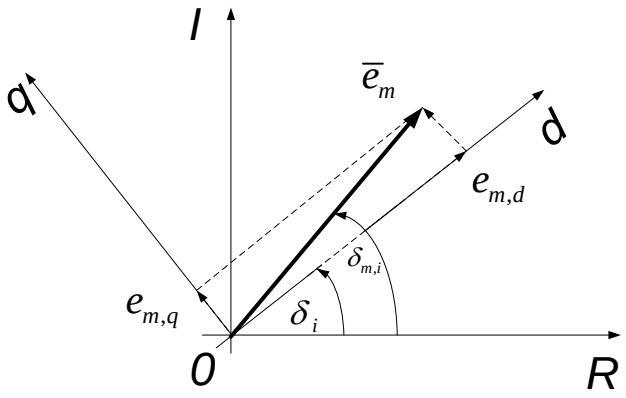

Figure 2.2: Grid-forming VSC: $d-q$ axes.

The control of the GFM-VSC is oriented to a $d-q$ mobile reference frame where the differential equations are written. The control structure of the GFM-VSC using an L-filter is depicted in Figure 2.3 and it is comprised as follows: (a) a quasi-static model for calculation of current set-points, (b) a current controller with current limitation, (c) voltage modulation with modulation index limitations, and (d) a grid-forming mechanism for self-synchronisation (VSM, IP controller or any other variant).

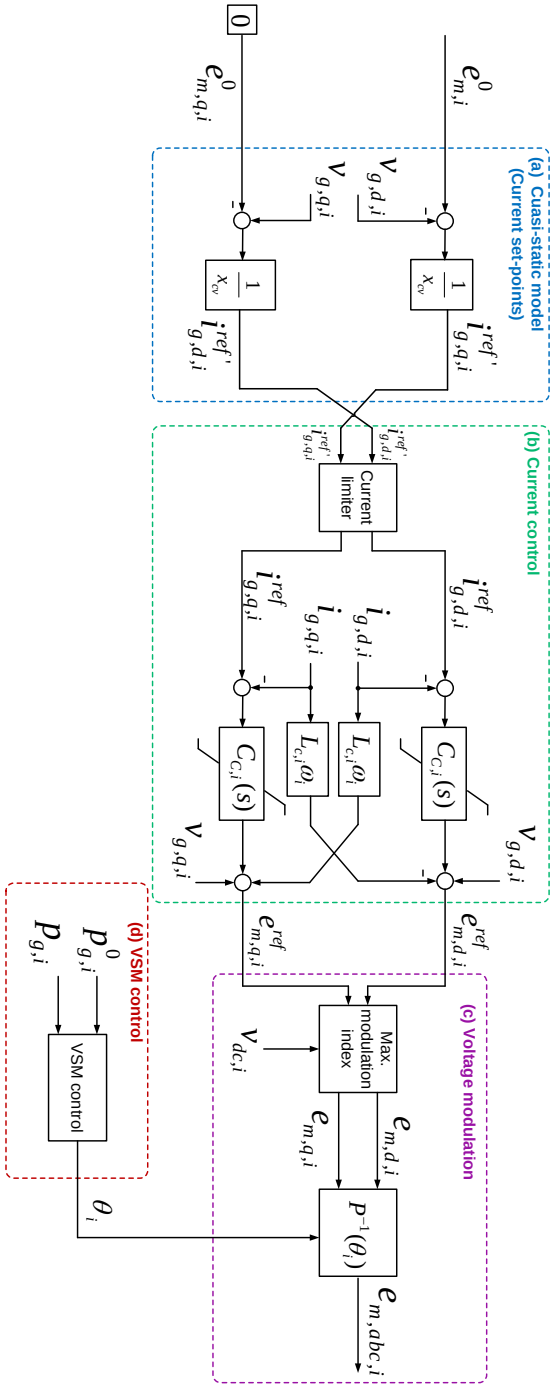

Figure 2.3: General scheme of the control system of a grid-forming VSC.

Initially, the GFM-VSC introduces an angle δ_i (in radians) for the mobile $d-q$ reference frame, which rotates at a speed of ω_i (in pu), as shown in Figure 2.2. This angle δ_i is referenced to an arbitrary mobile $R-I$ reference frame rotating at the synchronous frequency ($\omega_{0,pu} = 1$ pu). The position of the d-axis with respect to a static reference frame ($\alpha-\beta$ axes whose angular speed is equal to zero), denoted as θ_i, is used in Park's Transform to relate variables to the $d-q$ reference frame. The methodology for obtaining this angle δ_i through the self-synchronisation method ((e) in Figure 2.3) will be discussed in Section 2.3.

Calculation current set-points, shown as (a) in Figure 2.3 are obtained from the quasi-static model using a virtual admittance expression [**Laba'23**; **Kanakesh'23**]:

$$\begin{aligned} i_{g,q,i}^{ref'} &= \frac{v_{g,d,i} - e_{m,d,i}^{0}}{x_{cv,i}} \\ i_{g,d,i}^{ref'} &= \frac{e_{m,q,i}^{0} - v_{g,q,i}}{x_{cv,i}} \end{aligned} \tag{2.2}$$

where $x_{cv} = x_c + x_v$ and x_v is the expression of a virtual reactance added to connection impedance x_c.

The terms $e_{m,d,i}^{0}$ and $e_{m,q,i}^{0}$ from Eq. (2.2) are the voltage set-points used for the current set-point calculations in Figure 2.3. Here, $e_{m,i}^{ref'0}$ represents the initial operation set-point of the GFM-VSC converter voltage magnitude, and $e_{m,q,i}^{ref}$ is controlled to zero. The current set-points are the input of the current controllers. The current controllers consist of PI controllers and a current limiter, shown as (c) in Figure 2.3. The general schemes of the current set-point calculation and the current controllers are shown in Figures 2.4 and 2.5 respectively. The current limiter is implemented using the conventional current saturation algorithm (CSA) commonly employed in vector control [**Qoria'20**b], limiting the modulus of the current vector. The modulated voltages $\bar{e}_{m,d,i}$ and $\bar{e}_{m,q,i}$, related to the DC voltage, are the outputs of the current controllers and can be expressed as:

$$\bar{e}_{m,i} = \bar{m}_i v_{dc,i}, \quad \text{with} \quad e_{m,i} \leq m_i^{max} v_{dc,i} \quad \text{(pu)}, \tag{2.3}$$

where $\bar{m}_i$ denotes the modulation index. The maximum modulation index (magnitude), in pu, is calculated as:

$$m_i^{max} = \sqrt{\frac{3}{2}} \cdot \frac{V_{dc,B}}{2V_{ac,B}} \quad \text{(pu)}, \tag{2.4}$$

where $V_{dc,B}$ represents the DC voltage base value (pole to pole), and $V_{ac,B}$ is the AC voltage base value (phase to phase).

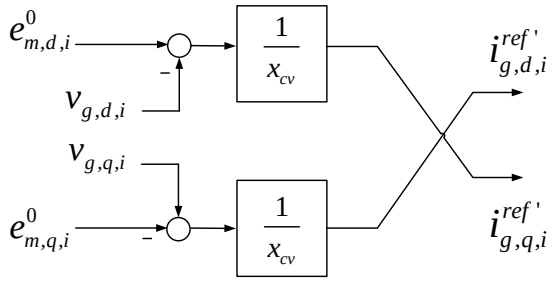

Figure 2.4: Voltage control loop of the GFM-VSC in $d-q$ axes.

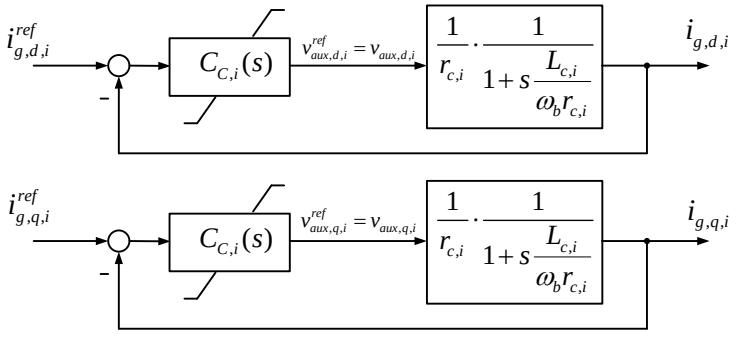

Figure 2.5: Curent control loop of the GFM-VSC in $d-q$ axes.

2.2.2 GFM-VSC connected to the system via an LC-filter

The equivalent model diagram of a GFM-VSC-i connected to the system via an LC-filter is illustrated in Figure 2.6. The converter is represented as an ideal voltage source ($\bar{e}_{m,i}$) connected to the rest of the system at bus g through an LC filter and a connection transformer. The voltage at bus g is

denoted as $v_{g,i}$, and the voltage at the PCC (bus f) is represented as $v_{f,i}$. The converter current is denoted as $i_{s,i}$, which serves as the feedback signal for the current control loop, while the output current is denoted as $i_{g,i}$. The LC filter comprises a phase reactor $\bar{z}_{f,i}$ characterised by its series resistance $r_{f,i}$ and inductance $L_{f,i}$, and a branch capacitor $C_{f,i}$, which serve to suppress high-frequency harmonics.

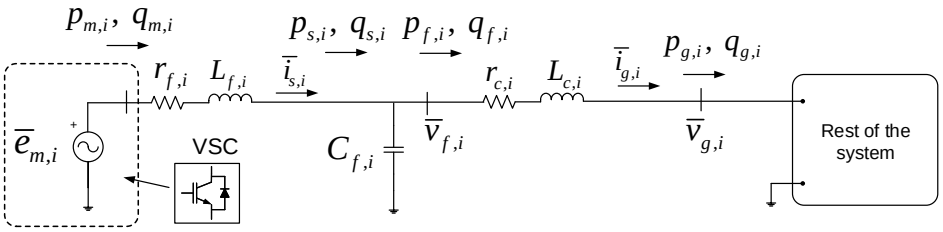

Figure 2.6: Equivalent model of a Grid-Forming Voltage Source Converter GFM-VSC.

Under this equivalent model of the GFM-VSC, the instantaneous voltages and currents can be described by the following differential equations written in the internal $d-q$ axes:

$$\bar{e}_{m,i} - r_{f,i}\bar{i}_{s,i} - L_{f,i}\frac{d\bar{i}_{s,i}}{dt} - j\omega_i L_{f,i}\bar{i}_{s,i} - \bar{v}_{f,i} = 0 \tag{2.5}$$

$$\bar{v}_{f,i} - r_{c,i}\bar{i}_{g,i} - L_{c,i}\frac{d\bar{i}_{g,i}}{dt} - j\omega_i L_{c,i}\bar{i}_{g,i} - \bar{v}_{g,i} = 0 \tag{2.6}$$

$$C_{f,i}\frac{d\bar{v}_{f,i}}{dt} - \bar{i}_{c_f,i} + j\omega_i C_{f,i}\bar{v}_{f,i} = 0 \tag{2.7}$$

where $i_{c_f,i} = i_{s,i} - i_{g,i}$, is the current of the filter capacitor and ω_i is the angular speed of the $d-q$ reference frame in which the differential equations are written. The voltage source $\bar{e}_{m,i}$ represents the internal dynamics and control mechanisms of the GFM-VSC, while the LC filter and transformer represent the coupling and connection impedance with the rest of the system.

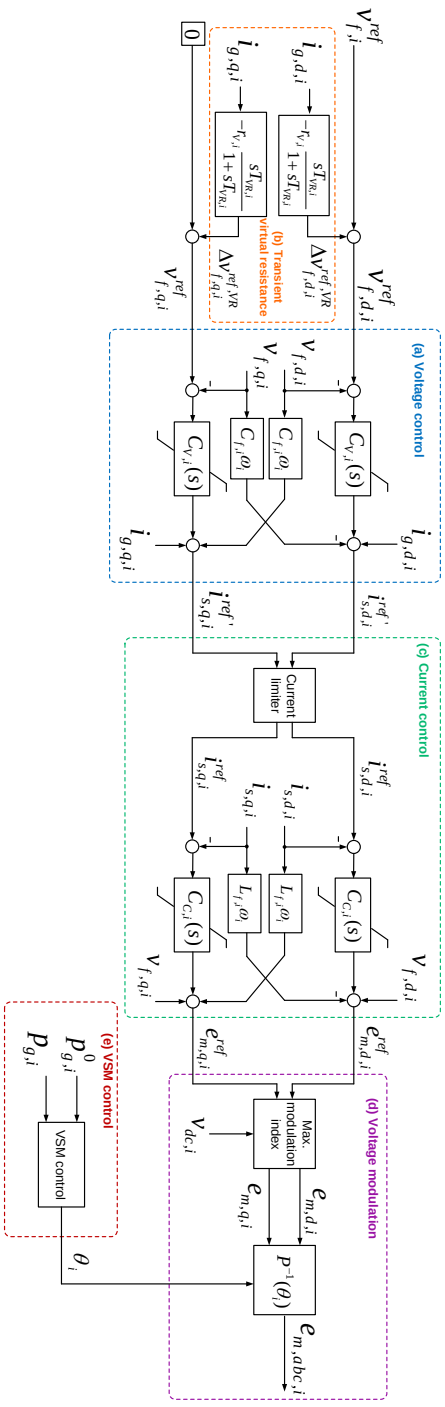

Figure 2.7: General scheme of the control system of a grid-forming VSC.

The GFM-VSC in Figure 2.6 controls the voltage magnitude $v_{f,i}$ and frequency $\omega_{f,i}$ (and consequently the voltage angle $\delta_{f,i}$) at the bus f_i.

Figure 2.7 illustrates the general control structure of the GFM-VSC-i of Figure 2.6 based on vector control, as described in [**Rokrok'20**; **Qoria'20**c]. The control system consists of the following: (a) a voltage controller, (b) a virtual transient resistance, (c) a current controller with current limitation, (d) voltage modulation with modulation index limitations, and (e) a grid-forming mechanism for self-synchronisation, such as Virtual Synchronous Machine (VSM) or any other variant.

The GFM-VSC introduces an angle δ_i (in radians) for the mobile $d-q$ reference frame. This frame rotates at a speed of ω_i (in pu), as seen in Figure 2.8. The angle δ_i is referenced to an arbitrary mobile $R-I$ reference frame that rotates at the synchronous frequency ($\omega_{0,pu} = 1$ pu). The d-axis position relative to a static reference frame ($\alpha-\beta$ axes whose angular speed is zero), which is denoted as θ_i, is used in Park's Transform to correlate variables with the $d-q$ reference frame. The process of obtaining this angle δ_i through the self-synchronisation method ((e) in Figure 2.7) is explained in Section 2.3.

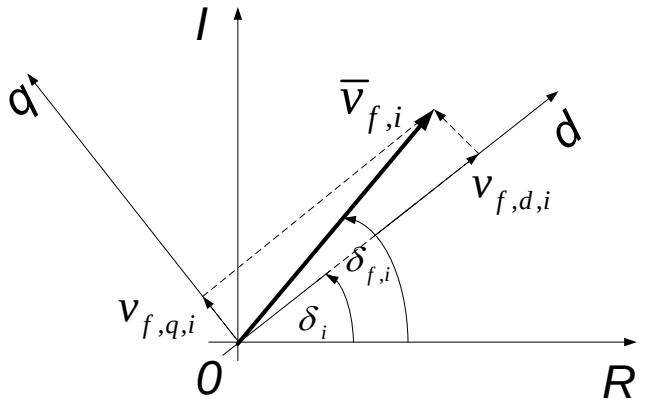

Figure 2.8: Grid-forming VSC: $d-q$ axes.

The voltage control loop in Figure 2.7 controls $v_{f,d,i}$ and $v_{f,q,i}$ using proportional-integral (PI) controllers, with the set-point values defined as

follows:

$$\begin{aligned} v_{f,d,i}^{ref} &= v_{f,i}^{ref} + \Delta v_{f,d,i}^{ref,VR} \\ v_{f,q,i}^{ref} &= 0 + \Delta v_{f,q,i}^{ref,VR} \end{aligned} \tag{2.8}$$

where $v_{f,i}^{ref}$ represents the set-point for the magnitude of the voltage, and $v_{f,q,i}^{ref}$ is controlled to zero.

The voltage controller aligns the voltage $\bar{v}_{f,i}$ with the $d-q$ axes of the GFM-VSC, as shown in Figure 2.8. The outputs of the voltage controller are the set-points for the $d-q$ current components of the current controllers, which include PI controllers and a current limiter ((c) in Figure 2.7). The block diagram of the PI voltage controller is shown in Figure 2.9, while the PI current controller is represented in Figure 2.10. The current limiter is implemented using the conventional current saturation algorithm (CSA) commonly employed in vector control [**Qoria'20**b], limiting the modulus of the current vector. The modulated voltages $\bar{e}_{m,d,i}$ and $\bar{e}_{m,q,i}$, related to the DC voltage, are the outputs of the current controllers and can be expressed as:

$$\bar{e}_{m,i} = \bar{m}_i v_{dc,i}, \quad \text{with} \quad e_{m,i} \leq m_i^{max} v_{dc,i} \quad \text{(pu)}, \tag{2.9}$$

where $\bar{m}_i$ denotes the modulation index. The maximum modulation index (magnitude), in pu, is calculated as:

$$m_i^{max} = \sqrt{\frac{3}{2}} \cdot \frac{V_{dc,B}}{2V_{ac,B}} \quad \text{(pu)}, \tag{2.10}$$

where $V_{dc,B}$ represents the DC voltage base value (pole to pole), and $V_{ac,B}$ is the AC voltage base value (phase to phase).

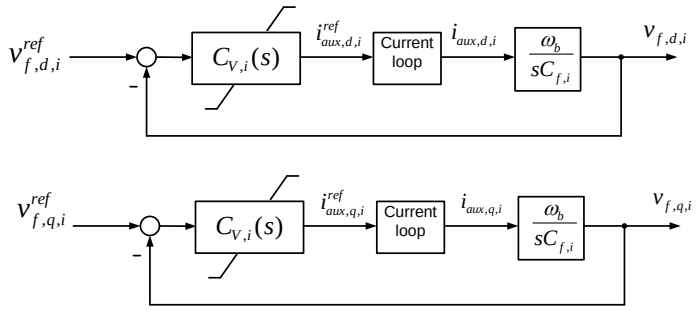

Figure 2.9: Voltage control loop of the GFM-VSC in $d-q$ axes.

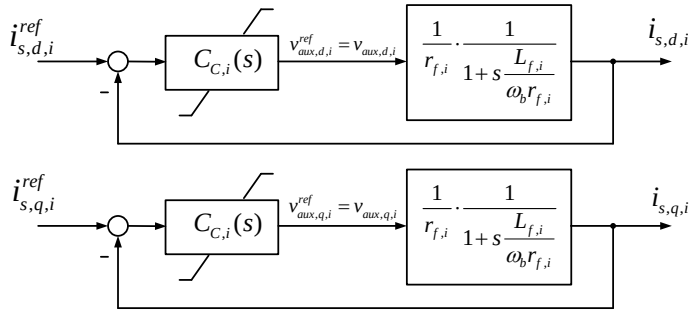

Figure 2.10: Curent control loop of the GFM-VSC in $d-q$ axes.

2.3 Self-synchronisation control strategy

Grid-forming converters can use different control strategies for achieving synchronisation. These methods include: the power-frequency ($p - f$) control droop, which is widely employed as a supplementary control for GFM-VSCs [**Rocabert'12**; **Olivares'14**]; the synchronverters [**Zhong'11**] or virtual synchronous machine (VSM) control [**DArco'15**; **Roldán-Pérez'19**] (with and without phase-locked loop (PLL)) commonly used in larger power systems, and the IP controller approache [**Qoria'20**c]. Chapter 3 will present a detailed analysis and comparison of these self-synchronisation methods, highlighting their advantages, limitations, and performance characteristics in various operating conditions. Figure 2.11 shows the general scheme of the implementation of a self-synchronisation control in GFM-VSCs. This thesis will use VSM control model without PLL as a benchmark due to its simplicity and potential for effective grid-forming operation. However, different self-synchronisation methods will be analysed in Chapter 3.

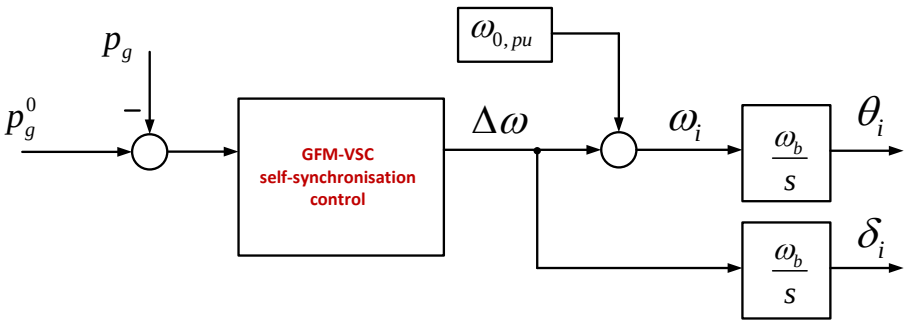

Figure 2.11: General block diagram of a self-synchronisation control in GFM-VSCs.

Virtual Synchronous Machine (VSM) control is a promising alternative that has gained significant attention in recent times. It is based on the concept of a virtual synchronous machine that emulates the behaviour of a physical synchronous machine by regulating its output voltage and frequency [**Choopani'20**; **Rokrok'20**]. This allows VSCs to operate in a grid-forming mode without needing a PLL or an external reference signal, simplifying the control scheme and improving the system's dynamic response. Two main variants exist for implementing VSM control: one without PLL, which regulates the voltage set point and angle of the GFM-VSC to mimic the behaviour

of a synchronous generator, and one with PLL, which employs a PLL control to help synchronize the VSC's output voltage with the grid [**DArco'15**; **Rokrok'20**].

A virtual synchronous machine (VSM) is implemented as a supplementary controller that manipulates the set points of the outer controllers of the GFM-VSC. Guidelines for the implementation of VSM controllers and different implementations can be found in [**DArco'15**; **Paolone'20**; **Choopani'20**; **Rokrok'20**; **Qoria'20**c]. This work considers a VSM supplementary controller emulating a classical model of a synchronous machine and equipped with a primary frequency controller, as shown in Figure 2.12.

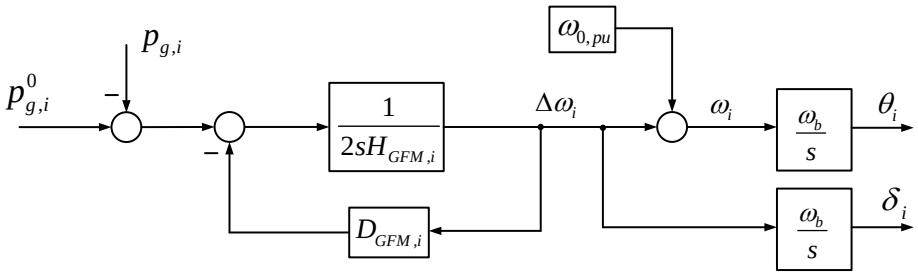

Figure 2.12: Supplementary controller of a virtual synchronous machine (VSM) implemented in a GFM-VSC.

where:

- $H_{GFM,i}$ (s) is the emulated inertia constant.
- $D_{GFM,i} = 1/R_{PFR,i}$ (pu) is the damping factor coefficient and the proportional gain of the primary frequency response (PFR) control). It is the inverse of the primary frequency droop constant ($R_{PFR,i}$).
- $\Delta\omega_i = \omega_i - \omega_{0,pu}$ (pu) is the frequency increment of the GFM-VSC ouput frequency, ω_i, with respect to the nominal frequency, $\omega_{0,pu} =$ 1 pu.
- $p^0_{g,i}$ (pu) is a constant active-power set point of the GFM-VSC at the PCC. This term represents the emulated mechanical power of the VSM.
- $p_{g,i}$ (pu) is the active-power delivered by the GFM-VSC measured at the PCC.

- ω_0 is the nominal frequency in rad/s.

2.4 Current limiter

Certain events can lead to overcurrent in power electronic converters in power systems. While power converters can provide a limited overload current compared to synchronous machines, it is important to limit the magnitude of the current, denoted as $i_{s,i}$, in order to prevent damage to the semiconductor switches. There are different methods for current limitations in GFM-VSCs, as will be discussed in Chapter 5. In this thesis, the GFM-VSC models use the most common general approach algorithm to limit the current, namely the current saturation algorithm (CSA) [**Qoria'20**c].

The current set points ($i_{s,d,i}^{ref'}$ and $i_{s,q,i}^{ref'}$) of Figure 2.7 are the outputs of the outer control loop:

$$\bar{i}_{s,i}^{ref'} = i_{s,d,i}^{ref'} + j i_{s,q,i}^{ref'} = i_{s,i}^{ref'} e^{j\delta_{is,i}^{ref'}} \tag{2.11}$$

The magnitude of the current set point, $i_{s,i}^{ref'}$, must be lower than or equal to the maximum current of VSC-i: $i_{s,i}^{max}$, as illustrated in Figure 2.13. Typical values of the maximum current are $i_{s,i}^{max} = 1 - 1.25$ pu. Current limitation algorithm obtains the saturated current set-point values ($i_{s,d,i}^{ref}$ and $i_{s,q,i}^{ref}$), as follows:

$$i_{s,d,i}^{ref} = \begin{cases} i_{s,i}^{max} \cos(\delta_{is,i}^{ref}) & if \quad i_{s,i}^{ref'} > i_{s,i}^{max} \\ i_{s,d,i}^{ref} = i_{s,d,i}^{ref'} & if \quad i_{s,i}^{ref'} \leq i_{s,i}^{max} \end{cases} \tag{2.12}$$

$$i_{s,q,i}^{ref} = \begin{cases} i_{s,i}^{max} \sin(\delta_{is,i}^{ref}) & if \quad i_{s,i}^{ref'} > i_{s,i}^{max} \\ i_{s,q,i}^{ref} = i_{s,q,i}^{ref'} & if \quad i_{s,i}^{ref'} \leq i_{s,i}^{max} \end{cases} \tag{2.13}$$

The algorithm has equal priority for both d-axis and q-axis currents; namely, the angle of the reference current does not change ($\delta_{is,i}^{ref} = \delta_{is,i}^{ref'}$). By implementing the CSA algorithm in GFM-VSC, it becomes possible to control and regulate the current within safe limits. This is crucial in maintaining the stability and integrity of the converter system, especially during transient conditions or grid disturbances.

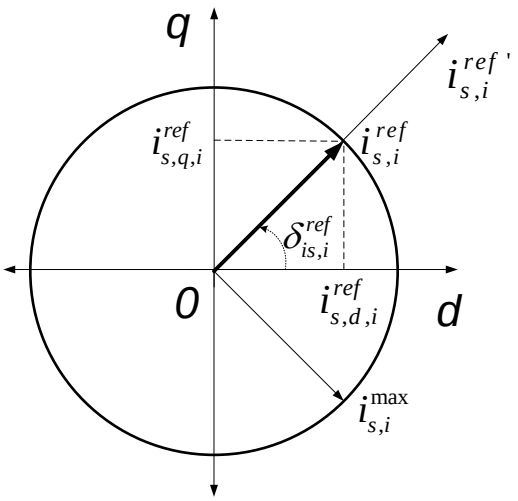

Figure 2.13: Current saturation algorithm (CSA).

2.5 Virtual impedance

Virtual impedance (VI) is a mathematical construct that mimics the behavior of a physical impedance. It is used to control the flow of power and stabilize electronic power systems. VI can be designed for different purposes such as reducing coupling between active and reactive power flows, mitigating harmonics, and improving fault ride-through capability [**Wang'15**]. The VI is also used to improve the stability and performance of VSCs, especially when several GFM-VSCs operate in parallel and the physical connection impedance is too small or do not have any connection transformer [**Rodríguez-Cabero'20**]. Adjusting the parameters of virtual resistance and inductance in VI can mitigate voltage fluctuations, improve power quality, and enhance system performance.

The virtual impedance method is not utilized in this thesis due to the GFM-VSC being connected to the grid through a transformer. This transformer is considered to have a relatively high impedance in the practical context of the proposal.

2.6 Simulation tools

Average electromagnetic-type models of power systems were used. Simulations were carried out with VSC_Lib tool, an open-source tool based on Matlab + Simulink + SimPowerSystems developed by L2EP-LILLE [**L2EP-LILLE'20**; **Qoria'18**a; **Qoria'19**]. Specifically, converters have been modelled using electromagnetic-type averaged models, including converter limitations such as current and voltage limits. System elements such as lines, loads, and controllers have been simulated in detail whereas converters have been modelled using electromagnetic-type averaged models, including converter limitations such as current and voltage limits.

2.7 Summary

This chapter can be summarised following the main points discussed in the previous sections:

- Grid-forming converters employ different self-synchronisation control strategies to achieve synchronisation. For this study, the VSM control without PLL is selected as the benchmark due to its simplicity and potential for effective grid-forming operation.
- The VSM control emulates the behaviour of a physical synchronous machine by regulating the output voltage and frequency.
- In GFM-VSCs, the current limiting mechanism utilises the current saturation algorithm (CSA) to restrict the magnitude of the current. This algorithm effectively prevents the current from surpassing a predetermined limit, safeguarding the semiconductor switches from potential damage.
- Virtual impedance is used to emulate the behaviour of a physical impedance in the converter's control loop. By adjusting the virtual impedance parameters, the converter can regulate the current and voltage response, providing stability and dynamic performance when several grid forming operate in parallel.

Chapter 3

Impact of GFM-VSC self-synchronisation control strategies on transient stability

3.1 Introduction

As previously discussed in Chapter 2, there are different options for self-synchronisation mechanisms in GFM-VSCs. This chapter analyses and compares the transient stability performance of different self-synchronisation methods for GFM-VSCs in various operating scenarios. The main focus is to compare the synchronising and controlling capabilities of the virtual synchronous machine (VSM) [**Choopani'20**; **Rokrok'20**; **DArco'15**] and an alternative approach using the IP controller [**Qoria'20**c] for GFM-VSCs in power systems.

The next four sections of the chapter present the rationale for this comparative performance analysis. Section 3.2 provides a review of previous work related to self-synchronisation control strategies for GFM-VSCs; Section 3.3 presents the gap covered by this chapter; Section 3.4 describes different self-synchronisation control strategies for GFM-VSCs; Section 3.5 presents the theoretical analysis of the equivalence and design the self-synchronisation mechanisms; Section 3.6 explains the virtual active power control (VAPC) method for GFM-VSCs; Section 3.7 presents the comparative performance analysis. First, it discusses the simulation results for load change, grid frequency change, and short circuit transient stability analysis. Then it analyses the performance of the VAPC and evaluates the critical clearing times. Fi-

nally, Section 3.8 provides the conclusions of this chapter.

3.2 Review of previous work

GFM-VSCs are emerging as a solution for integrating renewable energy resources (RERs) into electrical power systems under high penetration scenarios. The use of GFM-VSCs requires appropriate control algorithms to ensure stable and reliable operation of the system. These types of control strategies are essential for the operation of GFM-VSCs in island mode or during the reconnection process to the grid after a severe fault. In power systems with multiple GFM-VSCs, self-synchronisation strategies become essential when operating several GFM-VSCs in parallel. These strategies are necessary to ensure that all converters reach the same frequency in steady state [**Barker'21**]. One such strategy, virtual synchronous machine (VSM) control, has attracted considerable attention in power systems research. Unlike grid-following VSCs, a phase-locked loop (PLL) is not required for synchronisation, and supplementary control strategies can be used instead. The use of supplementary controller strategies for self-synchronisation of GFM-VSCs, typically emulates the behaviour of conventional synchronous machines. Several variants have been proposed in the literature, such as the power-synchronisation method [**Zhang'10**], the synchronverter control [**Zhong'11**], the active-power/frequency (P-f) droop control [**Rocabert'12**; **DArco'13**; **Olivares'14**], the virtual synchronous machine (VSM) control [**DArco'15**; **Roldán-Pérez'19**], the Integral-Proportional (IP) controller proposed in [**Qoria'20**c], among others.

Power-frequency (P-f) droop control is widely employed as a supplementary control for GFM-VSCs [**Rocabert'12**; **Olivares'14**]. Besides, in larger power systems, synchronisation is achieved through the use of synchronverters [**Zhong'11**] or virtual synchronous machines (VSM) [**Aouini'14**; **DArco'15**; **Roldán-Pérez'19**]. However, previous works [**DArco'13**] and [**DArco'14**] have shown that P-f droop and VSM supplementary controller are equivalent. Other different techniques for self-synchronisation of GFM-VSCs are the concept of virtual oscillator [**Arghir'18**; **Groß'19**], and reactive-power synchronisation method [**RodriguezA'21**]. The study in [**Arghir'18**] presents the approach for GFM-VSCs based on disturbance decoupling and voltage-power droop control strategies using an internal harmonic oscillator model. A similar approach, using a virtual-oscillator for synchronisation of GFM-VSCs, is presented in [**Groß'19**]. Meanwhile reactive-power synchroni-

sation approach [**RodriguezA'21**] separates synchronising power and active power control, leading to stable voltage and frequency.

The recent work in [**Qoria'20**c] introduces a novel concept, Integral-Proportional (IP) controller as an equivalent alternative of VSM using PLL [**DArco'15**]. The IP controller adds a proportional gain (K_p) to the active power control to mitigate damping oscillations, and compared with the VSM control (without PLL), this approach decouples the primary frequency response (PFR) control from the active power control. Another study [**Kanakesh'21**] proposes a virtual active-power control (VAPC) to improve system synchronisation after fault clearance. VAPC uses a feedback loop of the unsaturated power (virtual active power) calculated from the unsaturated current of the converter.

However, despite the efforts made in proposing GFM-VSC self-synchronisation strategies, there has been no comparative analysis of them so far. In order to provide a comprehensive understanding of the grid-forming self-synchronisation methods, it is important to examine the details of each approach. This chapter conducts a comparative analysis of different self-synchronisation control strategies, precisely the VSM control (with and without PLL) and IP controller technique. This chapter also investigates their impact on transient stability under different scenarios in GFM-VSCs. The models presented in this chapter serve as a basis for analysing and designing self-synchronisation strategies for GFM-VSCs. In the following sections, various methods and techniques proposed in the existing literature are discussed, and their effectiveness in achieving accurate synchronisation and stable grid integration is evaluated. These self-synchronisation methods are thoroughly examined in these sections, including their advantages, limitations and performance characteristics under different operating conditions in terms of transient stability. Through this comprehensive examination of control strategies, a deeper understanding of their capabilities can be obtained.

3.3 Gap covered by this chapter

Despite the efforts to propose GFM-VSC self-synchronisation strategies, there needs to be more literature regarding a comprehensive comparison and analysis of these strategies and their effects on transient stability. Specifically, previous work has yet to systematically examine the self-synchronisation strategies, including VSM control with and without Phase-Locked Loop (PLL) and the IP controller technique in GFM-VSCs. This chapter addresses this

research gap by conducting a thorough comparative analysis of these self-synchronisation control strategies. It delves into their impact on transient stability under various scenarios. Therefore, the contributions of this chapter are as follows:

- Analyses different self-synchronisation control strategies employed in GFM-VSCs: VSM control with and without PLL, IP controller and the VSM control without PLL using a wash-out filter.
- Theoretical analysis of the studied self-synchronisation control strategies for GFM-VSCs.
- Comparison the studied self-synchronisation control strategies of a GFM-VSC connected to an infinite grid under different scenarios in terms of transient stability.
- Evaluation the performance of the VAPC with the studied self-synchronisation control strategies of a GFM-VSC connected to an infinite grid under different scenarios in terms of transient stability.

3.4 Self-synchronisation control strategies of GFM-VSCs

This section discusses different self-synchronisation methods for the GFM-VSC control. The modelling and control are implemented in a d-q frame as explained in Chapter 2. The main concept of VSM control for self-synchronisation is analysed for a GFM-VSC connected to infinite grid using a L-filter as shown in Figure 3.1.

The following self-synchronisation mechanisms for GFM-VSCs will be analysed:

- Virtual synchronous machine (VSM) without phase-locked loop (PLL).
- VSM with PLL.
- Integral proportional (IP) controller.
- VSM without PLL + wash-out.

All the self-synchronisation strategies above mimic the behaviour of synchronous machines, in the sense that the GFM-VSC is able to behave as a voltage source connected to the system through an impedance and it is able to operate in synchronism with the rest of the system.

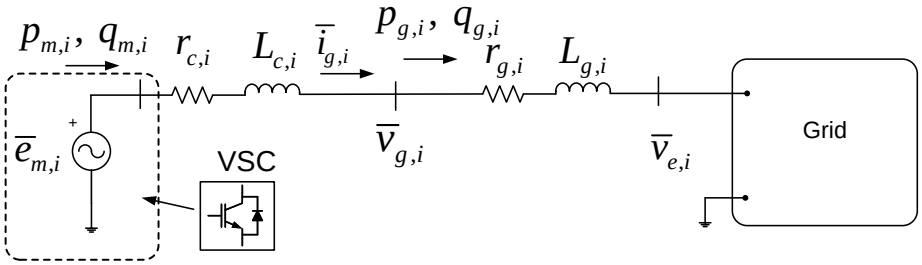

Figure 3.1: Equivalent model of a Grid-Forming Voltage Source Converter GFM-VSC connected to the grid.

3.4.1 VSM without PLL

The VSM is a supplementary controller used to mimic the behaviour of a synchronous generator in order to regulate the voltage angle of a GFM-VSC [**DArco'14**; **Choopani'20**; **Rokrok'20**]. The VSM is utilised as a control algorithm for the VSC to emulate the swing equation (3.1) of a synchronous machine, which eventually imposes the frequency, ω_i (pu), of the GFM-VSC, as shown in Figure 3.2).

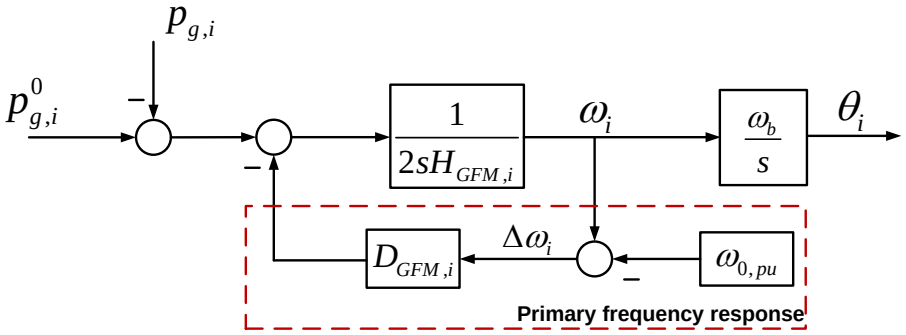

Figure 3.2: Supplementary controller of a virtual synchronous machine (VSM) implemented without PLL in a GFM-VSC.

The swing equation of the VSM reads:

$$p^0_{g,i} - p_{g,i} - D_{GFM,i}\Delta\omega_i = 2H_{GFM,i}\frac{d\Delta\omega_i}{dt} \tag{3.1}$$

where:

- $H_{GFM,i}$ (s) is the emulated inertia constant.
- $D_{GFM,i}$ is the damping factor coefficient. For the VSM control without PLL, the parameter $D_{GFM,i}$ also serves as control of the primary frequency response (PFR)), which is the inverse of the primary frequency droop constant, $R_{PFR,i}$ ($D_{GFM,i} = 1/R_{PFR,i}$ (pu)).
- $\Delta\omega_i = \omega_i - \omega_{0,pu}$ (pu) is the frequency increment of the GFM-VSC ouput frequency, ω_i, with respect to the nominal frequency, $\omega_{0,pu}$ = 1 pu.
- $p^0_{g,i}$ (pu) is a constant active-power set-point of the GFM-VSC at the PCC. This term represents the emulated mechanical power of the VSM.
- $p_{g,i}$ (pu) is the active-power delivered by the GFM-VSC measured at the PCC.
- $\omega_b = \omega_0$ is the nominal frequency in rad/s.

The main characteristics of VSM - without PLL are as follows

- The GFM-VSC does not use a PLL.
- The GFM-VSC provides an inertial response, due to the emulated inertia constant $H_{GFM,i}$ (s).
- The damping factor coefficient, $D_{GFM,i}$, plays two roles simultaneously: (a) to provide damping and (b) to contribute to an instantaneous primary frequency response. Notice that it is mandatory that the primary frequency support is instantaneous, because, otherwise, the dynamic response of the GFM-VSC could be jeopardised. Notice also that if a typical value for the proportional gain of the frequency controller is used (e.g. $D_{GFM,i}$ = 20 pu), then the dynamic response of the GFM-VSC is determined.

3.4.2 VSM with PLL

VSM control with PLL is another method for controlling the voltage set-point and the angle of a GFM-VSC. This approach employs a traditional PLL to synchronise the output voltage of the VSC with the grid [**DArco'15**; **Rokrok'20**] providing a stable reference frequency for the VSC. By using a PLL, the GFM-VSC imposes its frequency, facilitating its synchronisation with the frequency at the PCC and it can thus maintain synchronous operation with the grid. Figure 3.3 illustrates the block diagram of the VSM with PLL of a GFM-VSC, equipped with primary frequency response (PFR) control loop, while the block diagram of the PLL equipped with an anti-windup is shown in Figure 3.4.

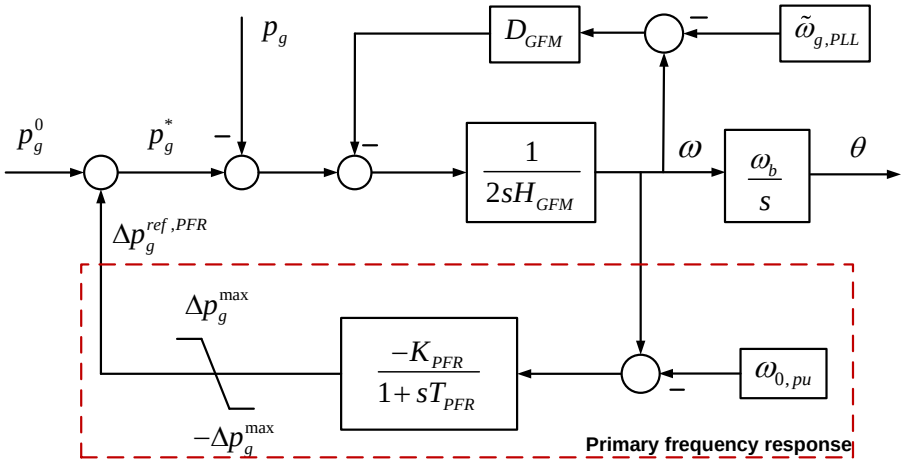

Figure 3.3: IP controller block diagram using PFR control support for synchronisation in a GFM-VSC.

The VSM swing equation, which describes the dynamics of the virtual synchronous machine, is given by the same Equation (3.1). The implementation of Eq. (3.1) for both configurations of the VSM control is the same. The key distinction is that, in this case, the deviation of the VSC angular frequency $\Delta\omega_i$, instead of using the nominal frequency ($\omega_{0,pu} = 1$ pu), this is obtained from the (estimated) grid frequency by using the PLL:

$$\Delta\omega_i \approx \omega_i - \hat{\omega}_{g,PLL,i} \tag{3.2}$$

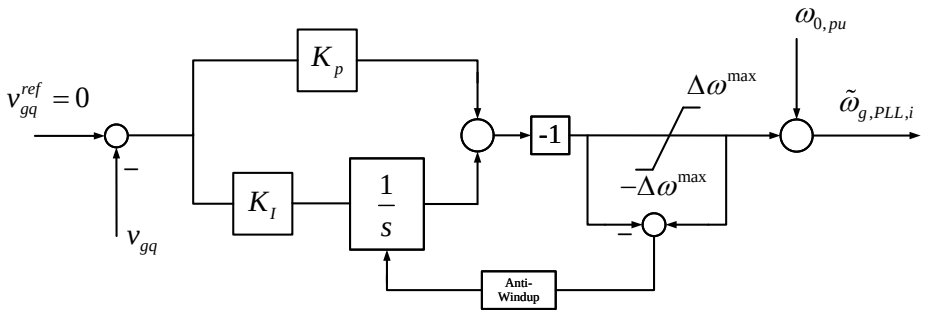

Figure 3.4: PLL block diagram equipped with an anti-windup.

where ω_i is the angular frequency of the VSC, $\omega_{g,i}$ is the grid frequency and the $\hat{\omega}_{g,PLL,i}$ is the estimated grid frequency by the PLL.

Notice that although this GFM-VSC self-synchronisation scheme uses a PLL, the application is totally different to the use of a PLL in grid-following converters.

The main characteristics of VSM with PLL are as follows

- The GFM-VSC uses a PLL.
- The GFM-VSC provides an inertial response, due to the emulated inertia constant $H_{GFM,i}$ (s).
- The damping coefficient, $D_{GFM,i}$, is used to obtain the required damping ratio of the dynamic response of the GFM-VSC.
- The controller of the primary frequency response of the GFM-VSC is decoupled from the power control. Therefore, if the primary frequency response support is requered by the GFM-VSC, then an external control loop can be added to the VSM control as shown in Figure 3.3. The PFR control can be made as slow as required (time constant $T_{PFR,i}$). The proportional gain, $K_{PFR,i}$, can be designed using typical values for this application (e.g. $K_{PFR,i} = 20$ pu, and the damping of the dynamic response of the GFM-VSC is not jeopardised, because the damping coefficient, $D_{GFM,i}$, can be designed to achieve the required damping ratio. Notice also, that if primary frequency controller is not used (e.g. $K_{PFR,i} = 0$ pu), the GFM-VSC controls its active-power injection to a constant value (e.g. $p_{g,i} = p_{g,i}^0$).

3.4.3 IP controller

The IP controller is another approach for controlling GFM-VSC power converters described in [**Qoria'20**c]. This type of controller adds a proportional action (K_p) to the active power to provide damping, as shown in Figure 3.5.

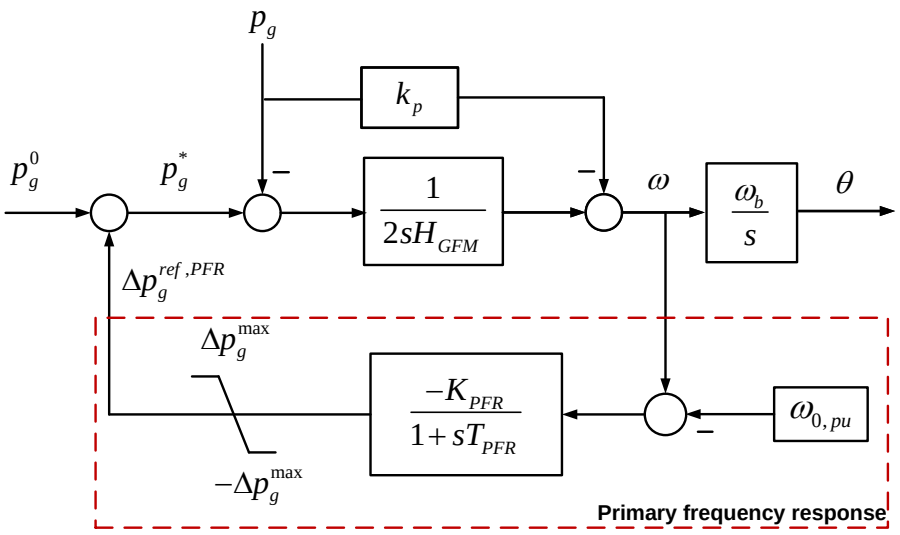

Figure 3.5: IP controller block diagram using PFR control support for synchronisation in a GFM-VSC.

The main characteristics of IP controller are as follows:

- The GFM-VSC does not use a PLL.
- The GFM-VSC provides an inertial response, due to the emulated inertia constant $H_{GFM,i}$ (s).
- The proportional gain, K_p, is used to obtain the required damping ratio of the dynamic response of the GFM-VSC.
- The primary frequency controller of the GFM-VSC is decoupled from the self-synchronisation control. Then an external control loop for PFR support can be added to the GFM-VSC control (Figure 3.5).

- As will be explained in Section 3.5, the behaviour of IP controller under small disturbances is equivalent to the behaviour of VSM with PLL strategy [**Qoria'20**c].

3.4.4 VSM without PLL + wash-out

Figure 3.6 shows the scheme of the VSM without PLL incorporating a wash-out filter with a time constant $T_{WD,i}$. This high-pass filter remains inactive during steady states but it acts during the transient [**DIgSILENT'22**; **Mo'17**].

The main characteristics of VSM without PLL - washout are as follows:

- The GFM-VSC does not use a PLL.
- The GFM-VSC provides an inertial response, due to the emulated inertia constant $H_{GFM,i}$ (s).
- The damping coefficient, $D_{GFM,i}$, is used to obtain the required damping ratio of the dynamic response of the GFM-VSC.
- The primary frequency controller of the GFM-VSC is decoupled from the power control, due to the washout filter.

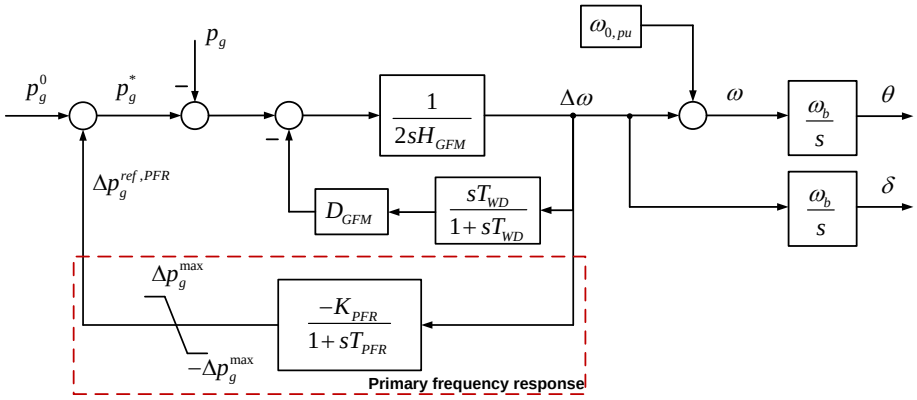

Figure 3.6: Virtual synchronous machine (VSM) control without PLL using wash-out filter and (PFC) support for synchronisation in a GFM-VSC.

3.5 Theoretical analysis of self-synchronisation mechanisms and design

This section presents a theoretical analysis of the self-synchronisation mechanisms described in Section 3.4. The objectives of the analysis are as follows:

- Examine the behaviour of the self-synchronisation mechanisms of a GFM-VSC connected to an infinite grid under small disturbances (Figure 3.1, where an infinite grid is assumed).
- Analyse the equivalence of certain self-synchronisation mechanisms, and emphasis on the differences of other ones under certain conditions.
- Provide useful insight into the design of the parameters of the self-synchronisation mechanisms.

In order to simplify the analysis, the primary frequency response (PFR) controller will not be considered. Naturally, the only case in which the PFR controller will be present is in the VSM without PLL, because it is implicit in its configuration.

A GFM-VSC connected to an infinite grid, as in Figure 3.1 is considered. The complex power and current injected by the GFM-VSC are given by:

$$\overline{s}_{g,i} = \overline{v}_{g,i}\overline{i}^{*}_{g,i} \;;\; \overline{i}_{g,i} = \frac{\overline{e}_{m,i} - \overline{v}_{g,i}}{\overline{z}_{c,i}}. \tag{3.3}$$

Then, the active-power injection of the GFM-VSC reads:

$$p_{g,i} = \Re_e\{\overline{s}_{g,i}\} = \Re_e\left\{\left(\frac{\overline{e}_{m,i} - \overline{v}_{g,i}}{\overline{z}_{c,i}}\right)^{*}\right\} \tag{3.4}$$

where:

$$\overline{e}_{m,i} = e_{m,i}e^{j\theta_{m,i}} \text{ and } \overline{v}_{g,i} = v_{g,i}e^{j\theta_{g,i}}. \tag{3.5}$$

Assuming the converter is connected to a transmission system, the resistance is usually much smaller than the reactance ($x_i >> r_i$). Therefore, to simplify the analysis, it is assumed that $\overline{z}_{c,i} = jx_{c,i}$:

$$p_{g,i} = \frac{e_{m,i}v_{g,i}}{x_{c,i}}\sin(\theta_i - \theta_{g,i}) \tag{3.6}$$

where the phase angle deviation is $\Delta\theta_i = \theta_i - \theta_{g,i}$, $e_{m,i}$ is the VSC's internal voltage amplitude, $v_{g,i}$ is the grid voltage amplitude, $x_{c,i}$ is the equivalent

grid impedance, θ_i is the phase angle of the VSC voltage, and $\theta_{g,i}$ is the voltage phase angle at the PCC.

$$p_{g,i} = \frac{e_{m,i} v_{g,i}}{x_{c,i}} \sin(\Delta\theta_i) \tag{3.7}$$

In small signal analysis, $\sin(\Delta\theta_i) \approx \Delta\theta_i$, and in steady state, $e_{m,i} = 1$ and $e_{g,i} = 1$. Using these assumptions, the expression of the active-power $p_{g,i}$, in steady state, can be simplified as shown in Eq. (3.8):

$$p_{g,i} = \left.\frac{\Delta\theta_i}{x_{c,i}}\right|_{\substack{\sin(\Delta\theta_i)=\Delta\theta_i \\ e_{m,i}=1 \\ v_{g,i}=1}} \tag{3.8}$$

The angle difference $\Delta\theta_i$ can be calculated in terms of the angular frequency $\Delta\omega_i$ using Eq. (3.9):

$$\Delta\theta = \frac{1}{s}\omega_b(\omega_i - \omega_{g,i}) \tag{3.9}$$

where ω_b is the base frequency of the system in rad/s ($2\pi 50$ rad/s).

3.5.1 VSM without PLL

In VSM without PLL control scheme, the frequency increment, $\Delta\omega_i = \omega_i - \omega_{0,pu}$, can be obtained from Eq. (3.1) in terms of active power in the frequency domain:

$$\Delta\omega_i = \frac{1}{2H_{GFM,i}s + D_{GFM,i}} p^0_{g,i} - \frac{1}{2H_{GFM,i}s + D_{GFM,i}} p_{g,i} \tag{3.10}$$

If the grid is infinite and strong ($x_{g,i}$ is low), then one can assume that:

$$\omega_{g,i} \approx \omega_{e,i} = \omega_{0,pu} = 1 \text{ pu.} \tag{3.11}$$

and Eq. (3.12) reads:

$$\Delta\theta = \frac{1}{s}\omega_b \Delta\omega_i \tag{3.12}$$

By replacing Eq. (3.12) in Eq. (3.8), the active power expression yields:

$$p_{g,i} = \frac{1}{x_{c,i}s}\omega_b \Delta\omega_i \tag{3.13}$$

Substituting the expression for $\Delta\omega$ given in Eq. (3.10) into Eq. (3.13):

$$p_{g,i} = \frac{1}{x_{c,i}s}\omega_b \left[\frac{1}{2H_{GFM,i}s + D_{GFM,i}} p^0_{g,i} - \frac{1}{2H_{GFM,i}s + D_{GFM,i}} p_{g,i} \right] \quad (3.14)$$

Rearranging to obtain the transfer function $T_{(s)} = p_{g,i}/p^0_{g,i}$:

$$T_{(s)} = \frac{p_{g,i}}{p^0_{g,i}} = \frac{\left(\frac{\omega_b}{2H_{GFM,i}x_{c,i}} \right)}{s^2 + \frac{D_{GFM,i}}{2H_{GFM,i}} s + \frac{\omega_b}{2H_{GFM,i}x_{c,i},i}} \quad (3.15)$$

Using the standard form, by definition, of the transfer function for a second-order system [**Pagola'06**; **Ogata'10**]:

$$F(s) = \frac{\omega_n^2}{s^2 + 2\zeta\omega_n s + \omega_n^2} \quad (3.16)$$

By aligning the corresponding terms of the two transfer functions (Eq. (3.15) and Eq. (3.16)), the damping ratio, ζ, and the natural frequency, ω_n, are given by:

$$\zeta = \frac{D_{GFM,i}}{4H_{GFM,i}} \frac{1}{\omega_n}, \quad \omega_n = \sqrt{\frac{\omega_b}{2H_{GFM,i}x_{c,i}}}. \quad (3.17)$$

There are two equations (3.17) and four parameters ($H_{GFM,i}$, $D_{GFM,i}$, ζ and ω_n).

In VSM without PLL, the primary frequency controller is included implicitly in the damping factor coefficient: $D_{GFM,i} = 1/R_{PFR,i}$, where $R_{PFR,i}$ is the droop constant. Normally, primary frequency controllers use proportional gains of $D_{GFM,i} = 20 - 25$ pu. Hence, the design of the parameters of the VSM without PLL self-synchronisation strategy is given by:

- Specified parameters for the design: Emulated inertia constant ($H_{GFM,i}$) and damping coefficient ($D_{GFM,i}$).
- Calculated parameters: damping ratio (ζ) and natural frequency (ω_n), given by (3.17).

It is important to recall that, in VSM without PLL the damping coefficient $D_{GFM,i}$ has to be specified (because it is also the proportional gain of the primary frequency controller), the the damping ratio of the dynamic response of the GFM-VSC is given, which can be lower than desired. And this is a disadvantage of this self-synchronisation strategy.

3.5.2 VSM with PLL

In VSM with PLL control scheme, the frequency increment, $\Delta\omega_i = \omega_i - \hat{\omega}_{g,PLL,i}$, can be obtained from Eq. (3.1):

$$\Delta\omega_i = \frac{1}{2H_{GFM,i}s + D_{GFM,i}} p^0_{g,i} - \frac{1}{2H_{GFM,i}s + D_{GFM,i}} p_{g,i} \tag{3.18}$$

Under the assumption that the estimated frequency at the connection point of the GFM-VSC ($\omega_{g,PLL}$) is similar to the true frequency at this bus (ω_g):

$$\Delta\omega_i = \omega_i - \omega_{g,i} \tag{3.19}$$

$$\omega_g \approx \hat{\omega}_{g,PLL,i} \tag{3.20}$$

$$\Delta\omega_i \approx \omega_i - \hat{\omega}_{g,PLL,i} \tag{3.21}$$

where ω_i is the frequency imposed by the GFM-VSC.

By performing the same analytical procedure as in Subsection 3.5.1 (Eqs. (3.13)-(3.17)), it is proved that the dynamic behaviour of VSM with PLL is equivalent to the one without PLL (under small disturbances and under the assumptions described in this section). However, there is an important difference related to the design of the parameters. Since in VSM with PLL the primary frequency controller is decoupled, parameter D_{GFM} can be selected to obtain the required damping ratio of the dynamic response of the GFM-VSC. Specifically, the design of the parameters of the VSM with PLL self-synchronisation strategy is given by:

- Specified parameters for the design: Emulated inertia constant ($H_{GFM,i}$) and damping ratio (ζ).
- Calculated parameters: Damping coefficient ($D_{GFM,i}$) and natural frequency (ω_n):

$$D_{GFM} = \zeta\sqrt{\frac{4H_{GFM,i}\omega_b}{x_{c,i}}}, \quad \omega_n = \sqrt{\frac{\omega_b}{2H_{GFM,i}x_{c,i}}}. \tag{3.22}$$

3.5.3 IP controller

Figure 3.7 shows the block diagram of the IP controller using a proportional gain of K_p to provide damping to the GFM-VSC.

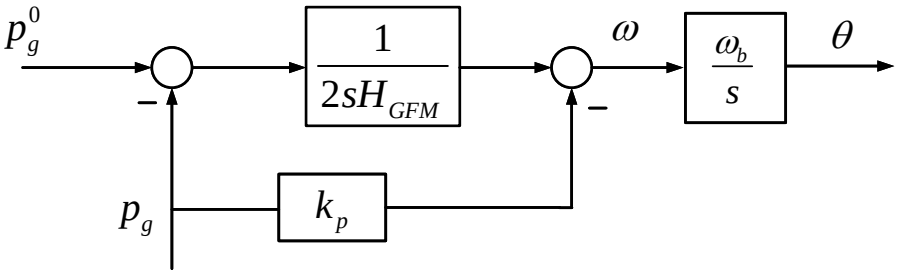

Figure 3.7: IP controller block diagram used in a GFM-VSC for synchronisation.

To obtain ω_i from the block diagram of the Figure 3.7, Eq. (3.23) is used.

$$\omega_i = \frac{1}{2H_{GFM,i}s}p^0_{g,i} - \frac{1}{2H_{GFM,i}s}p_{g,i} - K_{p,i}p_{g,i} \tag{3.23}$$

where, the active power in steady-state is given by:

$$p_{g,i} = \frac{1}{x_{c,i}}\Delta\theta_i\Big|_{\sin(\Delta\theta_i)=\Delta\theta_i} \tag{3.24}$$

If the GFM-VSC is connected to a strong grid, ($\omega_{g,i} \approx \omega_{e,i} = \omega_{0,pu} = 1\ pu$), and by using Eq. (3.8) in Eq. (3.9), the Eq. (3.25) can be used to obtain the active power in terms of the frequency:

$$p_{g,i} = \frac{1}{x_{c,i}s}\omega_b(\omega_i - \omega_{g,i}) \tag{3.25}$$

Replacing (3.23) in (3.25) yields:

$$\begin{aligned} p_{g,i} = {} & \frac{\omega_b}{2H_{GFM,i}x_{c,i}s^2 + 2H_{GFM,i}K_{p,i}\omega_b s + \omega_b}p^0_{g,i} - \\ & \frac{2H_{GFM,i}s^2}{2H_{GFM,i}x_{c,i}s^2 + 2H_{GFM,i}K_{p,i}\omega_b s + \omega_b}\theta_{g,i} \end{aligned} \tag{3.26}$$

The transfer function $T_{(s)} = P_g/P_g^0$ reads:

$$T(s) = \frac{\frac{\omega_b}{2H_{GFM,i}x_{c,i}}}{s^2 + \frac{K_{p,i}\omega_b}{x_{c,i}}s + \frac{\omega_b}{2H_{GFM,i}x_{c,i}}} \tag{3.27}$$

Matching to a second-order transfer function, the natural frequency is given by:

$$\omega_n^2 = \frac{\omega_b}{2H_{GFM,i}x_{c,i}} \qquad \Rightarrow \qquad \omega_n = \sqrt{\frac{\omega_b}{2H_{GFM,i}x_{c,i}}} \tag{3.28}$$

Therefore, the gain $K_{p,i}$ of the IP controller is:

$$\frac{K_{p,i}\omega_b}{x_{c,i}} = 2\zeta\omega_n \qquad \Rightarrow \qquad K_{p,i} = \frac{2\zeta x_{c,i}\omega_n}{\omega_b} \tag{3.29}$$

$$K_{p,i} = \zeta\sqrt{\frac{4x_{c,i}^2\omega_b}{2H_{GFM,i}(x_{c,i}\omega_b)^2}} = \zeta\sqrt{\frac{2x_{c,i}}{H_{GFM,i}\omega_b}} \tag{3.30}$$

This control approach offers one degree of freedom by selecting a constant damping ratio ζ to adjust the gain value $K_{p,i}$. However, it is not possible to directly set the response time and natural frequency ω_n, as they depend on both $H_{GFM,i}$ and the connection impedance $x_{c,i}$.

The design parameters for the IP controller approach are as follows:

- Specified parameters for the design: Emulated inertia constant ($H_{GFM,i}$) and damping ratio (ζ).

- Calculated parameters: Gain $K_{,i}p$ and natural frequency (ω_n), which are determined using the following equations:

$$K_{p,i} = \zeta\sqrt{\frac{2x_{c,i}}{H_{GFM,i}\omega_b}} \quad \text{and} \quad \omega_n = \sqrt{\frac{\omega_b}{2H_{GFM,i}x_{c,i}}}. \tag{3.31}$$

To decouple the PFR control from power control, a control loop for the PFC is added. The controller takes the difference between the frequency deviation and reference frequency as input and outputs an active-power set point. The PFR adds a proportional active-power set point based on the frequency deviation and a saturation parameter prevents excessive control actions.

3.5.4 VSM without PLL + wash-out

For the theoretical analysis of VSM without PLL using a wash-out filter, it is assumed that:

- During the transient, the wash-out filter is neglected:

$$\frac{T_{WD,i}s}{1+T_{WD,i}s} \approx 1 \tag{3.32}$$

- In steady state, the washout-out filter does not have any impact:

$$\frac{T_{WD,i}s}{1+T_{WD,i}s} \approx 0 \tag{3.33}$$

Hence, during the transient, the behaviour of VSM without PLL with washout is equivalent to the case of VSM without PLL and without wash-out filter. Therefore, the frequency increment $\Delta\omega_i = \omega_i - \omega_{0,pu}$ imposed by the GFM-VSC, which can be obtained from Eq. (3.1), has the same dynamic behaviour as the case without washout filter, and the analysis carried out in (3.13)-(3.17) is valid.

However, the washout filter does not act in steady state. Hence, the behaviour of VSM without PLL and with washout is equivalent to the behaviour of VSM with PLL (Subsection 3.5.2). As a consequence, VSM without PLL and with washout also decouples the primary frequency controller. Hence, the design of the parameters of the VSM with PLL self-synchronisation strategy is given by:

- Specified parameters for the design: Emulated inertia constant ($H_{GFM,i}$) and damping ratio (ζ). damping coefficient ($D_{GFM,i}$).
- Calculated parameters: Damping coefficient ($D_{GFM,i}$) and natural frequency (ω_n):

$$D_{GFM,i} = \zeta\sqrt{\frac{4H_{GFM,i}\omega_b}{x_{c,i}}}, \quad \omega_n = \sqrt{\frac{\omega_b}{2H_{GFM,i}x_{c,i}}}. \tag{3.34}$$

3.5.5 Equivalence between VSM and IP controller

The IP controller and the VSM with PLL decouple the frequency support control from the power control and both approaches are equivalent. This section shows the equivalence between the VSM and the IP controller [**Qoria'20**c].

Eq. (3.35) results from the block diagram in Figure 3.7, where ω_i is obtained in terms of active power:

$$\omega_i = \frac{1}{2H_{GFM,i}s}p^0_{g,i} - \frac{1}{2H_{GFM,i}s}p_{g,i} - K_{p,i}p_{g,i} \tag{3.35}$$

The active-power injection $p_{g,i}$ at the PCC can be expressed as:

$$p_{g,i} = \frac{1}{x_{c,i}s}\omega_b(\omega_i - \hat{\omega}_{g,PLL,i}) \tag{3.36}$$

Replacing $K_{c,i} = 1/x_{c,i}$ and Eq. (3.36) in Eq. (3.35):

$$\omega_i = \frac{1}{2H_{GFM,i}s}p^0_{g,i} - \frac{1}{2H_{GFM,i}s}p_{g,i} + K_{p,i}\frac{K_{c,i}}{s}\omega_b(\omega_i - \hat{\omega}_{g,PLL,i}) \tag{3.37}$$

Finally, Eq. (3.37) can be rewrited as follows:

$$2H_{GFM,i}s\omega_i = p^0_{g,i} - p_{g,i} + \underbrace{2H_{GFM,i}K_{p,i}K_{c,i}\omega_b}_{D_{GFM,i}}(\omega_i - \hat{\omega}_{g,PLL,i}) \tag{3.38}$$

where $D_{GFM,i} = 2H_{GFM,i}K_{p,i}K_{c,i}\omega_b$.

The block diagram of the equivalence between the VSM with PLL and the IP controller is shown in Figure 3.8.

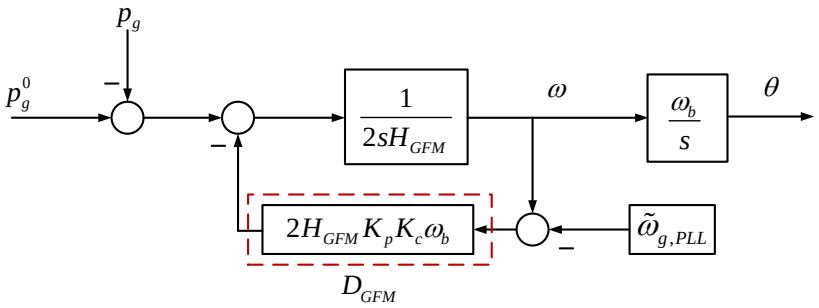

Figure 3.8: Equivalence Block diagram between the VSM (with PLL) and the IP controller.

3.6 Virtual active power control (VAPC)

The virtual active power control (VAPC) was proposed in [**Kanakesh'21**] to improve transient stability in GFM-VSC. Specifically, VAPC control improves transient stability by control actions when the GFM-VSC enters into the current limitation process [**Laba'23**]. In VAPC, the GFM-VSC uses as feedback signal of the self-synchronisation mechanism the *unsaturated virtual active power*, $p_{g,i}^{virt}$, instead of the measured active power injection, as shown in Figure 3.9. Notice that VAPC is compatible with any self-synchronisation mechanism in GFM-VSCs.

The unsaturated virtual active power used in VAPC ($p_{g,i}^{virt}$ in Figure 3.9) is calculated as follows:

$$p_{g,i}^{virt} = v_{g,d,i} \cdot i_{s,d,i}^{ref'} + v_{g,q,i} \cdot i_{s,q,i}^{ref'} \tag{3.39}$$

where $v_{g,d}$ and $v_{g,q}$ are the voltage components at PCC and $i_{s,d,i}^{ref'}$ and $i_{s,q,i}^{ref'}$ are the unsaturated current set points.

All details and analysis of VAPC control can be found in [**Kanakesh'21**]. The behaviour of VAPC when implemented in different self-synchronisation mechanisms will be analysed in this chapter of the thesis.

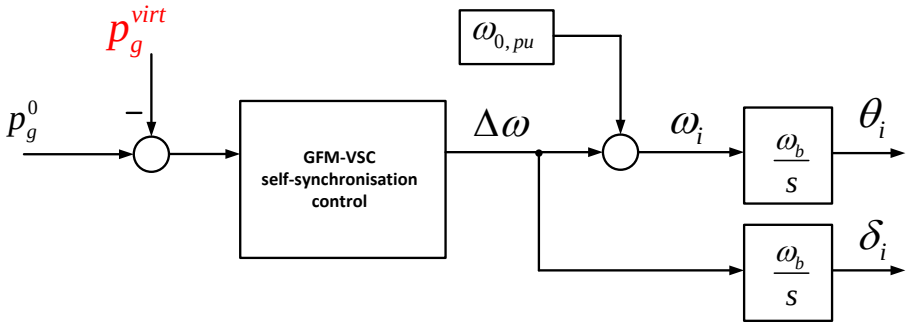

Figure 3.9: General block diagram of a self-synchronisation control in GFM-VSCs using the virtual active power $p_{g,i}^{virt}$ as a feedback measurement.

3.7 Case studies

This section compares the impact of four different power control strategies in grid-forming converters in three different scenarios. The case of the study

consists of a test power system of 100 MVA GFM-VSC connected to an infinite grid. Figure 3.10 shows the one-line diagram of the study system, whose system data is provided in the Appendix A. As indicated in Table A.1, the converters have a current saturation algorithm with equal priority d-axis and q-axis currents. Simulations were carried out with VSC_Lib tool, an open-source tool based on Matlab + Simulink + SimPowerSystems developed by L2EP-LILLE [**L2EP-LILLE'20**; **Qoria'18**a; **Qoria'19**].

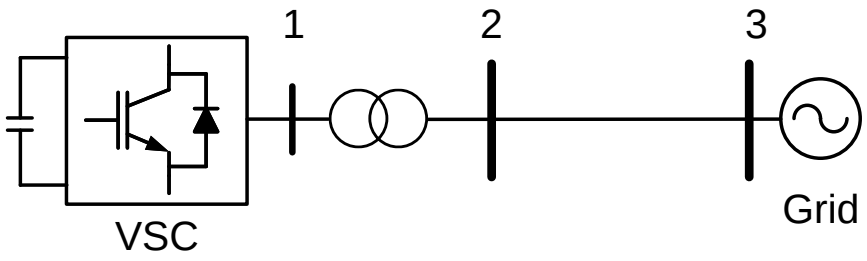

Figure 3.10: GFM-VSC connected to an infinite bus.

3.7.1 Calculation of the parameters D_{GFM} and K_p

For the case of VSM with PLL and WSM without PLL using wash-out filter, the damping factor coefficient (D_{GFM}) is obtained using the equations (3.22) and (3.34). Meanwhile the K_p gaing is obtained from equation (3.30).

- **VSM with PLL and WSM without PLL + wash-out**:

$$D_{GFM,i} = \zeta \sqrt{\frac{4H_{GFM,i}\omega_b}{x_{c,i}}} = 203 \ pu \tag{3.40}$$

- **IP controller**:

$$K_{p,i} = \zeta \sqrt{\frac{2x_{c,i}}{H_{GFM,i}\omega_b}} = 0.0096 \ pu \tag{3.41}$$

where:

  - The converter inertia constant is $H_{GFM} = 5$ s.
  - The connection impedance is $x_{c,i} = 0.15$ pu.
  - The damping ratio is $\zeta = 0.7$.
  - The base frequency is $\omega_b = 2\pi 50$ rad/s.

- **VSM without PLL**:

  The VSM control with PLL, VSM without PLL + wash-out and the IP controller are implemented with primary frequency respopnse (PFR) support. Meanwhile, VSM without PLL does not need an additional PFR control loop because it is capable of providing frequency support to the system. Therefore, the D_{GFM} value should be set to provide damping and primary frequency response simultaneously:

  - $D_{GFM} = 20$ pu.

  Furthermore, the case of VSM control without PLL using $D_{GFM} = 203$ pu will be analysed:

  - $D_{GFM} = 203$ pu.

  Notice that the case of VSM control without PLL using $D_{GFM} = 203$ pu is only for theoretical comparison purposes as it is not feasible in practice. Hence, any frequency variation would result in a very large deviation in the power injected by the converter according to Equation (3.1). The coupling the power control of the converter to the PFR control, as will be shown later in Subection 3.7.3.2, jeopardises the dynamic response of the system.

Therefore, this chapter compared the performance of the four self-synchronisation configurations considering the following five cases:

- VSM without PLL ($D_{GFM} = 20$ pu).
- VSM without PLL ($D_{GFM} = 203$ pu).
- VSM with PLL ($D_{GFM} = 203$ pu).
- IP controller ($K_p = 0.0096$ pu).
- VSM without PLL + wash-out ($D_{GFM} = 203$ pu, $T_{WD} = 2$ s).

3.7.2 Simulation under different scenarios

This section compares the five cases for the self-synchronisation of the GFM-VSC under four different events:

- Small-signal stability
  - Load change: a load addition of 5% of the rated power at the GFM-VSC terminal at $t = 1$ s.
  - Grid frequency change: from 50 Hz to 50.5 Hz (from 1 pu to 1.01 pu) at $t = 1$ s.
- Transient stability (large-signal stability)
  - Short circuit without VAPC: fault of 150 ms duration at the PCC at $t = 0.1$.
  - Short circuit with VAPC: fault of 150 ms duration at the PCC at $t = 0.1$.

3.7.3 Small-signal stability

3.7.3.1 Load change

A load of 5% of the nominal power is added at the GFM-VSC terminal (Bus 2 in Figure 3.10) at $t = 1$ s. Figure 3.11 illustrates the angle difference between the converter and the grid ($\delta - \delta_e$) as well as the frequency variation of the VSC after the load change. The converter decreases the angle difference keeping the GFM-VSC frequency at its nominal value (50 Hz) and, thus, controlling the active power of the converter to its setpoint value. In the case of the VSM without PLL ($D_{GFM} = 20$ pu), the generator exhibits an oscillatory behaviour due to its low damping coefficient value. However, the converter has a damped response for the remaining cases after the load change.

The active and reactive power injections of the GFM-VSC are shown in Figure 3.12. Faced with a small disturbance, the VSC's active power injection tries to recover its initial operating point value. Meanwhile, the VSC increase the reactive power value to compensate for the change in the angle difference. On the one hand, the non-PLL VSM case, using $D_{GFM} = 20$ pu, presents so many oscillations before raising the final operating point. On the other hand, in the rest of the cases (the VSM without PLL with and without wash-out filter ($D_{GFM} = 203$ pu), VSM with PLL and the IP controller), the converter has a better response faced with the load change.

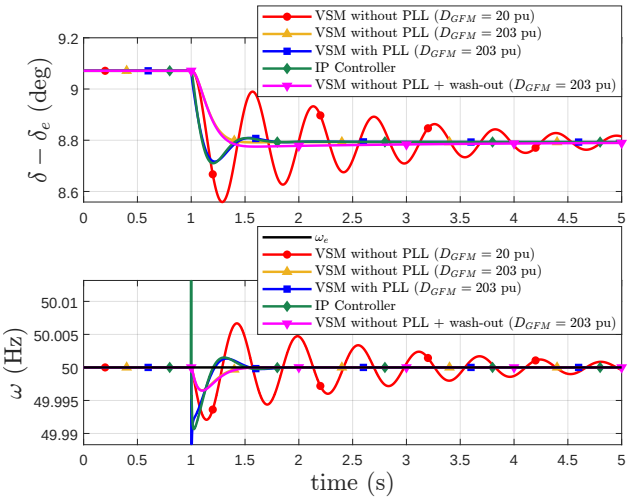

Figure 3.11: Load change of 5% of the nominal power. (top) Angle difference and (bottom) frequency variation of the GFM-VSC.

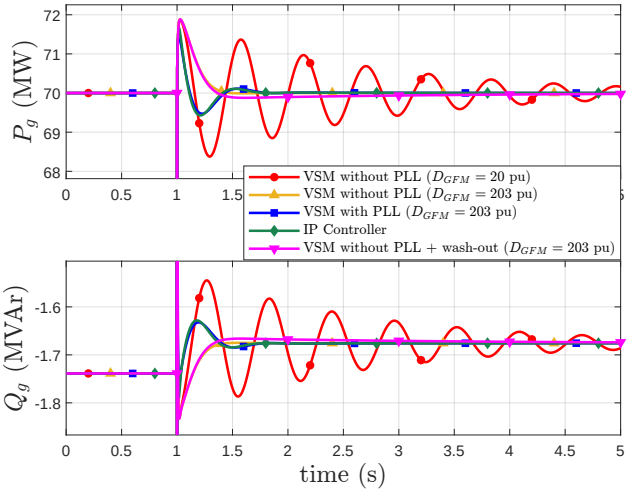

Figure 3.12: Load change of 5% of the nominal power. (top) Active power and (bottom) reactive power of the GFM-VSC.

Figure 3.13 illustrates the comparison of the estimated frequency $\hat{\omega}_g$, the VSC frequency ω, and the grid frequency ω_e during a 5% load change of nominal power in the case of VSM with PLL. The VSC frequency ω tracks the grid frequency ω_e closely, while the frequency $\hat{\omega}_g$ estimated by the PLL has a larger deviation with respect to the grid frequency. Although the frequency estimated by the PLL does not follow the grid frequency accurately, the converter tracks the grid frequency according to the swing equation (3.1).

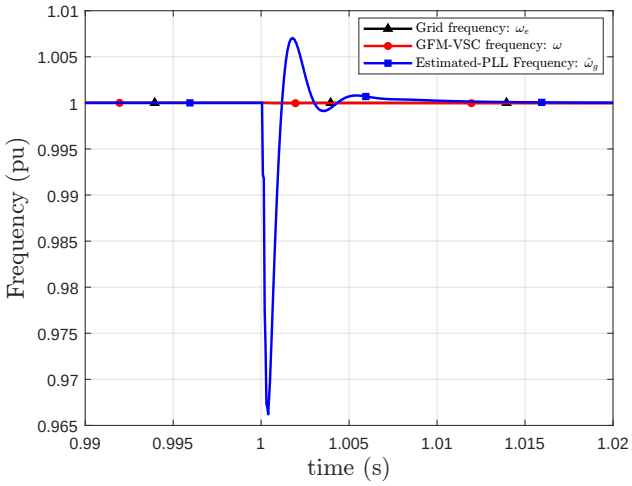

Figure 3.13: Load change of 5% of the nominal power. Comparison of the estimated frequency $\hat{\omega}_g$, the VSC frequency ω, and the grid frequency ω_e of VSM with PLL.

The results indicate that the VSM with PLL and the IP controller exhibit the best performance when subjected to small signal perturbations, followed by the VSM without PLL + wash-out (with a damping factor coefficient of $D_{GFM} = 203$ pu). In contrast, the VSM without PLL (with a damping factor coefficient of $D_{GFM} = 20$ pu) exhibits oscillations during and after the transient due to its low damping factor coefficient, resulting in a poor damped system response.

3.7.3.2 Grid frequency change

A 1% change in the grid frequency is applied at t = 1 s from 50 Hz to 50.5 Hz. The angle difference of the GFM-VSC with respect to the grid ($\delta - \delta_e$) and the frequency deviation of the converter are shown in Figure 3.14. Figure 3.14

(bottom) shows the tracking of the grid frequency by the converter in all five cases. However, for the cases of the VSM with PLL and the IP controller, the angle difference suffers a small deviation under a small change in the grid frequency, as shown in the upper part of Figure 3.14. Meanwhile, the cases of the VSM without PLL (with and without wash-out filter) present larger deviations in the angle difference.

On the one hand, the angle difference deviation in the VSM without PLL (without wash-out filter) is a consequence of the power variation ($\Delta p_{g,i} = p^0_{g,i} - p_{g,i}$) according to (3.1). $\Delta p_{g,i}$ is directly proportional to the change in the frequency deviation $\Delta\omega_i$ and the damping factor coefficient D_{GFM}. By using a $D_{GFM} = 20$ pu, the converter produces a poorly damped response, with several oscillations before the final operation point rise. By using $D_{GFM} = 203$ pu, a small change in the grid frequency produces a large deviation of the GFM-VSC active power due to the high D_{GFM} value as shown in Figure 3.15. On the other hand, although the VSM without PLL + wash-out has a large deviation during the fault, it reaches the final operation point similar to the VSM with PLL and the IP controller and different to the VSM without PLL (without wash-out filter). This action is performed because the washout filter is activated during the transient, allowing the GFM-VSC control action. It is then deactivated in the steady state to prevent a greater deviation of the GFM-VSC active power injection (refer to Figure 3.15).

Figure 3.15 displays the active and reactive power injections of the GFM-VSC while Figure 3.16 shows voltage and the current injection of the converter. As previously mentioned, a high D_{GFM} value can lead to a large deviation in the GFM-VSC active power when a small change in grid frequency occurs, as observed in the case of the VSM without PLL (without wash-out). The converter modulates the voltage e_m at 1pu, so by reducing the active power, the current injection of the converter also decreases, causing the voltage v_g to increase according to Eq.(3.7). This response increases the reactive power to compensate for the voltage variation. However, when using the VSM without PLL + wash-out, WSM with PLL, or the IP controller, they decouple the primary frequency response from the power controller, enabling them to compensate for the voltage variation without affecting the active power. In this way, these controllers avoid large deviations in the angle difference and the GFM-VSC active power during grid frequency disturbances. Additionally, the PFC and washout filter utilised in the VSM without PLL + wash-out enables it to reach the final operating point similarly to the VSM with PLL and the IP controller, further improving its performance.

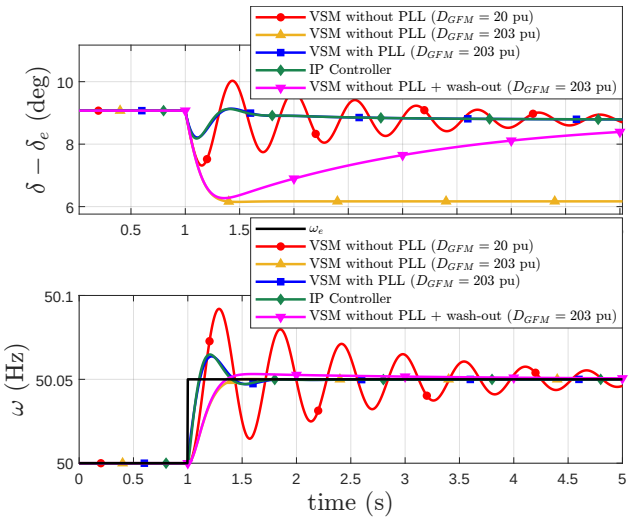

Figure 3.14: Change in the grid frequency of 1% (0.01 pu). (top) Angle difference and (bottom) Frequency of the GFM-VSC.

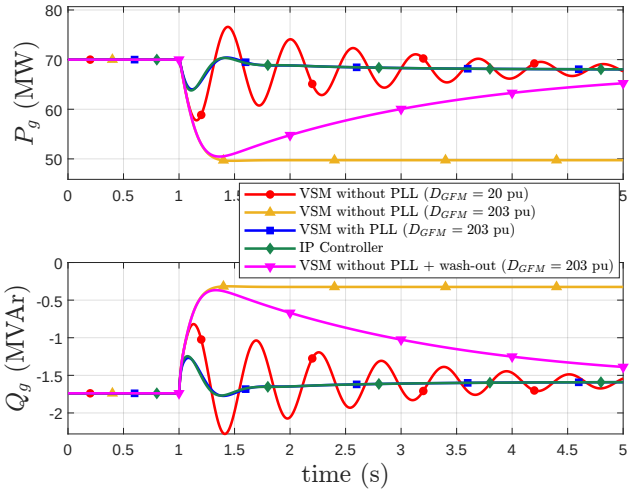

Figure 3.15: Change in the grid frequency of 1% (0.01 pu). (top) Active and (bottom) reactive power of the GFM-VSC.

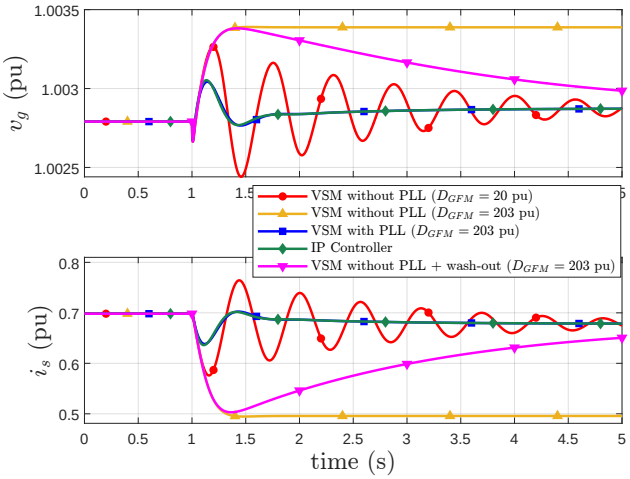

Figure 3.16: Change of the grid frequency of 1% (0.01 pu). (top) voltage at the terminal and (bottom) Current injection of the GFM-VSC.

Figure 3.17 illustrates the comparison of the estimated frequency $\hat{\omega}_g$, the VSC frequency ω, and the grid frequency ω_e for a grid frequency change of 1% in the case of VSM with PLL. Although the PLL tracks the grid frequency ω_e, it's important to note that the VSC frequency ω displays a more significant deviation following the grid frequency based on the VSM swing equation.

The analysis indicates that the VSM with PLL ($D_{GFM} = 203$ pu) and the IP controller exhibit superior frequency tracking and power-sharing performance compared to other methods, followed by the VSM without PLL + wash-out. However, the VSM without PLL ($D_{GFM} = 20$ pu) displays a significant frequency and power oscillation. While the VSM without PLL ($D_{GFM} = 203$ pu) has good frequency tracking, it has the highest power output deviation.

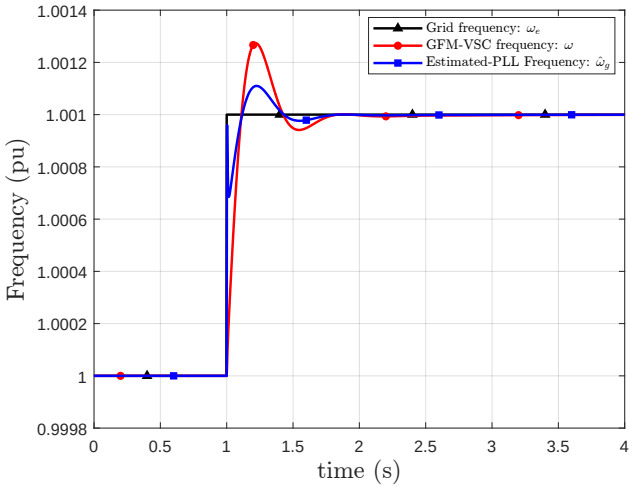

Figure 3.17: Change in the grid frequency of 1% (0.01 pu). Comparison of the estimate frequency $\hat{\omega}_g$, the VSC frequency ω, and the grid frequency ω_e of VSM with PLL.

3.7.4 Large-signal stability (transient stability)

3.7.4.1 Short circuit simulation without VAPC

A three-phase-to-ground short circuit is applied to the line 2-3, which is close to bus 2, and it is cleared 150 ms later. In Figure 3.18, the angle difference between the GFM-VSC and the grid ($\delta - \delta_e$) as well as the frequency deviation of the VSC with respect to the grid frequency are shown. For the short-circuit event, synchronisation is maintained in all cases. However, the IP controller shows the maximum angle difference and frequency deviation. This reflects a tendency to lose synchronism for faults that are not much higher than 150 ms.

After the fault clearing, the VSM without PLL using a $D_{GFM} = 20$ pu exhibits oscillations before reaching the steady state due to the low damping factor value. Conversely, the VSM without PLL (with and without wash-out filter) and the VSM with PLL present a smaller deviation of the angle difference and the frequency of the GFM-VSC. This is because the PLL helps to synchronise the VSC with the grid frequency, while the wash-out filter improves the control performance during dynamic conditions.

Figure 3.19 displays the VSC's active and reactive power injections, and

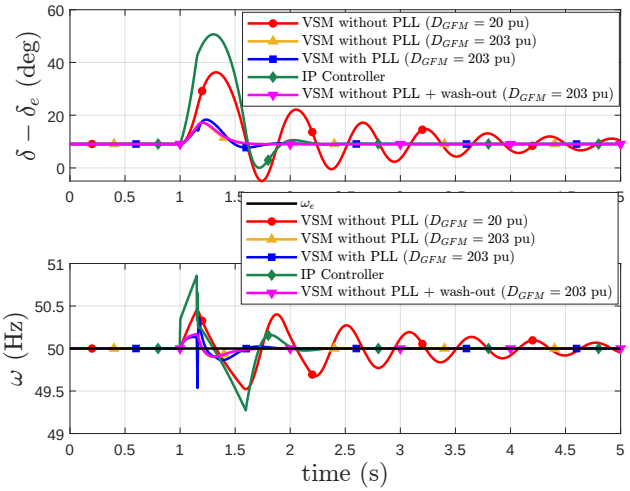

Figure 3.18: Fault at the VSC terminal cleared after 150 ms. (top) Angle difference and (bottom) Frequency of the GFM-VSC.

Figure 3.20 shows the voltages and the current injections of the VSC. During the fault, the active power injection experiences a sharp drop, triggering the converter current limiter (see Figure 3.20) and accelerating the converter. Once the fault is cleared, the active power injection sharply rises to the limit set by the current limiter ($i_{s,i}^{max} = 1.25$ pu).

Figure 3.21 illustrates the comparison of the estimated frequency $\hat{\omega}_g$, the VSC frequency ω, and the grid frequency ω_e for a short circuit event at the VSC terminal cleared after 150 ms, in the case of VSM with PLL. For a large disturbance, the PLL helps to the VSC frequency ω tracks the grid frequency ω_e according to the swing equation. For example, During the fault, when the converter output power is zero ($p_{g,i} = 0$) and the estimated frequency by the PLL is equal to the maximum value of the PLL frequency ($\hat{\omega}_{PLL,i} = \hat{\omega}_{PLL,i}^{max}$), the acceleration of the converter is reduced, thereby avoiding the loss of synchronism:

$$\frac{d\Delta\omega_i}{dt} = \frac{1}{2H_{GFM,i}} \left(p_{g,i}^0 - p_{g,i} - D_{GFM,i}(\omega_i - \hat{\omega}_{PLL,i}^{max})\right) \tag{3.42}$$

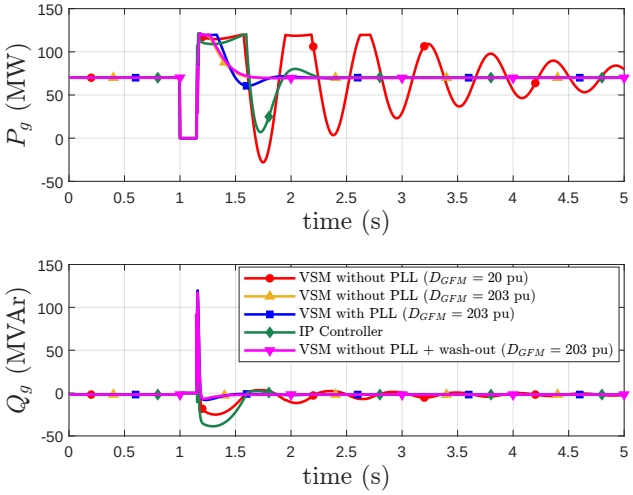

Figure 3.19: Fault at the VSC terminal cleared after 150 ms. (top) Active and (bottom) Reactive of the GFM-VSC.

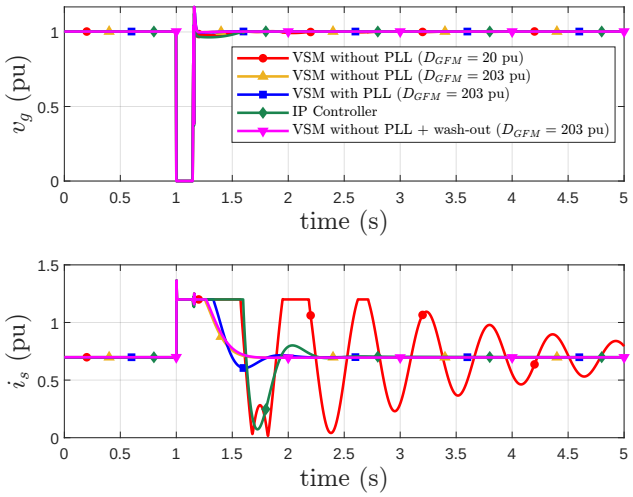

Figure 3.20: Fault at the VSC terminal cleared after 150 ms. (top) voltage at the terminal and (bottom) Current injection of the GFM-VSC.

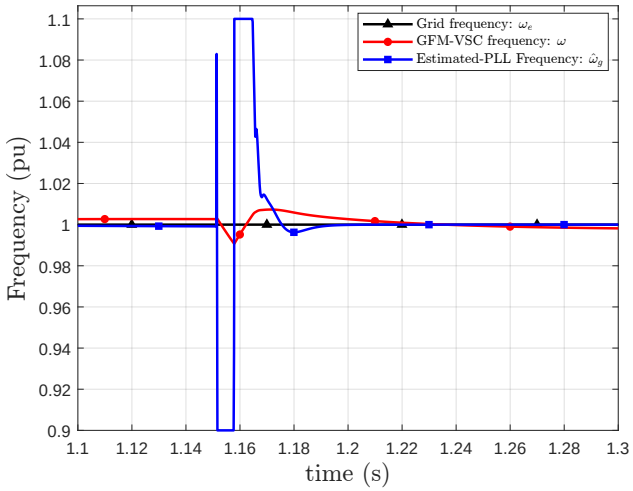

Figure 3.21: Fault at the VSC terminal cleared after 150 ms. Comparison of the estimate frequency $\hat{\omega}_g$, the VSC frequency ω, and the grid frequency ω_e of VSM with PLL.

Both VSMs with and without PLL (with and without wash-out filter), using the damping factor coefficient of $D_{GFM} = 203$ pu, exhibit a fast response for synchronisation and quickly reach a steady state. In contrast, the IP controller and the VSM without PLL, with $D_{GFM} = 20$ pu, show a slower response. However, the IP controller is more damped and reaches a steady state faster than the VSM without PLL ($D_{GFM} = 20$ pu), which results in an underdamped response before reaching the steady-state.

3.7.4.2 Performance of the virtual power controller (VAPC)

The performance of the virtual power controller is evaluated for the short circuit event. The same three-phase-to-ground short circuit is applied to the line 2-3 and cleared 150 ms later. The upper part of Figure 3.22 shows the angle difference between the GFM-VSC and the grid ($\delta - \delta_e$), while the lower part shows the frequency deviation of the VSC with respect to the grid frequency. The results indicate that the system maintains synchronism for the short circuit scenario when the VAPC is applied for synchronisation.

The IP controller shows the maximum angle difference and frequency deviation during the fault reaching the final operating point after the fault clearing. However, compared to when the VAPC is not applied, the IP

controller exhibits a faster response. Moreover, the VSM without PLL using a $D_{GFM} = 20$ pu exhibits oscillations before reaching the steady state, whereas VSM with PLL and VSM without PLL (with and without wash-out filter) using a $D_{GFM} = 203$ pu have the best performance on the system response.

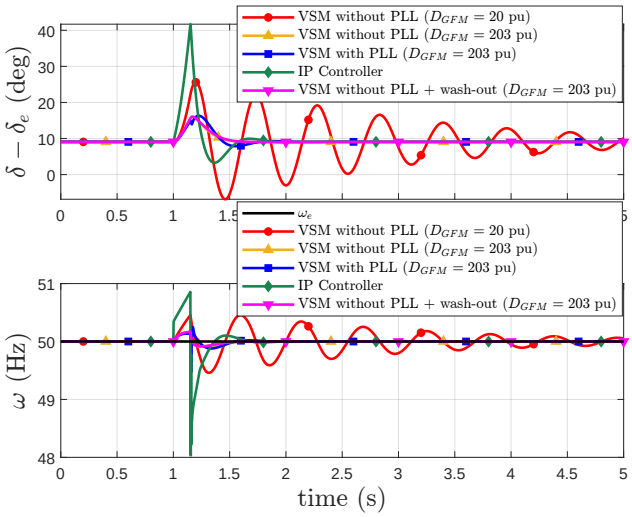

Figure 3.22: Fault at the VSC terminal cleared after 150 ms applying Virtual power control (VPC). (top) Angle difference and (bottom) Frequency of the GFM-VSC.

Figure 3.23 shows the active and reactive power injections of the VSC during the short circuit event. As the fault occurs, there is a sudden drop in the active power injection, causing the converter current limiter to activate (as seen in the lower part of Figure 3.24). This causes the converter to accelerate. Once the fault is cleared, the active power injection sharply rises to the limit set by the current limiter ($i_{s,i}^{max} = 1.25$ pu), avoiding the loss of synchronism. Notice that the current limiter is activated in less time than when the VAPC is not used (see Subsection 3.7.4.1)

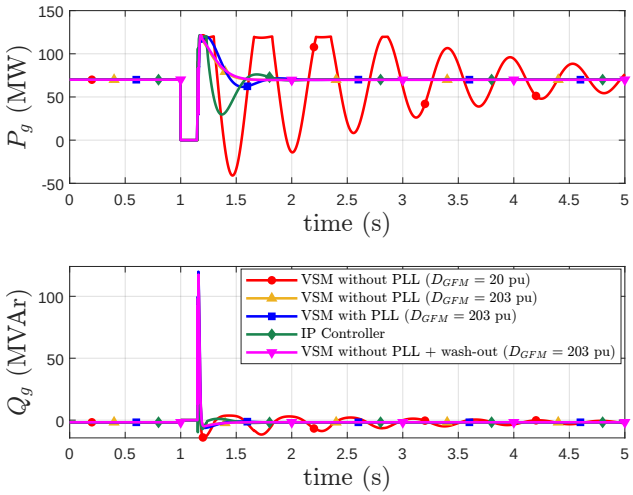

Figure 3.23: Fault at the VSC terminal cleared after 150 ms applying VPC. (top) Active and (bottom) Reactive of the GFM-VSC.

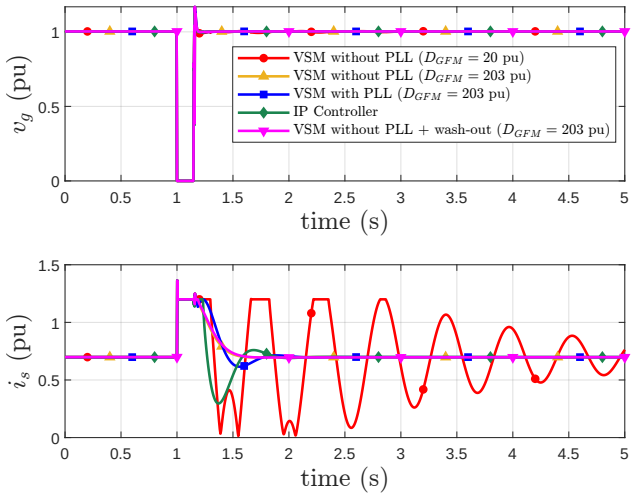

Figure 3.24: Fault at the VSC terminal cleared after 150 ms applying VPC. (top) voltage at the terminal and (bottom) Current injection of the GFM-VSC.

Figure 3.25 illustrates the comparison of the estimated frequency $\hat{\omega}_g$, the VSC frequency ω, and the grid frequency ω_e for a short circuit event using VAPC of the case of VSM with PLL. The fault is applied at the VSC terminal cleared after 150 ms. For a large disturbance, the VSC frequency ω tracks the grid frequency ω_e closely by the action of the power control and PFR of the GFM-VSC. MeanWhile the frequency $\hat{\omega}_g$, which the PLL estimates, has a larger deviation with respect to the grid frequency during and after the fault clearing.

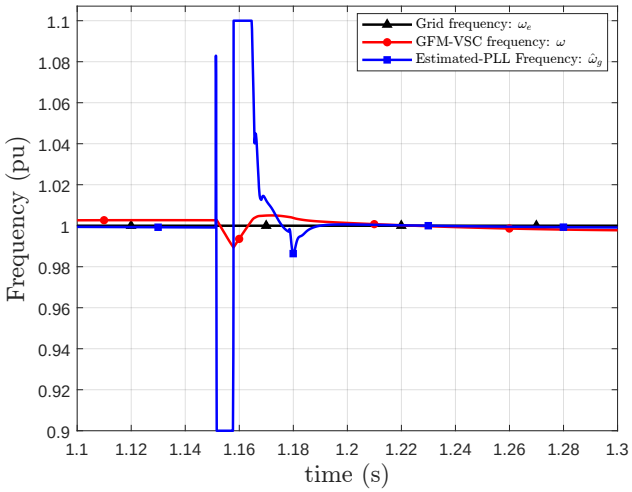

Figure 3.25: Fault at the VSC terminal cleared after 150 ms applying VPC. Comparison of the estimate frequency $\hat{\omega}_g$, the VSC frequency ω, and the grid frequency ω_e of VSM with PLL.

The results demonstrate that the VSM without PLL ($D_{GFM} = 203$ pu) and VSM with PLL have the best performance in terms of recovering the final operation point after the fault is cleared. While the IP controller manages to recover from the fault, it takes slightly longer than the VSM with PLL, showing that their behaviours differ in large disturbance events. On the other hand, the VSM without PLL ($D_{GFM} = 20$ pu) has the worst performance because, as in the previous scenarios, it shows oscillations after the fault has been cleared due to its low damping coefficient, with a large current overshoot that raises the current limits several times.

3.7.5 Critical clearing times

In order to assess transient stability, it is necessary to determine the critical clearing time (CCT). The CCT is a measure used to quantify the transient stability margins of a power system. This is defined as the maximum duration that a fault may persist without causing a loss of synchronism. The CCT is a widely used metric for evaluating the margin of transient stability **[Gomez-Exposito'17]**. Table 3.1 presents the CCT values in milliseconds (ms) for different GFM-VSC control strategies.

Table 3.1 shows that the VSM without PLL using a damping factor coefficient of $D_{GFM} = 203$ pu and the VSM with PLL using the same damping factor have the highest CCTs of 1600ms and 1700ms, respectively. In contrast, the VSM without PLL with a damping factor coefficient of $D_{GFM} = 20$ pu has a lower CCT with 280ms, indicating a worse transient stability margin.

The IP controller has a CCT of 190ms, which means it has the worst transient stability margin compared to other tested control strategies. Although the IP controller is similar to the VSM with PLL in small signal analysis, it is not the same for large disturbances. The VSM control with PLL has a good performance for short-circuit events compare to the IP controller. This is because, during a fault, the converter output power is zero ($p_{g,i} = 0$) which leads to the acceleration of the GFM-VSC as per the equivalent swing equation obtained in (3.23):

$$\frac{d\Delta\omega_i}{dt} = \frac{1}{2H_{GFM,i}} p^0_{g,i} \tag{3.43}$$

Table 3.1: Critical clearing times (CCTs).

GFM-VSC control strategy	**CCT** (ms)	
	Without VAPC	with VAPC
VSM without PLL ($D_{GFM} = 20$ pu)	280	540
VSM without PLL ($D_{GFM} = 203$ pu)	1600	2640
VSM with PLL ($D_{GFM} = 203$ pu)	1700	3440
VSM without PLL + wash-out ($D_{GFM} = 203$ pu)	1020	1900
IP controller	190	390

Furthermore, Table 3.1 also demonstrates the CCTs improvements using VAPC. The results indicate that the VAPC is more suitable for situations where a quick response is required to maintain synchronisation, such as when

large disturbances.

3.8 Conclusions

The conclusions obtained in this chapter can be summarised as follows:

- The four self-synchronisation mechanisms for GFM-VSCs analysed in this chapter (VSM without PLL, VSM with PLL, VSM without PLL + wash-out and IP controller) can have a similar behaviour under small disturbances, for a proper tuning of the parameters. However, they can have different behaviour under large disturbances, due to non-linearities.
- Strategies VSM with PLL and VSM without PLL + washout produce the best results in terms of transient stability.
- Strategies VSM without PLL and IP control produce the lowest critical clearing times (CCTs).
- The Virtual active-power controller (VAPC) improves the CCTs in all cases, and it can be applied to all self-synchronisation strategies in GFM-VSCs.

Chapter 4

Fast voltage boosters to improve transient stability

4.1 Introduction

This chapter proposes control strategies based on voltage/reactive-power control of GFM-VSCs to improve the transient stability of power systems with 100% GFM-VSC-based generation. The proposed strategies are called fast voltage boosters (FVBs) because each GFM-VSC modifies its voltage set point to improve transient stability. The proposed FVBs do not modify the set points linked to frequency/active-power injection. One control strategy utilises local measurements, while the other relies on global measurements of the frequency of the centre of inertia (COI). Both strategies have demonstrated significant improvement in the transient stability of the power systems. Theoretical analysis and simulation results are presented to validate the effectiveness of the proposed strategies.

The rest of the chapter is organised as follows. Section 4.2 provides a review of previous work on control strategies for improving the transient stability of GFM-VSC-based power systems. Section 4.3 presents the gap covered by this chapter. Section 4.4 presents the proposed fast voltage boosters, including the local fast voltage booster (FVB-L) and the fast voltage booster using a wide-area communication system (FVB-WACS). The design and operation principles of these strategies are discussed in detail. In Section 4.5, simulation results are presented to validate the effectiveness of the proposed strategies. This section includes a comprehensive analysis of various aspects of the proposed strategies, including short-circuit simulations, critical

clearing times (CCTs), the impact of communication latency, the design and impact of the control parameters. This section also discusses the use of local and global measurements for the proposed strategies. Finally, Section 4.6 summarises the conclusions of this chapter.

4.2 Review of previous work

Control strategies based on voltage/reactive-power control are an alternative approach to active power control strategies. There is a notable area of research and development in the design of control mechanisms specifically focused on reactive power control strategies in GFM-VSCs. In addition, the effect of converter output voltages and reactive power injections on transient stability has been studied in [**Pan'19**]. The work in [**Pan'19**] analyses the behaviour of a GFM-VSC (with voltage/reactive-power droop control) connected to an infinite grid. It shows that increasing the steady-state reactive power setpoint of the VSC's Q-V control droop increases the transient stability margin. However, specific voltage/reactive-power control strategies for improving transient stability in GFM-VSC have not been studied in [**Pan'19**].

The work in [**Chen'22**] proposes a method to improve the transient angle stability of a GFM-VSC connected to an infinite grid. The proposed method uses a voltage/reactive-power control on a GFM-VSC by changing its voltage setpoint, which changes the relationship between the reference voltage and the angle deviation. The proposed control strategy uses local measurements. The proposed voltage control strategy improves transient stability.

Authors in [**Xiong'21**b] proposed a voltage/reactive-power method in GFM-VSCs controlled with QV droop control to improve transient stability. In the proposed method a supplementary reactive-power set point is added to the reactive-power set point of the QV droop control of the GFM-VSC. The supplementary set point consists of a feedback signal of the frequency difference between the VSM and the grid (e.g., it uses local measurements). The proposed control strategy improves transient stability in a test system of a GFM-VSC connected to an infinite grid.

The work in [**Si'23**] proposes a control system that utilizes two methods to improve the transient stability of GFM-VSCs. These methods are voltage amplitude regulation and reactive power injection. They use local measurements and they are analysed in a test system consisting of a GFM-VSC connected to an infinite grid. The authors show that the proposed methods improve transient stability.

Although the proposed voltage/reactive-power control strategies for proposed in GFM-VSCs [**Xiong'21**b; **Chen'22**; **Si'23**] aim to improve transient stability, it does not guarantee its feasibility in multi-converter systems, as the control is specifically designed for a GFM-VSC connected to an infinite grid. In multi-converter systems, transient stability phenomenon is more complex. Therefore, more advanced and specific controls are required to ensure transient stability in multi-converter systems.

The use of control strategies based on voltage/reactive-power control to improve transient stability in power systems with 100 % converter has not been carefully investigated. While these types of approaches have been implemented in shunt FACTS devices [**Haque'04**] and VSC-HVDC systems [**Fuchs'14**; **Sigrist'15**; **Renedo'17**], they have only been applied as reactive-power control-based strategies in GFL-VSC converters. Alternatively, voltage/reactive-power control-based strategies have also been successfully applied to synchronous generators [**Lee'86**; **Kundur'94**] called excitation boosters [**Díez-Maroto'19**b; **Diez-Maroto'17**; **Díez-Maroto'19**a; **Díez-Maroto'20**] (EBs) in multi-machine systems. The successful implementation of EB strategies in the aforementioned systems has inspired the research presented in this chapter. In particular, EB strategies can help improve transient stability during a fault since synchronous generators do not require a current limiter for fault protection. However, control actions in GFM-VSC must guarantee their activation after fault clearance since no control action is effective during the current limitation of GFM-VSCs.

In this sense, this chapter proposes two fast voltage booster control strategies based on voltage/reactive-power to improve transient stability in power systems with 100% of GFM-VSC-based generation. The proposed strategies (to be called Fast Voltage Boosters -FVBs- in the rest of the chapter) are based on changing the voltage set points of GFM-VSC, quickly when a fault occurs. Such action should eventually change the electrical active-power injections of the GFM-VSC and would pull the frequencies of the GFM-VSCs in the system together, helping to maintain synchronism. One of the proposed strategies uses local measurements, whereas the other uses global measurements to calculate the frequency of the COI. The chapter will show that both strategies improve transient stability of these types of systems significantly with the advantage that the converter will change its reactive-power injection without affecting set points for active-power injections (directly related to frequency control). In other words, these types of strategies do not involve changing set points of the primary energy sources of GFM-VSCs.

4.3 Gap covered by this chapter

Voltage/reactive-power supplementary controllers for GFM-VSCS to improve transient stability have only been analysed in the converter connected to an infinite bus. However, there could be limitations to their application successfully in multi-converter systems, especially in power systems with 100% GFM-VSC-based generators. Therefore, the successful implementation of these types of strategies in the multi-machine systems has inspired the research presented in this chapter with the challenge of guaranteeing the feasibility of their control actions after fault clearance since no control action is effective during the current limitation which is activated during the faults.

The contributions of this chapter are as follows:

- Study two FVBs to improve transient stability of power systems with 100% of GFM-VSC-based generation, one based on local measurements and the other based on global measurements.
- Demonstrate significant improvements on the critical clearing times of different faults, due to the two control strategies proposed.
- Analyses the impact of communication latency on the performance of the proposed global control strategy. Results show that the proposed control strategy is robust for realistic communication latency.

The performance of the proposed strategies will be illustrated in Kundur's two-area test system [**Kundur'94**] with 100% of grid-forming VSC-based generation by means of electromagnetic-type simulation in Matlab + Simulink + SimPowerSystems.

4.4 Proposed fast voltage boosters to improve transient stability

In this section, fast voltage boosters for GFM-VSCs are proposed to improve transient stability. The proposed controllers are based on voltage/reactive-power control of the VSCs and they were inspired by the excitation boosters for synchronous machines proposed in [**Diez-Maroto'17**; **Díez-Maroto'19**a; **Díez-Maroto'20**] to improve transient stability in multi-machine systems. EBs in static-fed excitation systems in synchronous generators are based on supplying an additional field voltage when faults occur. Faults close to the generator's terminal can reduce the field voltage and, therefore, EBs need

to be implemented using external storage devices, such as ultra-capacitors or batteries [**Diez-Maroto'17**]. On the contrary, voltage boosters for GFM-VSCs manipulate the voltage set point and do not require additional devices, as will be explained in this section.

The active-power injection of the VSC at the connection point (see Figure 4.2) can be approximated as:

$$p_{g,i} \simeq \frac{v_{f,i} v_{g,i}}{x_{c,i}} \sin(\delta_{f,i} - \delta_{g,i}) \tag{4.1}$$

Eq. (4.1) is useful for qualitative analysis. Loss-of-synchronism in power systems with 100 % of GFM-VSC-based generation follows the same pattern as in multi-machine systems with synchronous generators. When a fault occurs, the voltage at the PCC, $v_{g,i}$, is diminished dramatically, reducing the active power injection $p_{g,i}$ (i.e. the virtual electromagnetic torque of the VSC). This produces the acceleration of the VSC frequency with respect to the nominal frequency ($\omega_{0,pu} = 1$ pu) according to the swing equation (4.2), which eventually sets the frequency imposed by the GFM-VSC:

$$p^0_{g,i} - p_{g,i} - D_{GFM,i}\Delta\omega_i = 2H_{GFM,i}\frac{d\Delta\omega_i}{dt} \tag{4.2}$$

Depending on the location of the fault, some VSCs will accelerate more than others and severe-enough faults could produce loss of synchronism of GFM-VSCs. For the purpose of this chapter, it should be noted that the VSM without PLL is considered for the control of the GFM-VSC (see Figure 4.1).

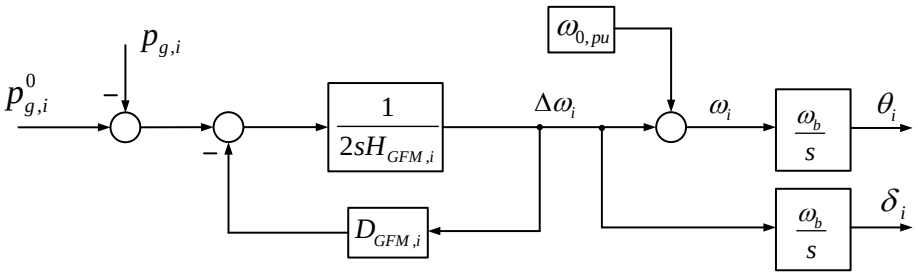

Figure 4.1: Supplementary controller of a virtual synchronous machine (VSM) implemented without PLL in a GFM-VSC.

Equation (4.1), shows that the active-power injection can be modified

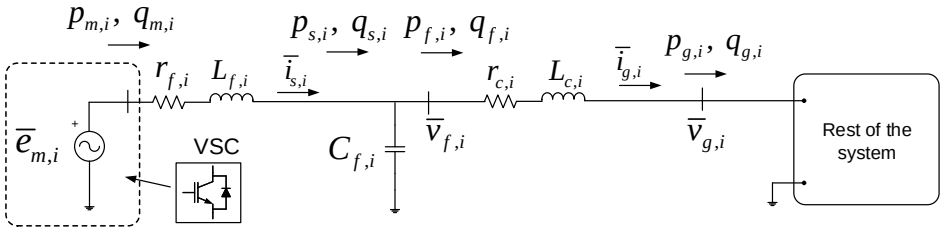

Figure 4.2: Equivalent model of a Grid-Forming Voltage Source Converter GFM-VSC.

by changing voltage $v_{f,i}$ and this is feasible, since voltage controllers of GFM-VSCs have fast responses. Therefore, the voltage set point of each GFM-VSC-i can be modified with an additional term ($\Delta v_{f,i}^{ref,TS}$) seeking the improvement of transient stability:

$$v_{f,i}^{ref} = v_{f,i}^{0} + \Delta v_{f,i}^{ref,TS} \tag{4.3}$$

where $v_{f,i}^{0}$ is the initial voltage set point. It should be noted that voltage set point $v_{f,i}^{ref}$ is actually the input of the voltage controller (2.8) (see Figure 2.7).

A control strategy will be effective to improve transient stability if it is able to act during the fault and/or inmediately after the fault clearing. In fact, VSCs might not be able to produce any effect during the fault, because the converter will limit its current injection, if the fault is close enough.

Transient stability of a single GFM-VSC connected to the grid can be improved by slowing down the frequency of the VSC with respect to the nominal frequency, following a pattern similar to the one used for a single synchronous machine connected to an infinite grid [**Kundur'94**; **Díez-Maroto'19**b]. Transient stability of a power system with 100 % GFM-VSC-based generation is a more complex phenomenon. A fault will produce that some VSCs accelerate faster than others during the transient, so control actions should try to pull their frequency together. In other words, some VSCs will have to be slowed down while others will have to be accelerated. This is, again, analogous to the case of a multi-machine system with conventional synchronous generators, where the use of the speed of the COI has proved to be useful [**Diez-Maroto'17**; **Díez-Maroto'19**a; **Díez-Maroto'20**].

The frequency of the COI in a power system with 100 % of GFM-VSC-

based generation can be defined as [**Choopani'20**]:

$$\omega_{COI} = \frac{1}{H_{tot}} \sum_{k=1}^{n} H_{GFM,k}\omega_k \text{ (pu) , with } H_{tot} = \sum_{k=1}^{n} H_{GFM,k} \tag{4.4}$$

Two control strategies are proposed in this Thesis:

- Local fast voltage booster (FVB-L, for short).
- Fast voltage booster using a wide-area control system (WACS) (FVB-WACS, for short).

4.4.1 Local fast voltage booster (FVB-L)

This control strategy was motivated by previous work on excitation boosters in synchronous machines [**Díez-Maroto'19**b] and on supplementary controllers for transient stability in shunt FACTS devices [**Haque'04**]. It consists in a fast voltage support. Strategy FVB-L uses local measurements as input signals: the voltage at the terminal of VSC-i, $v_{g,i}$, and the frequency deviation of each GFM-VSC-i, $\Delta\omega_i = \omega_i - \omega_{0,pu}$ (in pu) and its block diagram is shown in Figure 4.3.

The philosophy of local strategy FVB-L is as follows:

- Binary variable $\gamma_{1,i}$ is set to 1 if a voltage sag is detected with an hysteresis, as shown in Figure 4.3. If $v_{g,i} \leq v_{A,i}$, then $\gamma_{1,i} = 1$ and remains equal to 1 until $v_{g,i} > v_{B,i}$. if a fault is not detected, then $\gamma_{1,i} = 0$.
- Binary variable $\gamma_{2,i}$ is set to 1 if the frequency deviation of GFM-VSC-i (with respect to the nominal frequency) is greater than or equal to a certain threshold: $\Delta\omega_i \geq \omega_{thres,i}$. Otherwise, $\gamma_{2,i} = 0$.
- The supplementary controller is activated with binary variable γ_i, which is the result of a logic circuit with $\gamma_{1,i}$ and $\gamma_{2,i}$ as inputs, as shown in Figure 4.3.
- The supplementary voltage set point is given by: $\Delta v_{f,i}^{ref,TS} = \gamma_i \Delta v_{f,i}^{max}$, where $\Delta v_{f,i}^{max} > 0$ is a parameter of the controller ($\gamma_i = 0$ if the controller is deactivated and $\gamma_i = 1$ if the controller is activated).

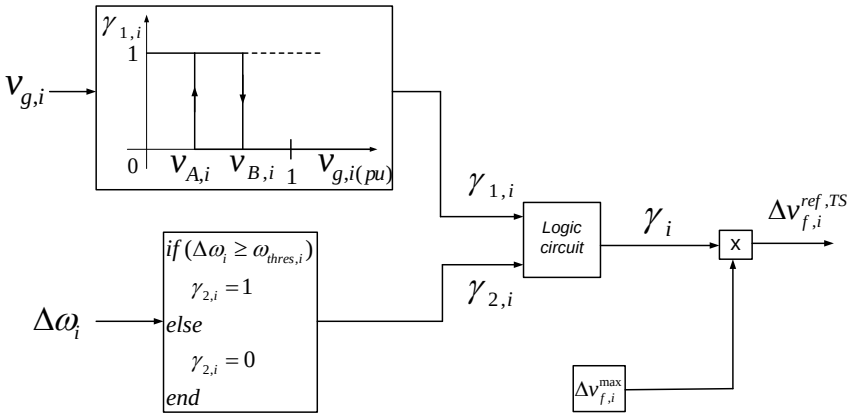

Figure 4.3: Strategy FVB-L.

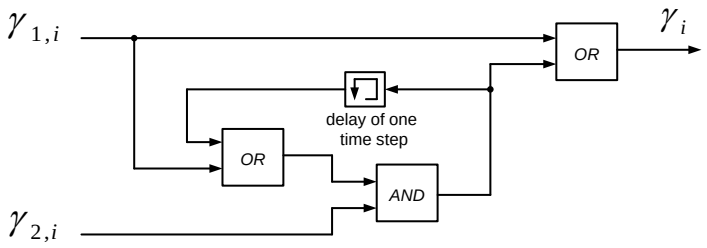

Figure 4.4: Strategy FVB-L. Logic circuit for fault detection.

The logic circuit rules for the activation of the controller can be summarised as follows:

- The controller will be activated if a voltage sag is detected. Therefore, $\gamma_{1,i}$ will drive the activation of the controller.
- Once the controller is activated, the supplementary voltage set point is maintained if at least one of the two following conditions are satisfied: undervoltage ($\gamma_{1,i} = 1$) or frequency greater than or equal to the threshold ($\gamma_{2,i} = 1$).

With this controller, VSC-i will increase its voltage setpoint with a positive increment $\Delta v_{f,i}^{ref,TS} = \Delta v_{f,i}^{max}$ if it detects a fault, trying to slow down the converter. This mechanism will improve transient stability of the grid-forming VSC connected to the rest of the system. The behaviour of each converter in a power system with several GFM-VSCs can be summarised as follows. When a fault occurs, the frequency of all GFM-VSCs will increase and all of them will see a certain voltage sag during the fault. The frequencies of GFM-VSCs close to the fault will grow faster than the frequencies of GFM-VSCs far from the fault. As discussed previously, the key point in transient stability is the difference between frequencies of the GFM-VSCs and not the absolute value of those frequencies. However, with this control strategy, converters do not have this information, because each VSC uses only local measurements. This problem can be tackled by the proper design of thresholds $v_{A,i}$, $v_{B,i}$ and $\omega_{thres,i}$ and with the logic circuit proposed of Figure 4.4. With the proper design of those thresholds, only controllers of GFM-VSCs close to the fault will be activated, and not the ones of VSCs far from the fault. Hence, transient stability in power systems with 100 % of GFM-VSC-based generation can be improved.

4.4.2 Fast voltage booster using a WACS (FVB-WACS)

This control strategy was motivated by previous work on excitation boosters in synchronous machines using the speed of the COI [**Diez-Maroto'17**; **Díez-Maroto'19**a; **Díez-Maroto'20**]. The proposed controller uses a fast voltage booster in each GFM-VSC using a wide-area control system (WACS). Following the scheme of Figure 4.5, where $K_{FVB,i}$ is a proportional gain, $T_{f,i}$ is a low-pass filter used for noise filtering, $T_{W,i}$ is a wash-out filter used to avoid any control actions in case of steady-state offsets and $\Delta v_{f,i}^{max}$ is a saturation parameter. The input of the controller is the error between a frequency set

point ($\omega_i^{ref,TS}$) and the frequency of each GFM-VSC (ω_i), in pu. A deadband of $\pm\epsilon_i$ is used to apply the control actions only when the system is subject to large-enough perturbations.

The frequency set point of each VSC-i is calculated as the frequency of the COI (Eq. (4.4)):

$$\omega_i^{ref,TS} = \omega_{COI} \tag{4.5}$$

Hence, a communication system is needed.

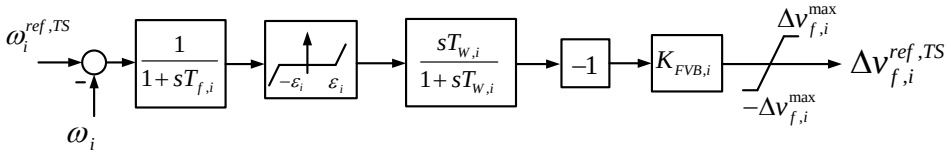

Figure 4.5: Strategy FVB-WACS.

The philosophy of FVB-WACS controller is as follows:

- If the frequency of VSC-i is above the frequency of the COI, VSC-i will increase its voltage setpoint, trying to slow VSC-i down.
- If the frequency of VSC-i is below the frequency of the COI, VSC-i will decrease its voltage setpoint, trying to accelerate VSC-i.
- Therefore, control actions will pull together the frequencies of GFM-VSCs of the system.

4.5 Results

The behaviour of Kundur's two-area test system [**Kundur'94**] with 100% of grid-forming VSC-based generation has been investigated (see Figure 4.6). Synchronous machines of the original system were replaced by GFM-VSC-based generators with VSM control, with the same rating as the original generators (900 MVA). The GFM-VSCs use current saturation algorithms (CSA) current limiters, which are conventionally used to protect the converter against damage.

Data of the system are provided in the Appendix. Converters have a current saturation algorithm with equal priority d-axis and q-axis currents, as indicated in Appendix A, in Table A.4. Simulations were carried out

with VSC_Lib tool, an open-source tool based on Matlab + Simulink + SimPowerSystems developed by L2EP-LILLE [**L2EP-LILLE'20**; **Qoria'18**a; **Qoria'19**]. Average electromagnetic-type models are used.

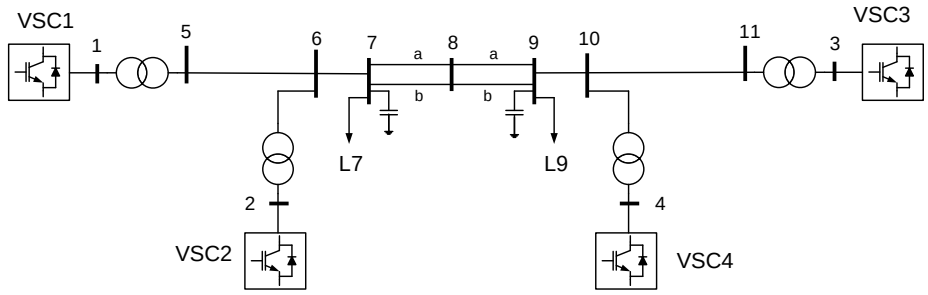

Figure 4.6: Kundur's two-area test system with 100% GFM-VSC-based generation.

Table 4.1 shows the results of the steady-state initial operating point.

Table 4.1: Initial operating point.

VSC	$v_{g,i}$ (pu)	$\delta_{g,i}$ (deg)	$P_{g,i}$ (MW)	$Q_{g,i}$ (MVAr)
VSC 1	1.0475	0.44	693.00	0.00
VSC 2	1.0309	0.45	693.00	90.00
VSC 3	0.9900	0.00	642.60	-69.93
VSC 4	0.9738	0.16	693.00	180.00

Three cases are compared:

- Base case: no supplementary controller for transient stability is implemented in the GFM-VSCs.
- FVB-L: VSCs applying FVB-L strategy (Figs. 4.3-4.4), with parameters: $v_{A,i} = 0.50$ pu, $v_{B,i} = 0.9$ pu, $\omega_{thres,i} = 10^{-3}$ pu, $\Delta v_{f,i}^{max} = 0.15$ pu.
- FVB-WACS: VSCs applying FVB-WACS strategy (Figure 4.5), with parameters: $K_{FVB,i} = 50$ pu, $T_{f,i} = 0.1$ s, $T_{W,i} = 10$ s, $\Delta v_{f,i}^{max} = 0.15$ pu and $\epsilon_i = 10^{-3}$ pu.

4.5.1 Simulation of Fault I

A three-phase-to-ground short circuit is applied to line 7-8a (close to bus 7), which is cleared by diconnecting the line 150 ms later (Fault I of Table 4.2). Figure 4.7 shows the angle difference between VSC-1 and VSC-3. In the base case, VSC-based generators lose synchronism. However, synchronism is maintained with the proposed supplementary controllers FVB-L and FVB-WACS (see Figure 4.7).

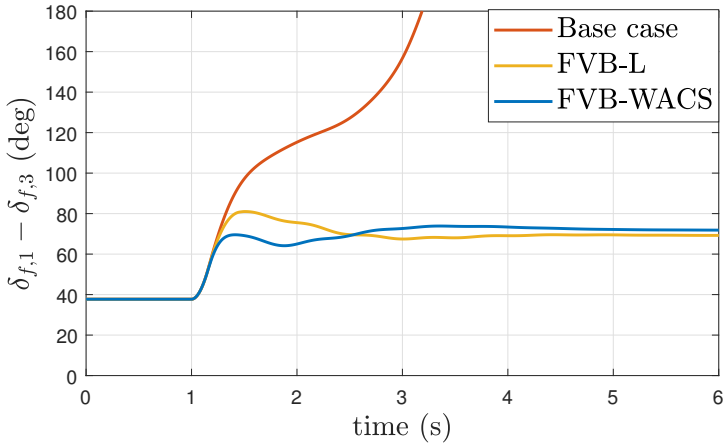

Figure 4.7: Fault I cleared after 150 ms. Angle difference of the VSCs.

Figure 4.8 shows the frequency deviations of the VSCs with respect to the frequency of the COI, while Figure 4.9 shows the supplementary voltage set point provided by the control strategies and the voltages of the VSCs. Notice that local strategy FVB-L is only activated in VSCs 1 and 2, which are close to the fault and not in VSCs 3 and 4, which are far from the fault. It is important to emphasise that achieving this configuration requires careful parameterisation of the controls, and this is by no means a straightforward task. This is why the FVB-L strategy is also effective in multi-converter systems with 100 % of grid-forming based generation; this is the consequence of the logic rules in Figure 4.4 and an appropriate design of the controller parameters. In control strategy FVB-WACS, a positive supplementary voltage set point is provided by VSCs 1 and 2 immediately after the fault clearing, because their frequencies are above the frequency of the COI (see Figure 4.8). Meanwhile, VSCs 3 and 4 provide a negative supplementary voltage during

the first swing, because their frequencies are below the frequency of the COI. Therefore, the frequencies of VSCs 1 and 2 will slow down while the frequencies of VSCs 3 and 4 will accelerate, reducing the risk of loss of synchronism.

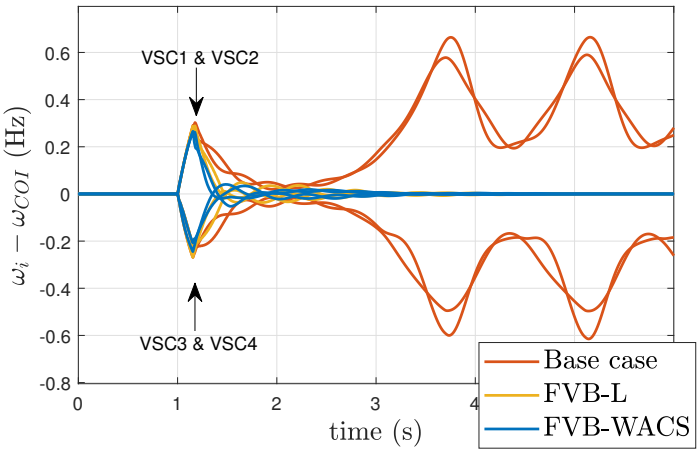

Figure 4.8: Fault I cleared after 150 ms. Frequency deviations of the VSCs with respect to the frequency of the COI.

Figure 4.10 shows the active-power injections of the VSCs. During the fault, the converter current limiter is activated leading to fast variations in the P injections. The active power injected by converters 1 and 2 decreases drastically during the fault. After the fault clearing, P injections are affected by the supplementary voltage set point of the proposed control strategies (FVB-L and FVB-WACS). By supplying a positive (negative) additional voltage set point $\Delta v_{f,i}^{ref,TS}$ (Figure 4.9), the active-power injection increases (decreases), according to (4.1). Precisely, (electrical) active-power injections, $p_{g,i}$, drive the slowing down or the acceleration of the GFM-VSCs, according to (4.2). For example, during the first swing, VSC-1 has its frequency above the frequency of the COI. Control strategy FVB-WACS increases its voltage set point. Hence, the active-power injection of VSC-1 is reduced, slowing down the converter. The opposite effect occurs in VSC-3: control strategy FVB-WACS accelerates VSC-3 during the first swing. As a result, VSC-1 and VSC-3 are pulled together.

Finally, Figure 4.11 displays the current injections of each VSCs. The converter current limiters, CSA, are activated during the fault in those con-

verters where the current limit is reached. The current injections of the VSCs 1 and 2, which are close to the fault, hit a peak reaching their maximum allowed value ($i_{s,i}^{max} = 1.25$). This results show that FVBs are compatible with current limiters of VSCs.

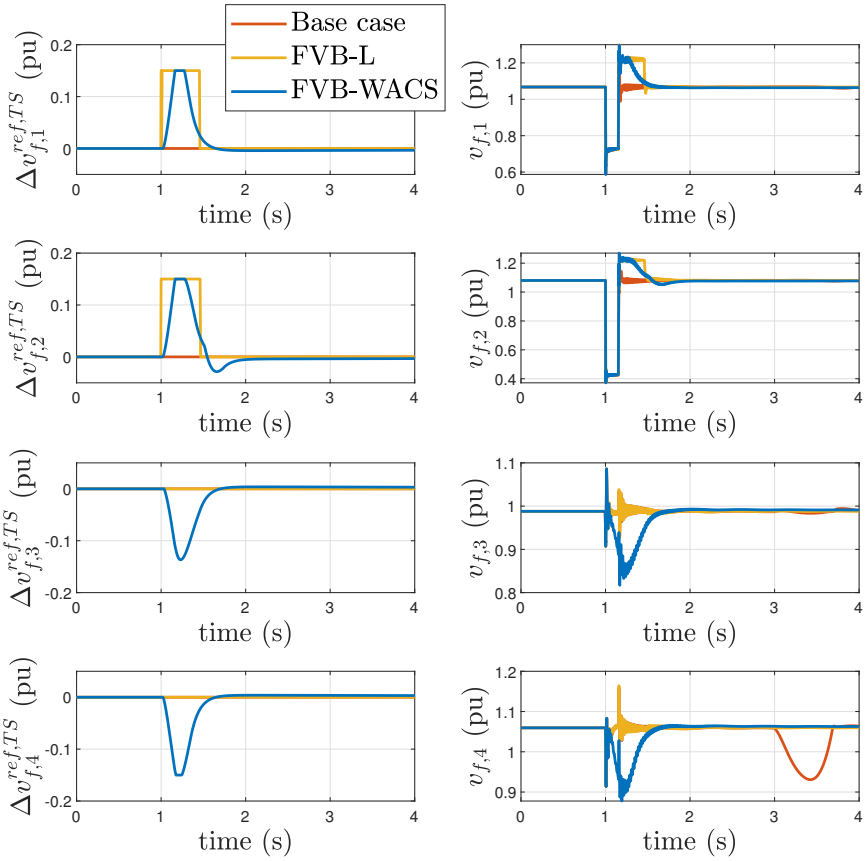

Figure 4.9: Fault I cleared after 150 ms. (left) Supplementary voltage set points of the VSCs and (right) voltages of the VSCs.

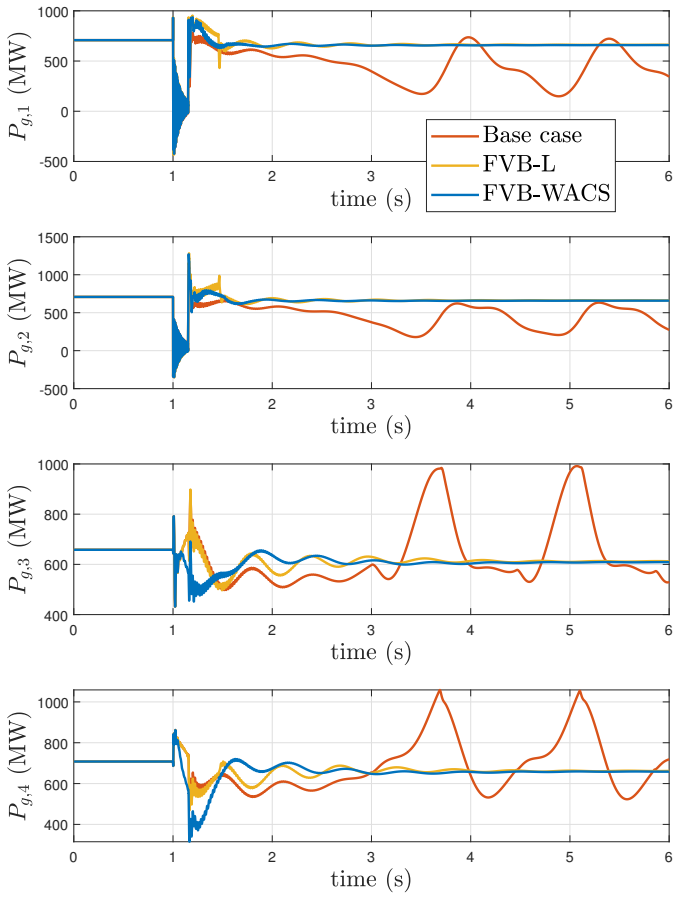

Figure 4.10: Fault I cleared after 150 ms. Active-power injections of the VSCs.

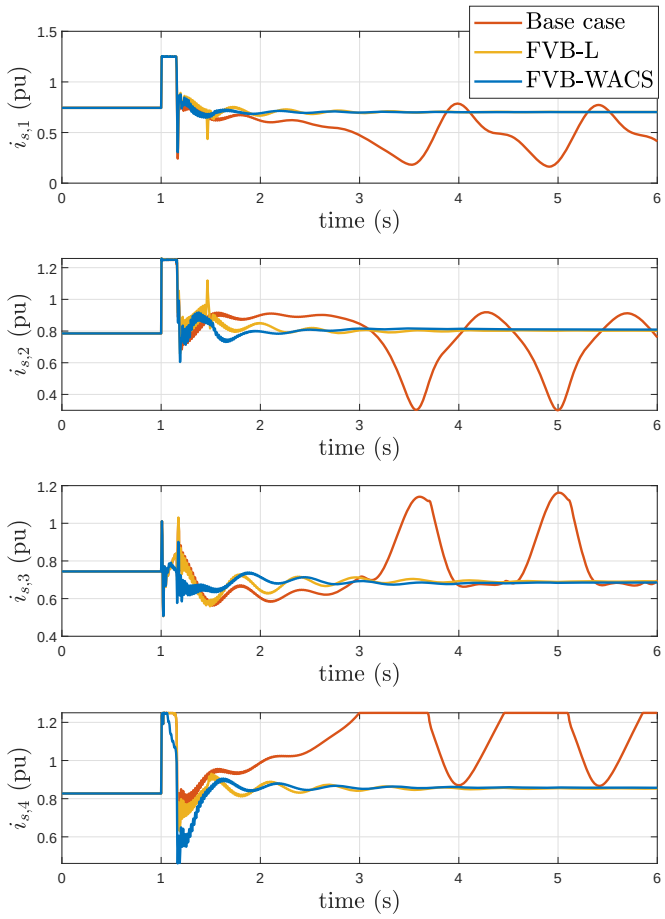

Figure 4.11: Fault I cleared after 150 ms. Current injections of the VSCs.

4.5.2 Critical clearing times (CCTs) and impact of communication latency

The critical clearing time (CCT) of different faults (described in Table 4.2) will be used to quantify transient-stability margins. Furthermore, the impact of communication latency on the performance of strategy FVB-WACS will also be analysed. Hence, the input error signal of the supplementary controller of Figure 4.5 will be delayed as:

$$u_i = e^{-s\tau}(\omega_{COI} - \omega_i) \tag{4.6}$$

where τ is the communication delay. The work in **[Zhang'15]** reported total communication delays in WACS within the range 50-80 ms. Total communication latency delays of 50 ms and 100 ms will be considered in this work.

Table 4.2: Fault description

	Short circuit at line $i-j$	close to bus	clearing
Fault I	7-8a	7	Disconnect 7-8a
Fault II	5-6	5	short circuit cleared (line not disconnected)
Fault III	10-11	11	short circuit cleared (line not disconnected)
Fault IV	8-9a	8	Disconnect 8-9a

CCTs of faults described in Table 4.2 are given in Table 4.3. The proposed supplementary controllers FVB-L and FVB-WACS increase the CCT of Fault I significantly. Strategy FVB-L also increases the CCT of Fault II, although the improvement is smaller than the one with strategy FVB-WACS. Furthermore, with strategy FVB-L, the CCT of Fault IV decreases from 420 ms of the base case to 400 ms. This is due to the conditions of activation of local strategy FVB-L described in Section 4.4.1. With a proper design of the activation thresholds, this strategy is only activated for severe-enough faults and this is why no negative impact is produced for any fault. An example of this is, if parameter $v_{A,i}$ of Figure 4.3 is changed from 0.75 pu to 0.5 pu, the CCT of Fault IV is not reduced (see Table 4.3). A value of $v_{A,i} = 0.5$ pu in FVB-L will be used in the rest of the chapter, which produced better results (these parameters are provided in the Appendix). While, there could be other faults (e.g. Fault III) in which the control strategies will have no impact. Overall, strategy FVB-WACS produces better results than FVB-L. Results of Table 4.3 also prove that strategy FVB-WACS is robust

against communication latency.

Table 4.3: Critical clearing times (CCTs).

CCT (ms)	**base case**	**FVB-L** $v_{A,i} = 0.75$ pu	**FVB-L** $v_{A,i} = 0.5$ pu	**FVB-WACS** $\tau = 0$ ms	with 50 ms	delay 100 ms
Fault I	130	250	250	270	270	260
Fault II	270	310	310	360	340	320
Fault III	220	220	220	230	230	230
Fault IV	420	400	420	880	870	890

4.5.3 Design and impact of the control parameters

This section analyses the design of and effect of the key parameters of strategies FVB-L and FVB-WACS. A key parameter of control strategy FVB-L (Figure 4.3) is the saturation parameter $\Delta v_{f,i}^{max}$. Key parameters of control strategy FVB-WACS (Figure 4.5) are the controller gain, $K_{FVB,i}$, and the saturation parameter $\Delta v_{f,i}^{max}$. The rest of parameters of strategies FVB-L and FVB-WACS are provided in the Appendix.

Table 4.4 shows the CCTs of the different faults of Table 4.2, for strategy FVB-L, using different values of $\Delta v_{f,i}^{max}$. In general, the higher $\Delta v_{f,i}^{max}$ is, the more effective the control strategy is. However, if $\Delta v_{f,i}^{max}$ is excessively high, the VSC could reach it limits (current or voltage limits) and these non-linearities will attenuate the effect of the control strategy (see Fault I with $\Delta v_{f,i}^{max} = 0.25$ pu, for example). In addition, $\Delta v_{f,i}^{max}$ must be consistent with the grid code. Parameter $\Delta v_{f,i}^{max}$ should always be designed considering the maximum AC voltage that can be produced by the GFM-VSC. Hence, the actual value of $\Delta v_{f,i}^{max}$ in the cases reported have been found equal to 0.15 pu by simulating extensively the test case.

Table 4.4: Strategy FVB-L. Impact of parameter $\Delta v_{f,i}^{max}$. Critical clearing times (CCTs).

CCT (ms)	**base case**	**FVB-L** $\Delta v_{f,i}^{max} = 0.05$ pu	**FVB-L** $\Delta v_{f,i}^{max} = 0.15$ pu	**FVB-L** $\Delta v_{f,i}^{max} = 0.25$ pu
Fault I	130	200	250	240
Fault II	270	290	310	290
Fault III	220	210	220	220
Fault IV	420	420	420	420

Tables 4.5 and 4.6 show the CCTs of the different faults of Table 4.2,

with strategy FVB-WACS, using different values of $K_{FVB,i}$ and $\Delta v_{f,i}^{max}$, respectively.

In general, the higher the gain $K_{FVB,i}$ is, the more effective the control strategy is. Nevertheless, if $K_{FVB,i}$ is excessively high, could jeopardise the stability or the VSC could reach its limits (current or voltage limits) and these non-linearities will attenuate the effect of the control strategy. The optimal value of $K_{FVB,i}$ must be investigated calculating CCTs by simulation. Table 4.5 shows that $K_{FVB,i} = 50$ pu is a reasonable value for the case study presented here. Saturation parameter ($\Delta v_{f,i}^{max}$) in FVB-WACS produces an effect similar to the one in FVB-L: it must be consistent with the over-voltage allowed by the grid code and its value must be limited not to push converters to their limits in the post-fault time. Again a value of 0.15 pu was found reasonable in the case study presented.

Finally, it is very important to highlight that saturation parameter, $\Delta v_{f,i}^{max}$, in strategies FVB-L and FVB-WACS must be always compatible with Fault Ride Through (FRT) requirements of the TSO.

Table 4.5: Strategy FVB-WACS. Impact of parameter $K_{FVB,i}$. Critical clearing times (CCTs).

CCT (ms)	**base case**	**FVB-WACS**		
		$K_{FVB,i} = 25$ pu	$K_{FVB,i} = 50$ pu	$K_{FVB,i} = 75$ pu
Fault I	130	240	250	260
Fault II	270	340	310	370
Fault III	220	230	220	230
Fault IV	420	660	880	940

Table 4.6: Strategy FVB-WACS. Impact of parameter $\Delta v_{f,i}^{max}$. Critical clearing times (CCTs).

CCT (ms)	**base case**	**FVB-WACS**		
		$\Delta v_{f,i}^{max} = 0.05$ pu	$\Delta v_{f,i}^{max} = 0.15$ pu	$\Delta v_{f,i}^{max} = 0.25$ pu
Fault I	130	200	270	300
Fault II	270	320	360	380
Fault III	220	230	230	230
Fault IV	420	600	880	880

4.5.4 Discussion on the use of local and global measurements

This section discusses two key factors of the proposed control strategies: implementation and effectiveness. In strategy FVB-L, each GFM-VSC uses

only local measurements, whereas in strategy FVB-WACS, global measurements are used and, therefore, a communication system is needed. Clearly, the implementation of local strategy FVB-L is easier and cheaper. The ideal control actions are supplying a positive (negative) supplementary voltage in those VSCs with frequency above (below) the frequency of the COI. Although strategy FVB-WACS produces better results than strategy FVB-L, precisely because it uses global measurements (the frequency of the COI). The activation thresholds of the local strategy FVB-L (described in Section 4.4.1) can be tuned in order to ensure that the control strategy is activated only for faults that are close enough, which are, in fact, the ones that produce frequencies above the frequency of the COI. As a general recommendation, local strategy FVB-L can be implemented in grid-forming VSCs to improve transient stability for severe faults. Nevertheless, the use of strategy FVB-WACS could be an interesting option in power systems which are vulnerable to transient stability, since the latter can produce more significant improvements.

4.6 Conclusions

Conclusions obtained in this chapter can be summarised as follows:

- The proposed local strategy FVB-L improves transient stability of severe faults, significantly, and their critical clearing times (CCTs) are increased. However, its control actions must be restricted to severe-enough faults by proper tuning activation thresholds. This means that this control strategy will have little effect on transient stability when remote faults occur.

- The proposed global strategy FVB-WACS improves transient stability, significantly, improving their CCTs. It produces significant improvements for severe and non-severe faults. The control strategy is robust when subject to communication latency.

- FVB-L strategy uses local measurements. Hence, its implementation is easier and cheaper. Meanwhile, FVB-WACS requires a communication system to use global measurements, having, therefore, a more difficult and expensive implementation. A trade-off should be made when choosing using FVB-L or FVB-WACS. In general, the implementation of FVB-L improving transient stability only for faults close to the GFM-VSC could be a cost-effective and practical solution. Nevertheless, in power systems which are vulnerable to transient stability,

FVB-WACS could be a more effective solution, improving transient stability of severe and non-severe faults.

- The effect of control parameters of strategies FVB-L and FVB-WACS has been analysed to provide design guidelines tuning the parameter values by simulation. High values of $\Delta v_{f,i}^{max}$ and $K_{FVB,i}$ can improve the effectiveness of the control strategy, but setting them too high can jeopardise the stability or cause the GFM-VSC to reach its limits, leading to non-linearities that can reduce the effect of the control strategy.

Chapter 5

Impact of current limiters on the performance of fast voltage boosters for transient stability improvement

5.1 Introduction

This chapter studies the impact of HCLs [**Qoria'20**a] and FVBs [**Ávila-Martínez'22**] on transient stability in power systems with 100 % non-synchronous generation. The chapter provides a review of previous work related to current limiter strategies, including the current saturation algorithm (CSA) and current limitation based on virtual impedance (VI-CL) [**Paquette'15**; **Qoria'20**a]. The HCLs, which are the combination of the CSA and current limiter based on VI, improve the performance of the power system, while the FVB provides a fast response to voltage drops during faults. The chapter presents the results from short circuit simulations and critical clearing time analysis to evaluate the effectiveness of the HCLs and FVBs in improving the transient stability of power systems. The effectiveness of these approaches in mitigating overcurrent and overvoltage problems is demonstrated by the simulation results.

The rest of the chapter is organised as follows: Section 5.2 provides a review of previous work related to current limiter control strategies applied to GFM-VSCs for transient stability improvement; Section 5.3 describes the gap covered by the chapter; Section 5.4 describes different current limiter

methods, including the current saturation algorithm (CSA) and the current limiters based on virtual impedance (VI-CL); This Section also presents the HCLs proposed in [**Qoria'20**b]; Section 5.5 presents the results and discussion of short circuit simulations and critical clearing time analysis. The impact of communication latency on the effectiveness of the implemented strategies is also discussed in this section; Finally, Section 5.6 provides the conclusions drawn from the chapter.

5.2 Review of previous work

Chapter 4 and the preceding text contain various research studies that explore ways to improve transient stability in power systems using GFM-VSCs. Another approach is to implement current limiters, as discussed in [**Qoria'20**b; **Qoria'20**a; **Rokrok'21**], which can limit the current magnitude, fault current contribution, and facilitate fault recovery. When a fault occurs, GF-VSCs are bound to reach their current limit. The work in [**Qoria'20**b] analyses the impact of current-limiting strategies on transient stability of a GFM-VSC connected to an infinite grid. The study analyses two current-limiting strategies: current-modulus limiter in vector control (Current Saturation Algorithm, CSA) and virtual-impedance-based current limiter (VI-CL). Eventually, the work proposes a combination of both strategies, improving the performance of the current limitation process as well as transient stability. Reference [**Rokrok'21**] also analyses the effect of converter current limitation on transient stability. The case study consists on a GFM-VSC connected to an infinite bus and the study focuses on the effect of the angle of the resulting current phasor which, together with the saturated current modulus, determines the active power delivered by the converter. In [**Fan'22**a], a literature review of existing research on current limiting control methods for GFM-VSCs under severe symmetrical disturbances is presented. The paper discusses the challenges of each method and their effectiveness in limiting current magnitude, fault current contribution, and fault recovery during the disturbance ride-through process. Among these methods, current limiters can meet the fault current contribution requirement by adjusting current or power references, but may fail to recover from severe disturbances. In comparison, the virtual impedance methods and voltage limiters can provide better fault recovery capability but may have limitations in achieving accurate output voltage regulation.

In [**Kanakesh'21**], the behavior of GFM-VSCs in response to large fre-

quency changes, phase jumps, and voltage faults is examined, especially when these converters are forced into current limit operation. The paper offers a quantitative and illustrative analysis of the effects of current limit operation and proposes a method to improve transient stability using virtual unsaturated power as feedback or controlled parameters for power synchronisation. The work in [**Sadeghkhani'17**], proposes a strategy to enhance the fault ride-through capability of inverter-based islanded microgrids by limiting the output current and voltage. The study evaluates the effectiveness of two main current limiting strategies, namely the instantaneous saturation limit and latched limit, during various fault conditions, including asymmetrical and symmetrical faults. By limiting the output current during a fault, these strategies prevent overloading and damage to the system, ensuring the stable operation of distributed energy resources. The study in [**Paquette'15**], focuses on current limiting for voltage-controlled inverters during overloads caused by poor transient load sharing between inverters and synchronous generators in islanded microgrids. The paper proposes the use of virtual impedance for current limiting to improve transient stability during current limiting when operating in parallel with synchronous generators. The experimental results show that virtual impedance current limiting effectively improves transient stability during current limiting in islanded microgrids.

In [**Qoria'22**], an analysis of the variable virtual impedance (VI) method for overcurrent protection in GFM-VSCs is presented. The authors propose improvements to the VI method to enhance its effectiveness in limiting overcurrents during large grid disturbances. The results show that the improved VI method provides better protection against overcurrents during large grid disturbances. The research in [**Fan'22**b], analyses the post-fault behavior of GFM-VSCs. The study identifies three post-fault scenarios: normal operation, current limitation, and oscillations. The impact of the current-limiting control parameters and short-circuit ratio on the fault recovery process is also revealed. The paper concludes by discussing potential solutions for improving the fault recovery capabilities of GFM inverters with current-limiting controls.

This study focuses on researching the impact of hybrid current limiters (HCLs) [**Qoria'20**a] and fast voltage boosters (FVBs) [**Ávila-Martínez'22**] on transient stability in power systems with 100% grid-forming VSC-based generators. The HCLs, which combine the CSA (Current Saturation Algorithm) and a current limiter based on virtual impedance (VI), enhance the overall performance of the power system. Additionally, the FVBs provide a rapid response to voltage drops that occur during faults. Both methods

contribute significantly to improving the transient stability of these types of systems. To assess the effectiveness of HCLs and FVBs in enhancing transient stability, short-circuit simulations and critical clearing time analysis are conducted. The simulation results demonstrate the efficacy of these approaches in preventing the loss of synchronism.

5.3 Gap covered by this chapter

Previous work has shown that specific strategies can be implemented in GFM-VSCs to improve transient stability. These strategies include voltage/reactive-power control and current-limitation approaches. Two voltage/reactive-power control strategies, called FVBs, have been proposed in Chapter 4 of this thesis and reported in [**Ávila-Martínez'22**]. Additionally, new variants of current limiters, such as the hybrid current limiter (HCL) that combines the current saturation algorithm (CSA) with a current limiter based on virtual impedance (VI-CL), can be used to improve transient stability.

This chapter addresses whether combining the voltage/reactive-power control strategies and current limiters in GFM-VSCs would still be effective in improving transient stability. The contributions of this chapter are to investigate the effectiveness of these combined strategies and to provide insights into their implementation. Therefore, the main contributions of this chapter are as follows:

- Investigation of the impact of the hybrid current limiters and fast voltage boosters on trasient stability of power systems with 100% of GFM-VSC-based generation.
- Demonstration of the effectiveness of both approaches in significantly improving the critical clearing times of different faults.
- Analysis of the impact of communication latency on the global control strategy (FVB-WACS) performance with hybrid current limiters. The results indicate that the combined use of these strategies remains robust even in the presence of communication latency.

In summary, this research examines the effects of hybrid current limiters and fast voltage boosters on transient stability in power systems, demonstrating their ability to improve critical clearing times and mitigate the effects of communication latency.

.

5.4 Current limiters (CL)

This section briefly reviews the current limits of grid-forming control of power converters. Some events in power systems may produce overcurrent in the power electronic converters. Power converters can provide a small overload current compared to synchronous machines. In particular, each component of the three-phase current injections $i_{s,i}$ needs to be limited to avoid damaging the semiconductor switches. Different alternatives exist for the implementation of current limitations in grid-forming converters. This study focuses on three general approaches to implementing current limits for grid forming control on transient stability: (a) current saturation algorithm (CSA) [**Qoria'20**c], (b) current limitation based on virtual impedance (VI) [**Qoria'20**a; **Qoria'20**c] and (c) hybrid current limiter (HCL) which consists in hybridising the former, CSA with the latter, VI [**Qoria'20**b].

5.4.1 Current saturation algorithm (CSA)

The current set points ($i_{s,d,i}^{ref'}$ and $i_{s,q,i}^{ref'}$) of Figure 2.7 are the outputs of the outer control loop:

$$\bar{i}_{s,i}^{ref'} = i_{s,d,i}^{ref'} + j i_{s,q,i}^{ref'} = i_{s,i}^{ref'} e^{j\delta_{is,i}^{ref'}} \tag{5.1}$$

The magnitude of the current set point, $i_{s,i}^{ref'}$, must be lower than or equal to the maximum current of VSC-i: $i_{s,i}^{max}$, as illustrated in Figure 5.1. Typical values of the maximum current are $i_{s,i}^{max} = 1-1.25$ pu. The current limitation algorithm obtains the saturated current set-point values ($i_{s,d,i}^{ref}$ and$i_{s,q,i}^{ref}$), as follows:

$$i_{s,d,i}^{ref} = \begin{cases} i_{s,i}^{max}\cos(\delta_{is,i}^{ref}) & if \quad i_{s,i}^{ref'} > i_{s,i}^{max} \\ i_{s,d,i}^{ref} = i_{s,d,i}^{ref'} & if \quad i_{s,i}^{ref'} \leq i_{s,i}^{max} \end{cases} \tag{5.2}$$

$$i_{s,q,i}^{ref} = \begin{cases} i_{s,i}^{max}\sin(\delta_{is,i}^{ref}) & if \quad i_{s,i}^{ref'} > i_{s,i}^{max} \\ i_{s,q,i}^{ref} = i_{s,q,i}^{ref'} & if \quad i_{s,i}^{ref'} \leq i_{s,i}^{max} \end{cases} \tag{5.3}$$

CSA algorithm could use different priority for d-axis and q-axis currents,

although in this work equal priority for both will be used. Hence, the angle of the reference current does not change ($\delta_{is,i}^{ref} = \delta_{is,i}^{ref'}$).

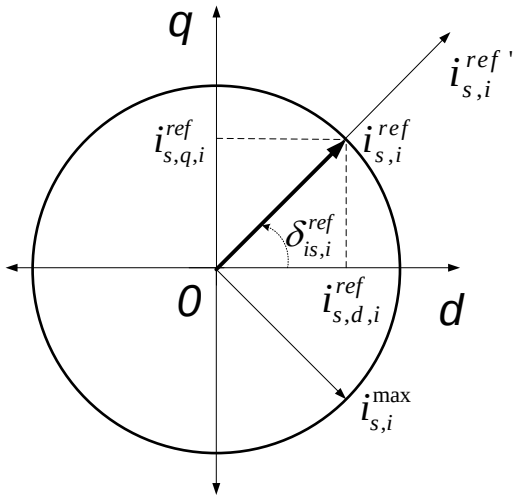

Figure 5.1: Current saturation algorithm (CSA).

Once the current set-point values are saturated, the inner loop of the grid-forming VSC-i controls the current injections $i_{s,d,i}$ and $i_{s,q,i}$ with proportional-integral (PI) controllers and they will provide the set-point values of the output voltage of the VSC: $e_{m,d,i}$ and $e_{m,q,i}$ (see Figure 2.7).

5.4.2 Current limitation based on virtual impedance (VI-CL)

A transient virtual impedance is added to provide current limitation and improve transient stability [**Qoria'20**a]. This consists of adding the terms $-\Delta v_{f,d,i}^{ref',VI}$ and $-\Delta v_{f,q,i}^{ref'VI}$ to the voltage set points of the outer controllers of Eq. (2.8) described in Chapter 2:

$$\begin{aligned} v_{f,d,i}^{ref} &= v_{f,i}^{ref} + \Delta v_{f,d,i}^{ref,VR} - \Delta v_{f,d,i}^{ref',VI} \\ v_{f,q,i}^{ref} &= 0 + \Delta v_{f,q,i}^{ref,VR} - \Delta v_{f,q,i}^{ref'VI} \end{aligned} \tag{5.4}$$

Terms $\Delta v_{f,d,i}^{ref',VI}$ and $\Delta v_{f,q,i}^{ref'VI}$ of the Eq. (5.4) are calculate as follows:

$$\begin{aligned} \Delta v_{f,d,i}^{ref',VI} &= r_{VI} i_{s,d,i} - x_{VI} i_{s,q,i} \\ \Delta v_{f,q,i}^{ref',VI} &= r_{VI} i_{s,q,i} + x_{VI} i_{s,d,i} \end{aligned} \tag{5.5}$$

Expression (5.5) only affects the transient and not the steady-state. The virtual impedance algorithm is activated only when the converter current magnitude $i_{s,i}$ exceeds the maximum value of VI ($i_{s,i} > i_{VI,i}^{max}$ pu). Otherwise, VI will be disabled. x_{VI} and r_{VI} are given in (5.6) and (5.7).

$$x_{VI} = \begin{cases} k_{p_{r_{VI}}} \sigma_{x/r} \Delta i_{s,i} & if \quad i_{s,i} > i_{VI,i}^{max} \\ \\ 0 & if \quad i_{s,i} \leq i_{VI,i}^{max} \end{cases} \tag{5.6}$$

$$r_{VI} = r_{VI} / \sigma_{x/r} \tag{5.7}$$

where $i_{s,i} = \sqrt{(i_{s,d,i})^2 + (i_{s,q,i})^2}$ and the parameters $k_{p_{r_{VI}}}$ and $\sigma_{x/r}$, are respectively the proportional gain and the ratio of the virtual impedance, defined in [**Qoria'20**a]. $k_{p_{R_{VI}}}$ is set to limit the current magnitude to a suitable level $i_{VI,i}^{max}$ during overcurrent in the steady state, while $\sigma_{X/R}$ ensures a good system dynamics during the overcurrent.

5.4.3 Hybrid current limiter (HCL)

The current saturation algorithm and current limitation based on virtual impedance can be implemented independently, both algorithms can also be hybridised simultaneously to benefit each other, as explained in [**Qoria'20**b]. CSA provides better post-fault current limitation than VI. In contrast, VI is better than CSA during the transient stability after the fault clearance. In comparison with the CSA, VI is less effective, because the VI cannot see the overcurrent peak reached by the convert just after the fault occurs. Therefore, hybridising both current limiting algorithms simultaneously takes advantage of their benefits, having an accurate current limitation for transient stability improvement.

To operate with hybrid current limiters, it is necessary to avoid activating both forms of current limitation, CSA and VI, simultaneously. This aim is achieved by making the maximum current allowed by CSA always higher

than the maximum value allowed by VI. For example, if the maximum CSA value is $i_{s,i}^{max} = 1.25$ pu, the maximum VI value should not be higher than 1.25 pu, then a reasonable value could be $i_{VI,i}^{max} = 1 - 1.2$ pu.

Hybridising both current limiters strategies activates the VI in case of a fault ($i_{s,i} > i_{VI,i}^{max}$). The CSA is activated if the current magnitude exceeds the maximum CSA value ($i_{s,i} > i_{s,i}^{max}$); otherwise, the CSA remains disabled. The CSA activation limits the VSC current injection at $i_{s,i}^{max}$ for a few milliseconds until the VI action diminishes the current to a lower value than the CSA limit ($i_{s,i} < i_{s,i}^{max}$). When the condition $i_{VI,i}^{max} < i_{s,i} < i_{s,i}^{max}$ is fulfilled, VI ensures the current limitation for the rest of the fault duration, improving the transient stability.

5.5 Results

Simulations were carried out to analyse the impact of FVBs and HCLs on Kundur's two-area test system [**Kundur'94**] with 100% grid-forming VSC-based generation. The system data and the corresponding one-line diagram of the study system can be found in Appendix A, specifically in Table A.4 and Figure A.3.

The following cases have been analysed and compared:

- Base case: current limiter only (CSA or HCL).
- FVB-L (local) and current limiter (CSA or HCL).
- FVB-WACS (global) and current limiter (CSA or HCL).

5.5.1 Simulation of Fault 1

A three-phase-to-ground short circuit is applied to line 7-8a (close to bus 7) of the test system in Figure A.3, which is cleared by disconnecting the line after 140 ms (Fault I of Table A.3). Figure 5.2 shows the angle difference between VSC-1 and VSC-3 for the six cases analysed while Figure 5.3 shows the frequency deviations of the VSCs with respect to the frequency of the COI. In the base case with CSA and no FVBs, GFM-VSC lose synchronism. The system maintains synchronism for the rest of the cases (see Figure 5.2). Although, synchronism between GFM-VSCs is maintained in the base case with HCL and no FVBs, the angles and frequencies of the GFM-VSCs present higher separations during the transient. Note that angle

differences are similar when using FVB-WACS with CSA or HCL, whereas some differences are observed in case of FVB-L with CSA or HCL.

Figure 5.4 shows the supplementary voltage set point (provided by FVBs strategies) and the output voltages of each VSC. The FVB-L strategy provides a positive supplementary voltage setpoint in all converters that detect the fault. Only the converters close to the fault (VSCs 1 and 2) activate the FVB-L strategy but not those far from it (VSCs 3 and 4). This behaviour is due to the logic rules of Figure 4.4 and an appropriate design of the FVB-L controller parameters. Therefore, this strategy is very effective whether implemented with CSA or HCL current limiters. Strategy FVB-WACS can provide a positive or/and negative supplementary voltage setpoint during the first swing. This action depends on whether the converter frequencies are above or below the frequency of the COI (see Figure 5.3). Thus, GFM-VSCs 1 and 2 provide a positive supplementary voltage setpoint $\Delta v_{f,i}^{ref,TS}$, slowing down the GFM-VSCs. While GFM-VSCs 3 and 4 provide a negative $\Delta v_{f,i}^{ref,TS}$, they accelerate as is shown in Figure 5.4 (blue and purple), reducing the risk of loss of synchronism. FVB-WACS strategy is also effective when using CSA or HCL current limiters.

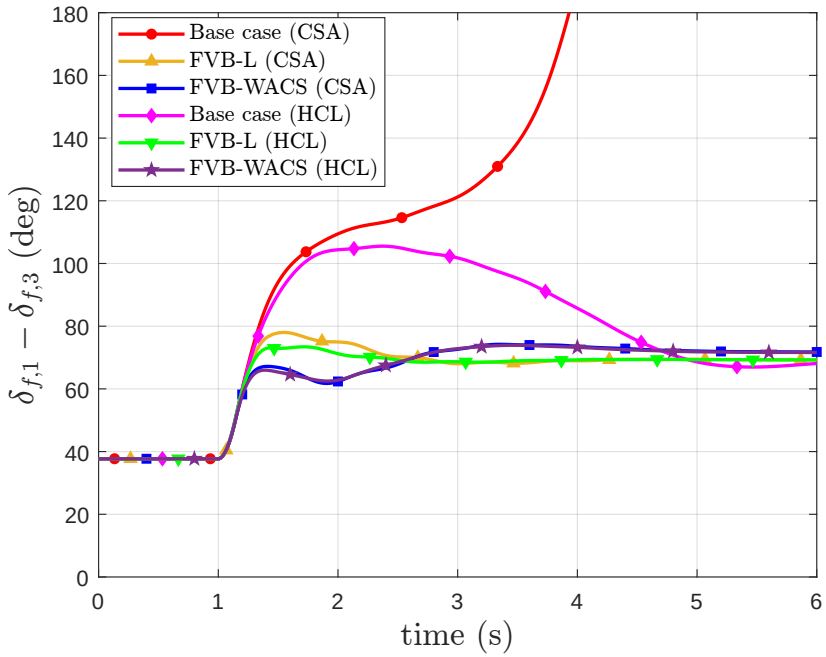

Figure 5.2: Fault I cleared after 140 ms. Angle difference of the VSCs.

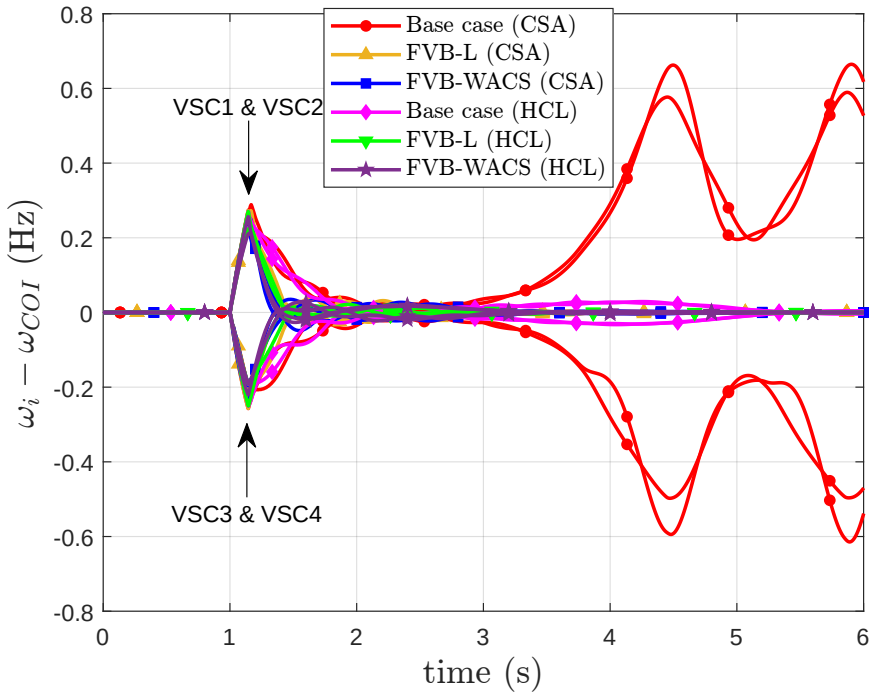

Figure 5.3: Fault I cleared after 140 ms. Frequency deviations of the VSCs with respect to the frequency of the COI.

Figure 5.5 shows the active power injections of the GFM-VSCs and Figure 5.6 their current injections. The fault activates the current limiters (either CSA or HCL) in those converters closer to it, leading to fast variations in the active-power injections until the fault clearance. After the fault is cleared, converters supply a positive or negative additional voltage setpoint $\Delta v_{f,i}^{ref,TS}$, by the action of FVB controllers (FVB-L and FVB-WACS). The supplementary voltage set points increase or decrease the active powers injections of the converters according to (4.1). Precisely, (electrical) active-power injections, $p_{g,i}$, drive the slowing down or the acceleration of the GFM-VSCs, according to (3.1).

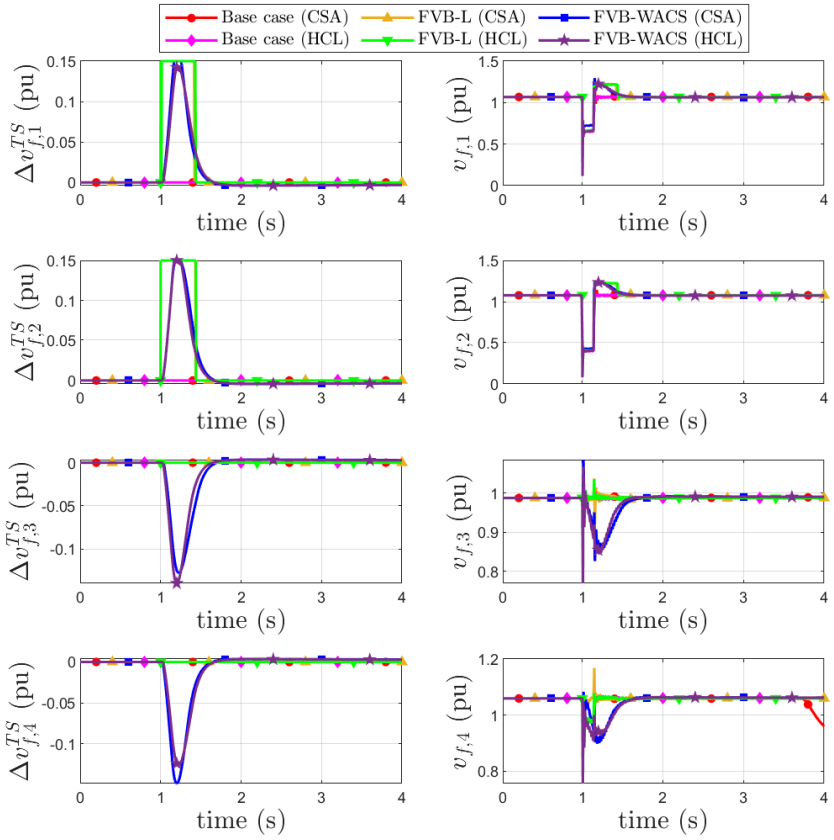

Figure 5.4: Fault I cleared after 140 ms. (left) Supplementary voltage set points of the VSCs and (right) voltages of the VSCs.

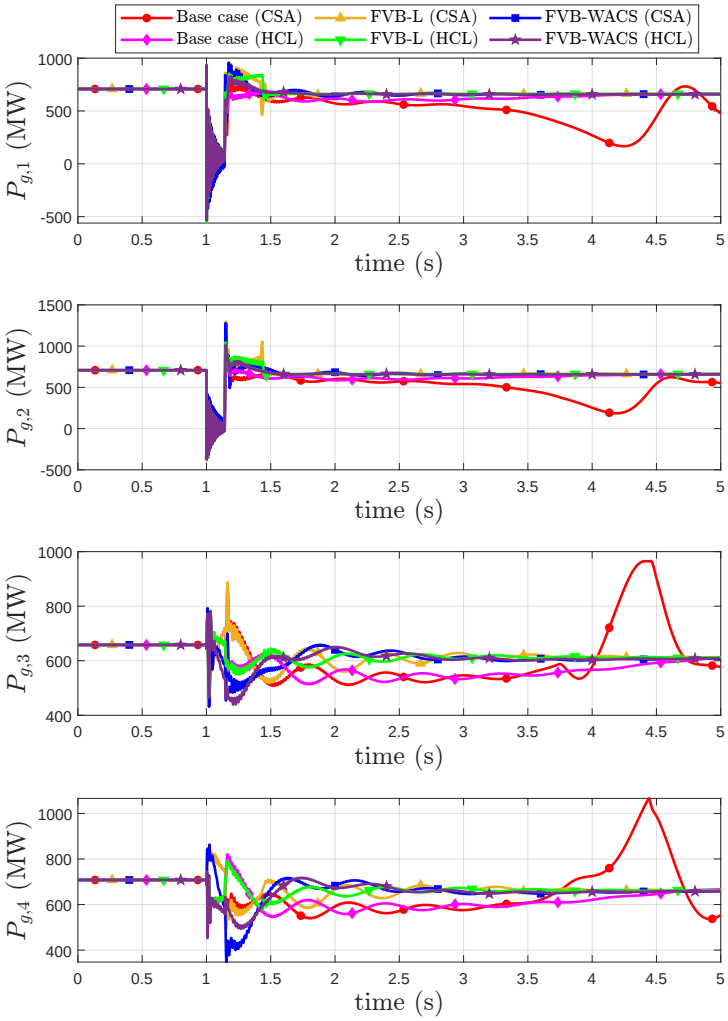

Figure 5.5: Fault I cleared after 140 ms. Active-power injections of the VSCs.

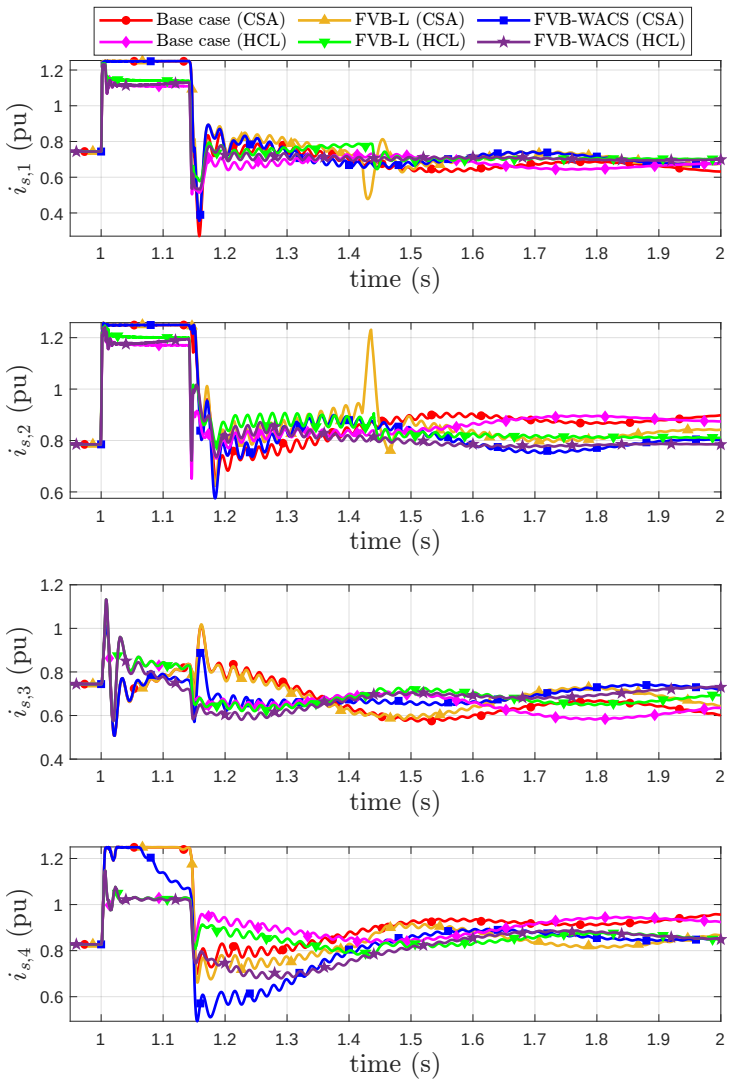

Figure 5.6: Fault I cleared after 140 ms. Current injections of the VSCs.

Current limiters CSA are activated just after the fault occurs in GFM-VSCs 1, 2, and 3, where the current limit is reached ($i_{s,i}^{max} = 1.25$). The current injections of those converters closer to the fault peak, reaching their maximum allowed value according to (5.2) and (5.3) (see Figure 5.1). In the cases where the CSA is used alone (without FVBs), converters remain at the maximum limit value allowed by CSA until the fault clearance. Meanwhile, when HCLs are used, the current injections of GFM-VSCs initially reach the CSA limit, and then they are reduced by the virtual-impedance action, impeding the loss of synchronism and thus improving transient stability.

The effectiveness of FVBs when using HCLs is due to the fact that actions of both controllers take place at different stages of the transient. During the fault, the HCL has priority and it introduces a supplementary voltage set point to the GFM-VSC. Once the fault has been cleared, the HCL is disabled and the FVB introduces a supplementary voltage set point to the GFM-VSC. Therefore, the use of FVBs together with HCLs takes advantage of both.

5.5.2 Critical clearing times (CCTs)

Tables 5.1 and 5.2 show the critical clearing times (CCTs) of the faults described in Table A.3 (see Appendix A) with/without FVBs, using CSA or HCL current limiters. The FVB-WACS strategy increases the CCTs of all faults. In contrast, the FVB-L strategy significantly increases the CCTs only on faults I and II, with no impact on faults III and IV. This behaviour is because the FVB-L strategy is designed to be activated only for severe-enough faults as a consequence of the activation conditions of the local strategy FVB-L described in in Chapter 4. Comparing Tables 5.2 and 5.1, results shows that HCL with no FVBs significantly improves the CCTs of faults III and IV with respect to CSA with no FVBs. However, the improvements for faults I and II are very small. This confirms that HCL is more effective than CSA .

The use of HCL algorithms with FVB strategies improves the CCTs in all faults, even in those where the FVBs and the HCLs cannot improve when applied independently. The best results are obtained when implementing FVB-WACS with HCL current limiter. For example, the Base case without FVB and using HCL does not have significant improvements in faults I and II. Nevertheless, by combining HCLs with the FVBs (local or global measurements), improvements in transient stability are produced. In the same way, this situation happens in those faults where the FVBs strategies had no relevant impact, such as fault number III. Specifically, using the FVB-WACS strategy with HCLs improves 100 ms concerning both "base case using HCL"

and "FVB-L strategy using HCL". Therefore, this improvement is more significant concerning the original base case (480 ms) than the FVB-WACS strategy no using HCL cunrrent limiter, which only improves 10 ms to the original base case.

Table 5.1: Critical clearing times (CCTs) with CSA.

CCT (ms)	**Base case**	**FVB-L**	**FVB-WACS** $\tau = 0$ ms	with 50 ms	delay 100 ms
Fault I	130	250	270	270	260
Fault II	270	310	360	340	320
Fault III	220	220	230	230	230
Fault IV	420	420	880	870	890

Table 5.2: CCTs with HCL

CCT (ms)	**Base case (HCL)**	**FVB-L (HCL)**	**FVB-WACS (HCL)** $\tau = 0$ ms	with 50 ms	delay 100 ms
Fault I	140	280	290	290	280
Fault II	280	330	370	370	360
Fault III	600	600	700	700	690
Fault IV	510	510	930	950	940

5.5.3 Impact of the CSA current limiter of the VSCs

The effect of the current limiters of VSCs on the perfomance of the FVBs proposed has been investigated by comparing two situations:

- CSA current limitation of $i_{s,i}^{max} = 1.25\ pu$ with equal priority to d-axis and q-axis currents has been imposed to all VSCs (the same strategy used so far).
- Simulation has also been carried out without current limitations on the VSCs. However, this is not a realistic case because the current limitation is mandatory for protection of the converter station.

Table 5.3 shows the CCTs for different faults of Table A.3, obtained for the base case, strategy FVB-L, and strategy FVB-WACS. Parameters of strategies FVB-L and FVB-WACS are provided in the Appendix.

The result shows that the current limiters in GFM-VSCs will surely impact on transient stability of these types of systems as previously shown in [**Qoria'20**b]. All three cases included in Table 5.3 are affected although a general pattern cannot be drawn without exceptions. in most cases, current limits reduce CCTs but this is not always the case (see Fault IV in Table 5.3). In fact, sometimes voltage sags during the fault are less severe if there is no current limitation in the converter station and strategy FVB may not be activated. However, Table 5.3 shows that current limiters and FVBs are compatibles and the former does not jeopardise the benefits of the latter.

Table 5.3: Impact of current limiter (CL) of the VSCs. Critical clearing times (CCTs).

CCT	**Base case**		**FVB-L**		**FVB-WACS**	
(ms)	with CL	without CL	with CL	without CL	with CL	without CL
Fault I	130	210	250	200	270	340
Fault II	270	380	310	380	360	460
Fault III	220	550	220	530	230	620
Fault IV	420	340	420	340	880	820

5.5.4 Impact of communication latency

The impact of communication latency on the performance of the FVB-WACS strategy, using CSA and HCL current limitation algorithms, has been analysed. The input error signal of the supplementary controller of Figure 4.5 with a communication delay reads:

$$u_i = e^{-s\tau}(\omega_{COI} - \omega_i) \tag{5.8}$$

where τ is the communication delay. The work in [**Zhang'15**] reported total communication delays in WACS within the range of 50-80 ms. Total communication latency delays of 50 ms and 100 ms will be considered in this work. The FVB-WACS strategy requires a communication system to transmit global measurements of the center of inertia. With this strategy, the converters can provide a positive or negative supplementary voltage set point when the frequency of the VSCs is above or below the frequency of the COI.

Table 5.4 summarises the CCTs when the delays in communication systems are considered using CSA and HCL current limiters. Three cases of communication latency using strategies FVB-WACS are compared (tau= 0

ms, 50 ms and 100 ms). The CCTs decrease as the communication delay increases. However, the CCTs obtained with the FVB-WACS strategy are higher than the ones obtained in the base case and the FVB-L strategy, even with communication delays up to 100 ms.

Furthermore, the CCTs obtained with FVB-WACS using HCL follow a similar pattern as when CSA alone is used. Although HCLs produce improvements in transient stability, they have no impact on the communication system latency. Results of Table 5.4 prove that strategy FVB-WACS is robust against communication latency when using the two options of current-limitation strategies: CSA and HCL. This control feature produces better results than the FVB-L strategy since it uses global measurements (the COI frequency), making it more susceptible during transients and resulting in more significant improvements.

Table 5.4: FVB-WACS with time delay

	CSA			**HCL**		
(ms)	$\tau = 0$ ms	50 ms	100 ms	$\tau = 0$ ms	50 ms	100 ms
Fault I	270	270	260	290	290	280
Fault II	360	340	320	370	370	360
Fault III	230	230	230	700	700	690
Fault IV	880	870	890	930	950	940

5.6 Conclusions

The conclusions obtained in this chapter can be summarised as follows:

- Transient stability is improved significantly with the proposed fast voltage boosters (FVB-L and FVB-WACS), when using conventional current saturation algorithm (CSA) and hybrid current limiter (HCL).
- Improvements are higher when using the proposed stategies FVB-L nad FVB-WACS with HCL current limiter.
- Results show that FVBs and HCLs are compatible and complementary.
- The effectiveness of FVBs when using HCLs is due to the fact that actions of both controllers take place at different stages of the transient. During the fault, the HCL has priority and it introduces a supplementary voltage set point to the GFM-VSC. After the fault clearing, the

HCL does not act any more and then FVB introduces a supplementary voltage set point to the GFM-VSC. Hence, the use of FVBs together with HCLs takes advantages of both.

- FVB-WACS is robust against communication latency, when using both current-limitation algorithms analysed (CSA and HCL).

Chapter 6

Active-Power control strategies for transient stability improvement

6.1 Introduction

This chapter proposes a local active-power (TSP-L) control strategy using local measurements as the control input to improve the transient stability of power systems with 100% GFM-VSC-based generator. The proposed TSP-L control strategy is analysed and compared with two other active power control approaches in GFM-VSCs for transient stability improvements within power systems. The three strategies evaluated are the active power control using a wide-area control system (TSP-WACS) [**Choopani'19**], the local active power control using a transient damping method (TSP-TDM) [**Xiong'21**a], and the local active power control strategy (TSP-L) proposed in this thesis. Simulations were conducted to assess the effectiveness of these strategies in increasing the critical clearing time (CCT) of the examined faults. The results illustrate the potential applicability of these strategies on transient stability improvements within power systems.

The rest of the chapter is organised as follows. Section 6.2 reviews the previous work on active-power control strategies for transient stability improvement. Section 6.3 presents the gap covered by the chapter. Section 6.4 presents the analysis of the three active-power control strategies mentioned above: TSP-L, TSP-WACS, and TSP-TDM. The description of each strategy in detail is provided in this section. Section 6.6 presents the results of the

short-circuit simulation and the impact of communication latency on critical clearing times (CCTs). Finally, Section 6.7 summaryses the key conclusions found in this chapter and their implications for improving transient stability in power systems.

6.2 Review of previous work

The phenomenon of loss of synchronism in large power systems has been studied, and several control strategies have been proposed for improving transient stability based on active-power control. The work in [**Qoria'20**a] goes a step further and analyses transient stability of a GFM-VSC connected to an infinite grid, using virtual-impedance current limiters of the GFM-VSC. The study proposes an adaptative droop in the GFM-VSC by changing the proportional gain of the P-f droop controller during the fault. Results show that the strategy increases the critical clearing times (CCT) of a fault significantly. The studies presented in [**Choopani'19**; **Choopani'20**] introduce a novel approach to improving the stability of power grids with 100% of GFM-VSC-based generators. The work [**Choopani'19**] proposed a P-control strategy, based on a PI controller, that introduces an additional active-power setpoint using the error of the frequency qith respect to the frequency of the Centre Of Inertia (COI) as input signal. The work analyses the impact of communication latency on the performance of the controller. The study demonstrates their method's effectiveness in enhancing transient stability stability of multi-converter systems. Meanwhile, the paper [**Choopani'20**] present the same proposed method, focusing on large disturbances using the frequency deviation with respect to the COI-frequency of the grid as an input signal. Simulation results show that their method efficiently improves transient stability.

Furthermore, the work in [**Collados-Rodriguez'23**] proposed a local active-power control strategy in GFM-VSCs to improve transient stability. The proposed method introduces an additional term is introduced into the P-f droop control if the changes on the output frequency is too high, preventing loss of synchronism. The research presented in [**Xiong'21**a] proposes a supplementary P-control strategy to improve transient stability using a transient damping method (TDM) for a GFM-VSC connected to an infinite grid. The P-control method adds a proportional gain to the frequency deviation with respect to the nominal frequency, using local measurements. The TDM strategy changes its active-power set-point proportionally to its

frequency deviation through a high-pass filter (HPF), as a solution for stabilising power systems. The study also discusses the limitations of the TDM approach and provides guidelines for the design of the proposed controller in improving transient stability in power systems. In contrast to the strategy in [**Choopani'19**], which uses global measurements of the centre of inertia to try to pull all VSC frequencies together to join the COI frequency, the TDM control action slows down all the converters independently when they are close to or far from the faults. This means that the TDM control strategy also slows down the converters below the centre of inertia, jeopardising the transient stability.

Considering this aspect, this chapter proposes a local active-power control strategy (TSP-L) able to be active only for severe-enough faults in a multi-converter system with 100% grid-forming VSC-based generators. Therefore, the TSP-L control will be only activated for those converters that are close to the faults and disabled for those ones far from the faults. The aim of this design is to mitigate the risks associated with the TSP-TDM strategy without jeopardising system stability.

The chapter demonstrates that while all three strategies significantly improve transient stability in such systems, controllers presented in [**Xiong'21**a] and [**Choopani'20**] may require further refinements. For example, some results show that these control strategies could lead to poor results in multi-converter systems, and the control strategy could be improved with logic-activation rules and setting parameters. Short-circuit simulations and critical clearing time analyses are conducted to assess the effectiveness of the active power controllers in enhancing transient stability, demonstrating their efficacy in preventing the loss of synchronism.

6.3 Gap covered by this chapter

A noticeable research gap exists in investigating the P-TDM supplementary controller proposed in [**Xiong'21**a] applied to GFM-VSCs connected to an infinite bus. The question arises regarding its performance and effectiveness when extended to multi-converter systems. Additionally, there is a need to explore effective P-control strategies in GFM-VSCs to improve transient stability in multi-converter systems, especially when using local measurements.

By conducting a thorough analysis and comparison of various P-supplementary controllers designed for GFM-VSCs, this chapter focuses on their effectiveness in improving transient stability in multi-converter systems with

100 % GFM-VSC-based generators. Furthermore, in this chapter, a novel local active-power supplementary controller (TSP-L) is proposed for transient stability improvement in GFM-VSCs. The significance of this proposal lies in its expected effectiveness in multi-converter systems, addressing the identified research gap and advancing the understanding of control strategies in complex power system configurations.

Specifically, the main contributions of this chapter are as follows:

- Proposal of local active power control strategy to improve transient stability of power systems with 100% of GFM-VSC-based generation.
- Comparison of the proposed control strategy with two control strategies based on both global measurements (TSP-WACS) and local measurements (TSP-TDM).
- Demonstration of the effectiveness of the control approaches in significantly improving the critical clearing times of different faults.
- Analysis of the impact of communication latency on the global control strategy (TSP-WACS) showing that the proposed control strategy is robust for realistic communication latency.

To evaluate the effectiveness of the TSP-L strategy in comparison to the other two strategies, numerical simulations are conducted on a multi-converter system with GFM-VSC-based generators, specifically using Kundur's two-area test system [**Kundur'94**] with 100% GFM-VSC-based generation. The evaluation is carried out using the same simulation model that has been used in the previous chapters. The simulation included detailed modelling of system components such as lines, loads, and controllers. However, switching converters were represented as ideal variable voltage sources. This comprehensive simulation setup enabled the analysis and evaluation of control strategies in a realistic power system scenario. As a result, their impact on transient stability and overall system behaviour could be reliably assessed.

6.4 Active-Power control strategies

This section describes two active-power control strategies in GFM-VSC with VSM control. One of these strategies uses local measurements, and the other uses global measurements that consider the frequency of the center of

inertia (COI). Both types of strategies have shown significant improvements in transient stability.

Two control strategies are analysed in this section:

- Active-power control using a wide-area control system (TSP-WACS) presented in [**Choopani'19**].
- Local Active-power control using transient damping method (TDM) proposed in [**Xiong'21**a].

6.4.1 Active-power control using a wide-area control system (TSP-WACS) [Choopani'19]

Similarly to the case of the control strategy with local measurements, this control strategy follows the same principle as its analogue FVB-WACS (see Chapter 4), using the speed of the COI. This chapter aims to compare the proposed controller with the proposal in [**Choopani'19**], which uses the speed of the COI and applying PID controllers, and to investigate further improvements This controller works using an active-power control in each GFM-VSC within a wide-area control system (TSP-WACS). Yet, in this case, the control set-point value is the active power injection ($p_{g,i}$) shown in Figure 6.1.

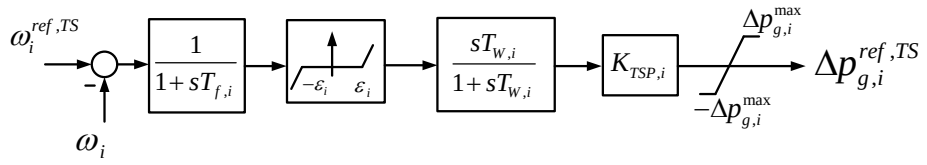

Figure 6.1: Strategy TSP-WACS.

The philosophy of the TSP-WACS controller follows the same principle as its FVB analog, but with slight differences in terms of activation, as explained below:

- If the frequency of VSC-i is above the frequency of the COI, VSC-i will decrease its active-power setpoint, trying to slow VSC-i down.
- If the frequency of VSC-i is below the frequency of the COI, VSC-i will increase its active-power setpoint, trying to accelerate VSC-i.
- Therefore, control actions will pull together the frequencies of GFM-VSCs of the system.

6.4.2 Local Active-power control using transient damping method (TSP-TDM) [Xiong'21a]

This control strategy consists of the damping method in VSM proposed in [**Xiong'21**a] for transient stability improvement in GFM-VSCs connected to infinite gird. The input of the controller of TSP-TDM is the frequency deviation of each GFM-VSC-i, with respect to an absolute reference frequency, $\Delta\omega_i = \omega_i - \omega_{0,pu}$. Figure 6.2 shows the scheme of the TDM implemented in a GFM-VSC with VSM control.

The TDM control strategy consists of a gain ($K_{TSP,i}$) and a wash-out filter (with a time constant of $T_{W,i}$). Although not discussed in [**Xiong'21**a], this work includes a saturation parameter to limit the contribution of control actions (such as the TSP-L and TSP-WACS controllers) for a fair comparison, denoted as $\pm\Delta p_{g,i}^{max}$. The controller takes the frequency deviation ($\Delta\omega_i$) calculated by the VSM algorithm of the GFM-VSC as input, and its output is a supplementary active-power set point ($\Delta p_{g,i}^{ref,TS}$). In the TDM control strategy, each GFM-VSC adds a supplementary active-power set point that is proportional to the frequency deviation, which uses only local information.

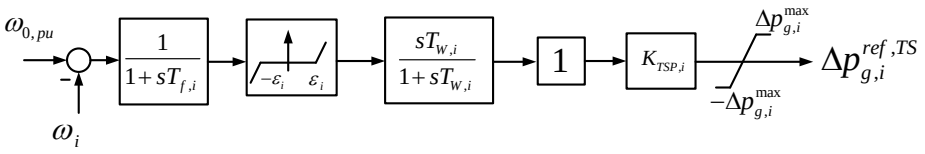

Figure 6.2: Strategy TSP-TDM.

TSP-TDM control strategy uses the frequency deviation of each GFM-VSC-i as an input, and the philosophy of its activation is as follows:

- If the frequency of VSC-i (ω_i) is above the base frequency ($\omega_{0,pu}$), VSC-i will decrease its active-power setpoint, trying to slow VSC-i down.
- If the frequency of VSC-i (ω_i) is below the base frequency ($\omega_{0,pu}$), VSC-i will increase its active-power setpoint, trying to accelerate VSC-i.

In contrast to the TSP-WACS, which uses global measurements of the centre of inertia to try to pull all VSC frequencies together to join the COI frequency, the TDM control action slows down all the converters independently when they are close to or far from the faults. This means that the

TDM control strategy also slows down the converters below the centre of inertia, which would jeopardise the transient stability.

Notice that this control approach has the same structure and configuration as the self-synchronisation strategy VSM without PLL using a wash-out filter, previously analysed in Chapter 3.

6.5 Local Active-power control (TSP-L)

This Section introduces the proposed local active-power (TSP-L) control strategy to improve transient stability in multi-converter systems. This proposed control strategy follows the same principle as that used in the FVB-L (see Chapter 4); which is based on the use of local measurements as input signals: the voltage at the terminal and the frequency deviation (in pu) of each GFM-VSC-i. The block diagram is shown in Figure 6.3. It is a similar diagram of Figure 4.3 of Chapter 4, but in this case, the control set-point value is the active-power set-point ($\Delta p_{g,i}^{ref,TS}$) instead voltage at the terminal of VSC-i ($v_{f,i}$) as in the case of the FVB-L strategy.

The activation philosophy for the TSP-L strategy shown in Figs. 6.3 and 6.4 is as follows:

- Binary variable $\gamma_{1,i}$ is set to 1 if a voltage sag is detected with an hysteresis, as shown in Figure 6.3. If $v_{g,i} \leq v_{A,i}$, then $\gamma_{1,i} = 1$ and remains equal to 1 until $v_{g,i} > v_{B,i}$. if a fault is not detected, then $\gamma_{1,i} = 0$.

- Binary variable $\gamma_{2,i}$ is set to 1 if the frequency deviation of GFM-VSC-i (with respect to the nominal frequency) is greater than or equal to a certain threshold: $\Delta\omega_i \geq \omega_{thres,i}$. Otherwise, $\gamma_{2,i} = 0$.

- The supplementary controller is activated with binary variable γ_i, which is the result of a logic circuit with $\gamma_{1,i}$ and $\gamma_{2,i}$ as inputs, as shown in Figure 6.3.

- The supplementary active-power set point is given by: $\Delta p_{g,i}^{ref,TS} = \gamma_i \Delta p_{g,i}^{max}$, where $\Delta p_{g,i}^{max} > 0$ is a parameter of the controller ($\gamma_i = 0$ if the controller is deactivated and $\gamma_i = 1$ if the controller is activated).

The logic used to activate the controller can then be summarised as follows:

- The controller will be activated if a voltage sag is detected. Therefore, $\gamma_{1,i}$ will drive the activation of the controller.
- Once the controller is activated, the supplementary active-power set-point is maintained if at least one of the two following conditions are satisfied: undervoltage ($\gamma_{1,i} = 1$) or frequency greater than or equal to the threshold ($\gamma_{2,i} = 1$).

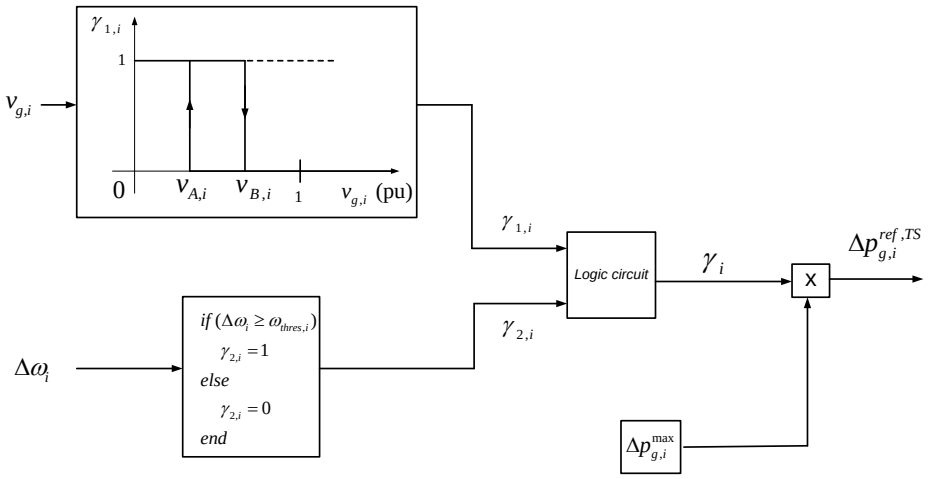

Figure 6.3: Strategy TSP-L.

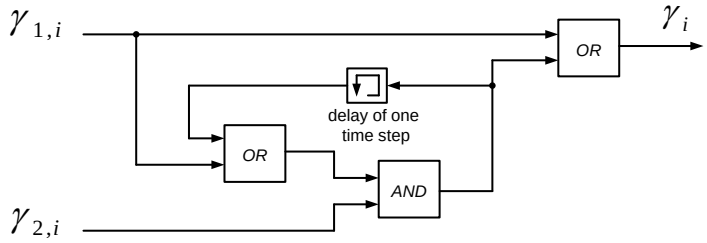

Figure 6.4: Strategy TSP-L. Logic circuit for fault detection.

Unlike the TSP-TDM strategy, which was proposed for GFM-VSCs connected to an infinite grid and activated for even converters far from the fault, the control action rules of the TSP-L strategy only activate the control for

severe enough fault, thus avoiding its activation for those converters very far from the fault (VSCs which frequencies are bellow the COI frequency).

6.6 Results

This section examined the behaviour of Kundur's two-area test system in [**Kundur'94**], but using 100% grid-forming VSC-based generation. System Data and the one-line diagram are provided in Appendix A (Table A.4 and Figure A.3).

Four cases are compared:

- Base case: no supplementary controller for transient stability is implemented in the GFM-VSCs.
- TSP-L: VSCs applying TSP-L strategy (Figs. 6.3 and 6.4), with parameters: $v_{A,i} = 0.50$ pu, $v_{B,i} = 0.9$ pu, $\omega_{thres,i} = 10^{-3}$ pu, $\Delta p_{g,i}^{max} = 0.15$ pu.
- TSP-WACS: VSCs applying TSP-WACS strategy (Figure 6.1), with parameters: $K_{TSP,i} = 100$ pu, $T_{f,i} = 0.1$ s, $T_{W,i} = 10$ s, $\Delta p_{g,i}^{max} = 0.15$ pu and $\epsilon_i = 10^{-3}$ pu.
- TSP-TDM: VSCs applying TSP-TDM strategy (Figure 6.2) with parameters: $K_{TSP,i} = 100$ pu, $T_{f,i} = 0.1$ s, $T_{W,i} = 10$ s, $\Delta p_{g,i}^{max} = 0.15$ pu and $\epsilon_i = 10^{-3}$ pu.

6.6.1 Short-circuit simulation

Fault I described in Table A.3 is applied at $t = 1$ s and cleared after 150 ms. Figure 6.5 shows the angle difference between VSC-1 and VSC-3, while Figure 6.6 shows the frequency deviations of the VSCs with respect to the frequency of the COI. In the base case, VSC-based generators lose synchronism. However, synchronism is maintained with the three supplementary controllers (TSP-L, TSP-TDM and TSP-WACS).

Figure 6.7 shows the supplementary active-power set-point provided by the control strategies and the active-power injections of the VSCs. Local strategies TSP-L is only activated in VSCs 1 and 2, which are close to the fault and not in VSCs 3 and 4, which are far from it. This local strategy is also effective in multi-converter systems with 100% of grid-forming-based

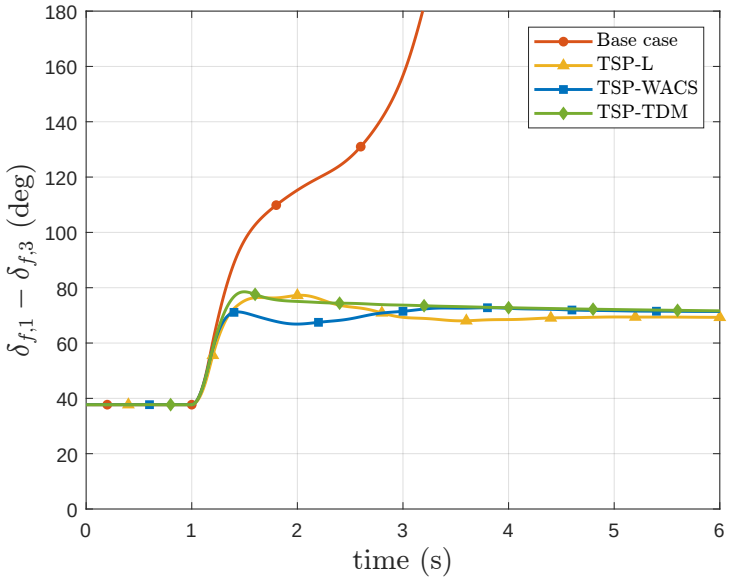

Figure 6.5: Fault I cleared after 150 ms. Angle difference of the VSCs applying TSP controllers.

generation. This is the consequence of the logic rules in Figure 6.4. The TSP-TDM strategy is activated in all converters, providing a larger supplementary power set-point to the converters that are closer to the fault, based on the frequency deviation of each GFM-VSC-i as input in the TSP-TDM strategy (see Figure 6.2). It is important to note that the frequency deviation is always negative because it is measured relative to an absolute frequency set-point, which is the nominal frequency ($\omega_{0,pu} = 1$ pu), and all the VSCs tend to accelerate during faults. These accelerations result in the frequency of each VSC being higher than the frequency set-point. Therefore, the control action aims to decelerate all the VSCs simultaneously.

In control strategy TSP-WACS, a negative supplementary active-power set point is provided by VSCs 1 and 2 when just the fault occurs because their frequencies are above the frequency of the COI (see Figure 6.6). Meanwhile, VSCs 3 and 4 provide a positive supplementary active-power setpoint during the first swing because their frequencies are below the frequency of the COI. Therefore, VSCs 1 and 2 will slow down while VSCs 3 and 4 will accelerate, reducing the risk of loss of synchronism.

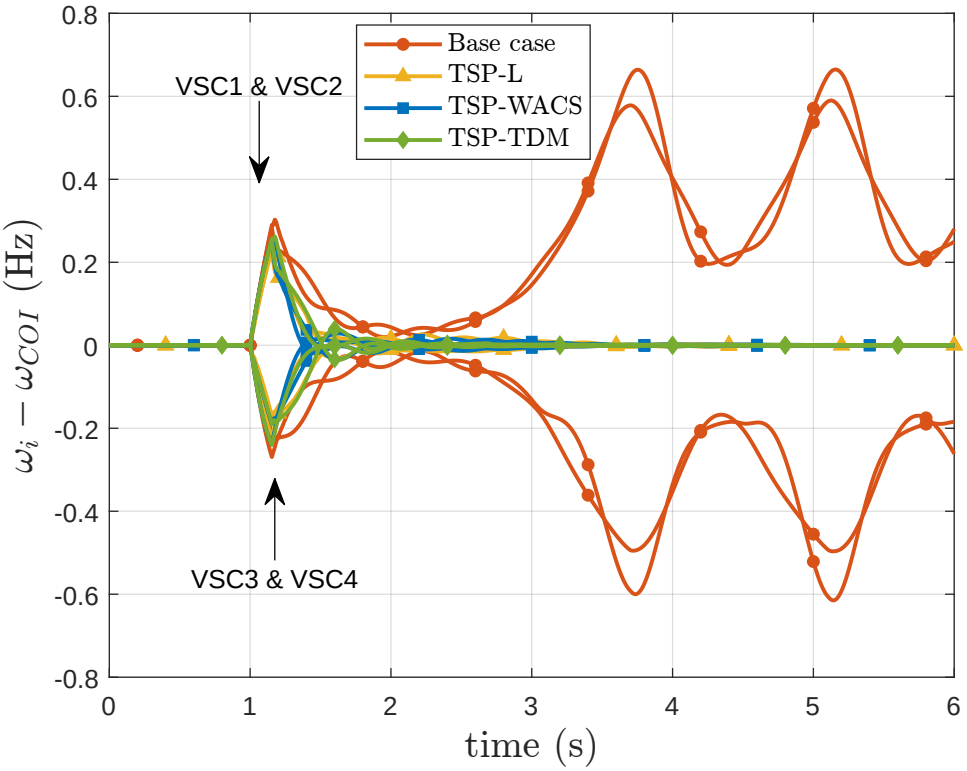

Figure 6.6: Fault I cleared after 150 ms. Frequency deviations of the VSCs with respect to the frequency of the COI applying TSP controllers.

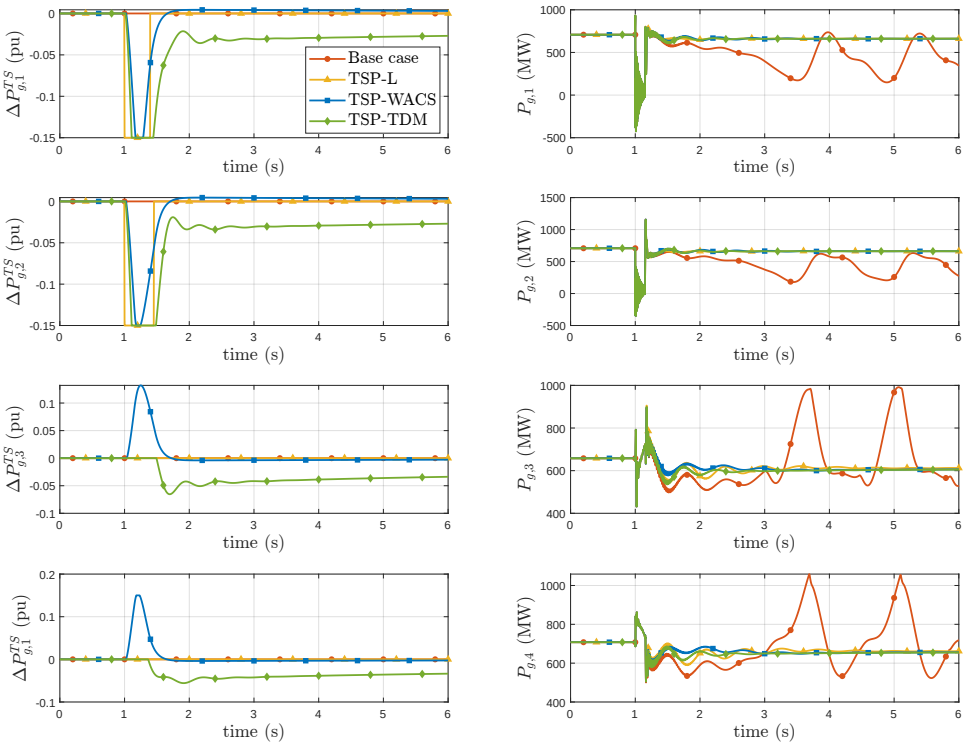

Figure 6.7: Fault I cleared after 150 ms. (left) Active-power set-points and (right) active-power injections of each VSC applying TSP controllers.

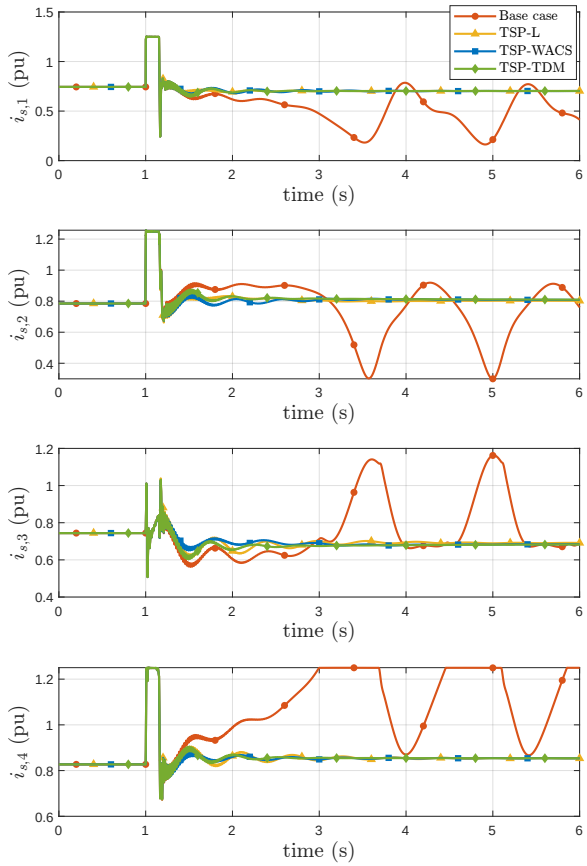

Figure 6.8: Fault I cleared after 150 ms. Current injections of the VSCs applying TSP controllers.

Finally, Figure 6.8 illustrates the current injections of each VSCs during the simulation. When a fault occurs, the current limiters of the converters are activated in cases where the current limit is reached. The current injections of VSCs 1, 2, and 3, which are located close to the fault, experience a peak where they reach their maximum allowed value ($i_{s,i}^{max} = 1.25$). These findings demonstrate that the P control strategies used in the study are compatible with the current limiters of the VSCs, similar to the findings observed with the fast voltage boosters (FBVs) strategies in the chapters 4 and 5.

6.6.2 Critical clearing times (CCTs)

The critical clearing time (CCT) of several faults described in Table A.3 are provide in Table 6.1. The base case is provided as a reference the table and the subsequent columns correspond to different supplementary control strategies: TSP-L, TSP-TDM, and TSP-WACS. Active-power control strategies were implemented in all GFM-VSCs of Figure A.3 (see Appendix A).

The three P-supplementary controllers significantly increase the CCTs of all faults in comparison with the base case. Each strategy is evaluated with different parameter settings, indicated by the values in the table. For each fault scenario (Fault I, Fault II, Fault III, and Fault IV), the CCT values are presented for each strategy and parameter configuration. A wash-out-filter time constant of $T_{W,i} = 10$ s was selected for TDM and TPS-WACS strategies. Two different values of gain $K_{TSP,i}$ ($K_{TSP,i} = 100$ pu and $K_{TSP,i} = 50$ pu) are used to compare the performance of the TDM strategy. Similarly, the TSP-WACS strategy compares two values of the gain $K_{TSP,i}$ parameter ($K_{TSP,i} = 100$ pu and $K_{TSP,i} = 50$ pu). Finally, the saturation parameter of the TSP strategies was selected as $\Delta p_{g,i}^{max} = 0.15$ pu, since the supplementary active-power set point should be bounded for practical applications.

Table 6.1 depicts that different strategies and parameter settings impact the CCTs differently. For example, in Fault IV, the TSP-TDM strategy with $K_{TSP,i} = 100$ pu achieves a CCT of 540 ms, while with $K_{TSP,i} = 50$ pu yields a CCT of 600 ms (these parameters are a feasible design, according to the guidelines provided in reference [**Xiong'21**a]).

The performance of the TSP-WACS strategy varies depending on the fault scenario. For Fault I, a value of $K_{TSP,i} = 50$ pu yields a better performance, with a CCT of 290 ms compared to a CCT of 280 ms when $K_{TSP,i} = 100$pu. However, for the rest of the faults, the opposite behavior is observed. The TSP-WACS strategy exhibits better behaviour in terms of CCTs when a value of $K_{TSP,i} = 100$ pu is used compared to $K_{TSP,i} = 50$ pu.

The TSP-L strategy shows different CCT values depending on the voltage threshold ($v_{A,i}$). The TSP-L strategy increases the CCTs for Faults I, II, and III, except for Fault IV. In the case of Fault IV, the CCT decreases from 420 ms in the base case to 300 ms when $v_{A,i} = 0.75$ pu is used but when the threshold is set at $v_{A,i} = 0.5$ pu, the CTTs maintains the same value as the bases case at 420 ms. The absence of negative impact on the critical clearing times (CCTs) for all fault scenarios can be attributed to the specific conditions under which the local strategy TSP-L is activated, as described

in Section 6.4. By carefully designing the activation thresholds, the TSP-L strategy is only triggered for severe faults. This selective activation ensures that the strategy does not introduce any adverse effects for less severe faults. To illustrate this, consider the example where the parameter $v_{A,i}$ in Figure 6.3 is changed from 0.75 pu to 0.5 pu. Despite this change, the CCT for Fault IV remains unchanged, as shown in Table 6.1. This demonstrates that the TSP-L strategy, with a $v_{A,i}$ value of 0.5 pu, is capable of delivering improved results without negatively impacting the system's stability. Therefore, for the remainder of the chapter, a value of $v_{A,i} = 0.5$ pu will be used for the TSP-L strategy. This choice has been found to yield better results, and the specific parameter values can be found in the Appendix. By carefully selecting the activation thresholds and parameter values, the TSP-L strategy ensures that it provides effective supplementary control only when necessary, without compromising the system's stability under normal operating conditions. This highlights the importance of tuning the control parameters to achieve optimal performance in power systems with grid-forming VSC-based generation.

Table 6.1: Critical clearing times (CCTs) for TSPs.

CCT (ms)	**base case**	**TSP-L** $v_{A,i} = 0.75$ pu	**TSP-L** $v_{A,i} = 0.5$ pu	**TSP-TDM**	**TSP-WACS** $\tau = 0$ ms	with 50 ms	delay 100 ms
Fault I	130	300	300	240	280	270	270
Fault II	270	390	390	350	430	410	390
Fault III	220	260	260	250	320	300	270
Fault IV	420	300	420	600	1520	1420	1410

Table 6.2: Critical clearing times (CCTs) for TSPs.

CCT (ms)	**base case**	**TSP-L** $v_{A,i} = 0.75$ pu	**TSP-L** $v_{A,i} = 0.5$ pu	**TSP-TDM** $K_{TSP,i} = 100$ pu	**TSP-TDM** $K_{TSP,i} = 50$ pu	**TSP-WACS** $K_{TSP,i} = 100$ pu	**TSP-WACS** $K_{TSP,i} = 50$ pu
Fault I	130	300	300	230	240	280	290
Fault II	270	390	390	350	350	430	390
Fault III	220	260	260	250	250	320	270
Fault IV	420	300	420	540	600	1520	1410

6.6.3 Impact of the activation of the TSP controllers in different areas.

Tables 6.3 and 6.4 present the critical clearing times (CCTs) for the three different supplementary control strategies when they are activated in two separate areas. Table 6.3 displays the CCTs for Area 1, while Table 6.4 shows

the CCTs for Area 2. The base case is used as a reference in both tables, and each column represents a different supplementary control strategy: TSP-L, TSP-TDM, and TSP-WACS. The impact of various parameter settings on the CCTs is also examined.

In Area 1, the TSP-L strategy increases the CCTs for Faults I, II, and III compared to the base case. However, for Fault IV, the CCT remains the same as the base case. This behaviour is attributed to the specific conditions under which the TSP-L strategy is activated. By carefully designing the activation thresholds, the TSP-L strategy is triggered only for severe faults, ensuring that it does not introduce any adverse effects for less severe faults. The TSP-TDM and TSP-WACS strategies show different effects on the CCTs depending on the fault scenario in Area 1. For Fault I, both strategies with different parameter settings result in improved CCTs compared to the base case. However, for Faults II and III, the CCTs are similar to or slightly worse than the base case. In the case of Fault IV, both strategies significantly increase the CCTs.

In Area 2, the TSP-L strategy does not have any impact on the CCTs for Faults I and II, as the values remain the same as the base case. For Fault III, the CCT increases when the TSP-L strategy is activated. However, for Fault IV, the TSP-L strategy increases the CCTs compared to the base case. The behavior of the TSP-L strategy in Area 2 differs from that in Area 1, highlighting the influence of the specific system conditions and fault scenarios. The TSP-TDM strategy in Area 2 shows no improvement in the CCTs for Faults I and II. For Fault III, the CCTs remain similar to the base case, while for Fault IV, the TSP-TDM strategy with the specific parameter settings results in a CCT of 0 ms. This indicates that the TSP-TDM strategy is not effective in mitigating the fault for Area 2 in this scenario. The TSP-WACS strategy in Area 2 improves the CCTs for Faults I and III compared to the base case. However, for Faults II and IV, the CCTs increase significantly when the TSP-WACS strategy is activated. A CCT of zero milliseconds (0 ms) means that a fault of very short duration (e.g., fault clearance of 10 ms) plus the disconnection of the faulted line produces a loss of synchronism.

Table 6.3: Critical clearing times (CCTs) for TSPs. Area 1

CCT (ms)	**base case**	**TSP-L** $v_{A,i} = 0.5$ pu	**TSP-TDM** $K_{TSP,i} = 100$ pu	**TSP-WACS** $K_{TSP,i} = 100$ pu
Fault I	130	300	270	230
Fault II	270	390	360	350
Fault III	220	220	220	320
Fault IV	420	420	1080	840

Table 6.4: Critical clearing times (CCTs) for TSPs. Area 2

CCT (ms)	**base case**	**TSP-L** $v_{A,i} = 0.5$ pu	**TSP-TDM** $K_{TSP,i} = 100$ pu	**TSP-WACS** $K_{TSP,i} = 100$ pu
Fault I	130	130	0	230
Fault II	270	270	250	350
Fault III	220	260	250	610
Fault IV	420	420	0	790

6.6.4 Impact of communication latency

Furthermore, it is important to analyse the influence of communication latency on the performance of the TSP-WACS strategy. To investigate this, the input error signal of the supplementary controller in Figure 6.1 will be subjected to a delay represented by τ in the following equation:

$$u_i = e^{-s\tau}(\omega_{COI} - \omega_i) \tag{6.1}$$

Here, τ denotes the communication delay. Previous studies, such as the one conducted in **[Zhang'15]**, have reported total communication delays in wide-area control systems (WACS) ranging from 50 to 80 ms. In this particular study, we will consider communication latency delays of 50 ms and 100 ms.

While there may be faults, such as Fault IV, in which the control strategies will have no impact, overall, the TSP-WACS strategy demonstrates better results compared to TSP-L and TSP-TDM. Moreover, the results presented in Table 6.5 provide evidence that the TSP-WACS strategy is robust against communication latency. Table 6.5, presents the critical clearing times (CCTs) for the TSP-WACS strategy with different communication latency delays. It includes scenarios where $K_{TSP,i}$ is set to 100 pu. As observed, the CCTs for various fault scenarios are influenced by the communication delay. However, even with the presence of latency, the TSP-WACS strategy consistently outperforms the other strategies in terms of improving transient

stability.

These findings highlight the significance of considering communication latency in the design and implementation of wide-area control systems. The robust performance of the TSP-WACS strategy, even with communication delays of 50 ms and 100 ms, demonstrates its ability to effectively mitigate transient stability issues.

Table 6.5: Critical clearing times (CCTs) for TSP-WACS with delay.

CCT (ms)	**TSP-WACS** with delay		
	$\tau = 0$ ms	50 ms	100 ms
Fault I	280	270	270
Fault II	430	410	390
Fault III	320	300	270
Fault IV	1520	1420	1410

6.6.5 Discussion on the use of the three P control strategies

This section discusses the implementation and effectiveness of the three control strategies analysed in this chapter. The TSP-L and TSP-WACS strategies, involve local active-power control, where each grid-forming VSC utilises only local measurements. On the other hand, the second strategy uses a wide-area control system that requires global measurements and, consequently, a communication system. In terms of implementation, local strategies are considered easier and more cost-effective since they rely solely on local measurements. In contrast, the TSP-WACS strategy requires a communication system to gather global measurements, making it more complex and potentially more expensive to implement.

The effectiveness of the control strategies is evaluated based on their ability to improve transient stability. The ideal control actions involve supplying a positive supplementary voltage to VSCs with frequencies above the frequency of the center of inertia (COI) and a negative supplementary voltage to VSCs with frequencies below the COI. The TSP-WACS strategy, which utilises global measurements, generally yields better results than the TSP-L and TDM strategies because it has access to the frequency of the COI. The activation thresholds of the TSP-L strategy can be tuned to ensure that the control strategy is activated only for sufficiently close faults, which typically correspond to faults producing frequencies above the COI. This selective activation mechanism allows the TSP-L strategy to target severe faults while

avoiding unnecessary intervention for less severe faults.

Both TSP-L and TSP-TDM strategies can be implemented in grid-forming VSCs to improve transient stability for severe faults. They provide effective control mechanisms without the need for a communication system. However, despite their increased complexity, the use of the TSP-WACS strategy could be a valuable option in power systems that are particularly vulnerable to transient stability issues. The TSP-WACS strategy can potentially deliver more significant improvements by utilising global measurements and better capturing the system's dynamics.

6.7 Conclusions

The conclusions obtained in this chapter are as follows:

- Strategy TSP-WACS (global measurements), proposed in previous work improves transient stability for when close and remote faults occur and it improves their critical clearing times (CCTs) significantly.
- Strategy TSP-WACS (local measurements), proposed in previous work, improves transient stability when close faults occur, but it jeopardises transient stability for some remote faults.
- Strategy TSP-L (local measurements), proposed in this chapter of the thesis, improves transient stability when close faults occur and it does not jeopardise transient stability in case of remote faults. Achieving this when using local measurements, only, is an advantage.
- The effect of control parameters of active-power has been analysed to provide design guidelines tuning the parameter values by simulation. High values of saturation parameter or gains can improve the effectiveness of the control strategies, but setting them too high can jeopardise the stability.

Chapter 7

Conclusions and contributions

This thesis aimed to investigate control strategies in GFM-VSCs to improve transient stability of power systems with 100% converter-interfaced generation. This chapter summarises the conclusions and contributions of this thesis and suggests potential avenues for future research.

7.1 Conclusions

The main conclusions and findings derived from this thesis are summarised below.

7.1.1 Self-synchronisation strategies in GFM-VSCs

- The four self-synchronisation mechanisms for GFM-VSCs analysed in this thesis (VSM without PLL, VSM with PLL, VSM without PLL + wash-out and IP controller) can have a similar behaviour under small disturbances, for a proper tuning of the parameters. However, they can have different behaviour under large disturbances, due to non-linearities.
- Strategies VSM with PLL and VSM without PLL + washout produce the best results in terms of transient stability.
- Strategies VSM without PLL and IP control produce the lowest critical clearing times (CCTs).
- The Virtual active-power controller (VAPC) improves the CCTs in all cases, and it can be applied to all self-synchronisation strategies in

GFM-VSCs.

7.1.2 Fast voltage boosters (FVBs)

- The proposed local strategy FVB-L improves transient stability of severe faults, significantly, and their critical clearing times (CCTs) are increased. However, its control actions must be restricted to severe-enough faults by proper tuning activation thresholds. This means that this control strategy will have little effect on transient stability when remote faults occur.

- The proposed global strategy FVB-WACS improves transient stability, significantly, improving their CCTs. It produces significant improvements for severe and non-severe faults. The control strategy is robust when subject to communication latency.

- FVB-L strategy uses local measurements. Hence, its implementation is easier and cheaper. Meanwhile, FVB-WACS requires a communication system to use global measurements, having, therefore, a more difficult and expensive implementation. A trade-off should be made when choosing using FVB-L or FVB-WACS. In general, the implementation of FVB-L improving transient stability only for faults close to the GFM-VSC could be a cost-effective and practical solution. Nevertheless, in power systems which are vulnerable to transient stability, FVB-WACS could be a more effective solution, improving transient stability of severe and non-severe faults.

- The effect of control parameters of strategies FVB-L and FVB-WACS has been analysed to provide design guidelines tuning the parameter values by simulation. High values of $\Delta v_{f,i}^{max}$ and $K_{FVB,i}$ can improve the effectiveness of the control strategy, but setting them too high can jeopardise the stability or cause the GFM-VSC to reach its limits, leading to non-linearities that can reduce the effect of the control strategy.

7.1.3 Current limiters and FVBs

- Transient stability is improved significantly with the proposed fast voltage boosters (FVB-L and FVB-WACS), when using conventional current saturation algorithm (CSA) and hybrid current limiter (HCL).

- Improvements are higher when using the proposed stategies FVB-L nad FVB-WACS with HCL current limiter.

- Results show that FVBs and HCLs are compatible and complementary.
- The effectiveness of FVBs when using HCLs is due to the fact that actions of both controllers take place at different stages of the transient. During the fault, the HCL has priority and it introduces a supplementary voltage set point to the GFM-VSC. After the fault clearing, the HCL does not act any more and then FVB introduces a supplementary voltage set point to the GFM-VSC. Hence, the use of FVBs together with HCLs takes advantages of both.
- FVB-WACS is robust against communication latency, when using both current-limitation algorithms analysed (CSA and HCL).

7.1.4 Active-power control strategies

- Strategy TSP-WACS (global measurements), proposed in previous work improves transient stability for when close and remote faults occur and it improves their critical clearing times (CCTs) significantly.
- Strategy TSP-WACS (local measurements), proposed in previous work, improves transient stability when close faults occur, but it jeopardises transient stability for some remote faults.
- Strategy TSP-L (local measurements), proposed in this chapter of the thesis, improves transient stability when close faults occur and it does not jeopardise transient stability in case of remote faults. Achieving this when using local measurements, only, is an advantage.
- The effect of control parameters of active-power has been analysed to provide design guidelines tuning the parameter values by simulation. High values of saturation parameter or gains can improve the effectiveness of the control strategies, but setting them too high can jeopardise the stability.

7.2 Scientific Contributions of the thesis

The main scientific contributions of this thesis are summarised below.

7.2.1 Self-synchronisation strategies in GFM-VSCs

- A comprehensive analysis and evaluation of grid-forming self-synchronisation methods for GFM-VSCs.
- Analysis of the impact of grid-forming self-synchronisation methods for GFM-VSCs on transient stability.
- Various methods and techniques proposed in the literature are discussed, allowing for a thorough examination of the self-synchronisation approaches. The advantages, limitations, and performance characteristics of these methods are analysed under different operating conditions.
- Understanding of the capabilities of self-synchronisation strategies, providing valuable insights for the design and implementation of GFM-VSCs.

7.2.2 Fast voltage boosters (FVBs)

- Proposal of FVBs in GFM-VSCs to improve transient stability:
  - FVB-L: Local FVB (local measurements).
  - FVB-WACS: FVB using a wide-area control system (global measurements).
- Analysis of the impact of communication latency of strategy FVB-WACS.
- Analysis of the impact of control parameters of the proposed FVBs and guidelines for design.
- Analysis of the proposed FVBs in power systems with 100 % converter-interfaced generation.

7.2.3 Current limiters and FVBs

- Investigation of the impact of the hybrid current limiters (HCLs) implemented together with the proposed FVBs on transient stability of power systems with 100% of GFM-VSC-based generation.
  - HCL + FVB-L.
  - HCL + FVB-WACS.
- Demonstration of the effectiveness of both approaches in significantly improving the critical clearing times of different faults.
- Analysis of the impact of communication latency of strategy FVB-WACS, when implemented with HCL limiter.

7.2.4 Active-power control strategies

- Proposal of Local active-power (P) control strategy to improve transient stability of power systems with 100% of converter-interfaced generation (TSP-L), proving its effectiveness for severe faults and not jeopardising the results for remote faults.
- Analysis and comparison of different P-supplementary controllers for GFM-VSCs to improve transient stability.
  - TSP-TDM (local), proposed in previous work.
  - TSP-WACS (global), proposed in previous work.
  - TSP-L (local), proposed in this thesis.
- Analysis of the impact of communication latency of strategy TSP-WACS.
- Analysis of the impact of control parameters of P-control strategies and guidelines for design.
- Analysis of P-control strategies in power systems with 100 % converter-interfaced generation.

7.3 Proposals for further research

Based on the results of this thesis, some proposals for further research are as follows:

- The control strategies proposed and analysed in this thesis to improve transient stability (FVBs and P-control strategies) provide good results. However, their evaluation and verification in experimental platforms could be investigated.
- The proposed control strategies have demonstrated efficacy in transient stability improvement. Nevertheless, there is a need for a more extensive evaluation and validation through in large-scale power systems with 100% non-synchronous generation. Conducting such analyses will yield valuable practical insights into the applicability and performance of these control strategies on a broader scale.
- Analysis of FVB strategies with various current limiter algorithms should be conducted. This thesis was restricted to analysing FVBs with current saturation algorithms (CSAs) and hybrid current limiters (HCLs). Future investigations could explore different current limiter algorithms to provide a more comprehensive understanding of the implications and potential improvements in the performance of FVBs.

7.4 Publications

7.4.1 Journal papers (Chapter 4)

- R. E. Ávila-Martínez, J. Renedo, L. Rouco, A. García-Cerrada, L. Sigrist, T. Qoria, and X. Guillaud, "Fast voltage boosters to improve transient stability of power systems with 100% of grid-forming VSC-Based generation," IEEE Transactions on Energy Conversion, vol. 37, no. 4, pp. 2777–2789, 2022.

7.4.2 Working papers (Chapter 5)

- R. E. Ávila-Martínez, J. Renedo, L. Rouco, A. García-Cerrada, L. Sigrist, T. Qoria, and X. Guillaud, "Impact of current limiters and fast voltage boosters on transient stability of power systems with 100% grid-forming VSC-based generators," submitted to the power system computation conference (PSCC), Paris, France — June 4 – 7, 2024.

7.4.3 Additional publications (conference papers and presentations)

The author of this thesis also participated in additional publications which were not part of this thesis:

- R. E. Ávila-Martínez, L. Rouco, J. García-Aguilar, J. Renedo, L. Sigrist, A. García-Cerrada, Impact of PLL control on small-signal stability of wind DFIGs connected to weak grids, 28º Seminario Anual de Automática, Electrónica industrial e Instrumentación - SAAEI 2021, Ciudad Real (Spain) Online. 07-09 July 2021. In: SAAEI 28º Seminario Anual de Automática, Electrónica Industrial e Instrumentación: Libro de actas, ISBN: 978-84-123292-2-3.

- L. I. de la Barba, L. Sigrist, L. Rouco, R. E. Ávila-Martínez, A. García-Cerrada, Analysis of the effect of control bandwidth on inverter interactions using small-signal stability analysis, 28º Seminario Anual de Automática, Electrónica industrial e Instrumentación - SAAEI 2021, Ciudad Real (Spain) Online. 07-09 July 2021. In: SAAEI 28º Seminario Anual de Automática, Electrónica Industrial e Instrumentación: Libro de actas, ISBN: 978-84-123292-2-3.

- R. E. Ávila-Martínez, L. Rouco, J. García-Aguilar, J. Renedo, L. Sigrist, Impact of PLL control on small-signal stability of wind DFIGs, IEEE Power & Energy Society General Meeting - IEEE PES GM 2020, Montreal (Canada). 03-06 August 2020. In: IEEE PES GM 2020: Conference proceedings, ISBN: 978-1-7281-5509-8

Bibliography

[**Amano'18**] H. Amano and A. Yokoyama. "Rotor Angle Stability Analysis Using Normal form Method with High Penetrations of Renewable Energy Sources-Energy Index for Multi-Swing Stability". In: *2018 Power Systems Computation Conference (PSCC)*. June 2018, pp. 1–6. DOI: 10.23919/PSCC.2018.8442791.

[**Andrade'11**] F. Andrade, J. Cusidó, and L. Romeral. "Transient stability analysis of inverter-interfaced distributed generators in a microgrid system". In: *Proc. European conference on power electronics and applications, birmingham, UK*. 2011, pp. 1–10.

[**Aouini'14**] R. Aouini, K. Ben Kilani, B. Marinescu, and M. Elleuch. "Virtual synchronous generators dynamic performances". In: *2014 International Conference on Electrical Sciences and Technologies in Maghreb (CISTEM)*. Tunis, Tunisia: IEEE, Nov. 2014, pp. 1–6. DOI: 10.1109/CISTEM.2014.7077025.

[**Arghir'18**] C. Arghir, T. Jouini, and F. Dörfler. "Grid-forming control for power converters based on matching of synchronous machines". In: *Automatica*, vol. 95 (2018), pp. 273–282. DOI: https://doi.org/10.1016/j.automatica.2018.05.037.

[**Ávila-Martínez'22**] R. E. Ávila-Martínez, J. Renedo, L. Rouco, A. García-Cerrada, L. Sigrist, T. Qoria, and X. Guillaud. "Fast Voltage Boosters to Improve Transient Stability of Power Systems With 100% of Grid-Forming VSC-Based Generation". In: *IEEE Transactions on Energy Conversion*, vol. 37. no. 4 (Dec. 2022), pp. 2777–2789. DOI: 10.1109/TEC.2022.3199650.

[**Barker'21**] C. Barker, A. Adamczyk, J. Fradley, and O. Jasim. "Providing Synchronous Grid Forming Capability through HVDC Transmission". In:

The 17th International Conference on AC and DC Power Transmission (ACDC 2021). July 2021, pp. 161–166. DOI: 10.1049/icp.2021.2462.

[**Beerten'14**] J. Beerten, O. Gomis-Bellmunt, X. Guillaud, J. Rimez, A. van der Meer, and D. Van Hertem. "Modeling and control of HVDC grids: A key challenge for the future power system". In: *2014 Power Systems Computation Conference*. Aug. 2014, pp. 1–21. DOI: 10.1109/PSCC.2014.7038505.

[**Chamorro'16**a] H. R. Chamorro, M. Ghandhari, and R. Eriksson. "Coherent groups identification under high penetration of non-synchronous generation". en. In: *2016 IEEE Power and Energy Society General Meeting (PESGM)*. Boston, MA, USA: IEEE, July 2016, pp. 1–5. DOI: 10.1109/PESGM.2016.7741186.

[**Chamorro'16**b] H. R. Chamorro, C. A. Ordonez, J. C. Peng, and M. Ghandhari. "Non-synchronous generation impact on power systems coherency". en. In: *IET Generation, Transmission & Distribution*, vol. 10. no. 10 (2016), pp. 2443–2453. DOI: 10.1049/iet-gtd.2015.1233.

[**Chen'22**] M. Chen, D. Zhou, and F. Blaabjerg. "Enhanced Transient Angle Stability Control of Grid-Forming Converter Based on Virtual Synchronous Generator". In: *IEEE Transactions on Industrial Electronics*, vol. 69. no. 9 (Sept. 2022), pp. 9133–9144. DOI: 10.1109/TIE.2021.3114723.

[**Cheng'20**] H. Cheng, Z. Shuai, C. Shen, X. Liu, Z. Li, and Z. J. Shen. "Transient angle stability of paralleled synchronous and virtual synchronous generators in islanded microgrids". In: *IEEE Transactions on Power Electronics*, vol. 35. no. 8 (2020), pp. 1019–1033.

[**Choopani'19**] M. Choopani, S. Hosseinain, and B. Vahidi. "A novel comprehensive method to enhance stability of multi-VSG grids". In: *International Journal of Electrical Power & Energy Systems*, vol. 104 (2019), pp. 502–514. DOI: https://doi.org/10.1016/j.ijepes.2018.07.027.

[**Choopani'20**] M. Choopani, S. H. Hosseinian, and B. Vahidi. "New transient stability and LVRT improvement of multi-VSG grids using the frequency of the center of inertia". In: *IEEE Transactions on Power Systems*, vol. 35. no. 1 (2020), pp. 527–538.

[**Collados-Rodriguez'20**] C. Collados-Rodriguez, M. Cheah-Mane, E. Prieto-Araujo, and O. Gomis-Bellmunt. "Stability Analysis of Systems With High VSC Penetration: Where Is the Limit?" In: *IEEE Transactions on Power Delivery*, vol. 35. no. 4 (Aug. 2020), pp. 2021–2031. DOI: 10.1109/TPWRD.2019.2959541.

[**Collados-Rodriguez'23**] C. Collados-Rodriguez, D. Westerman Spier, M. Cheah-Mane, E. Prieto-Araujo, and O. Gomis-Bellmunt. "Preventing loss of synchronism of droop-based grid-forming converters during frequency excursions". In: *International Journal of Electrical Power & Energy Systems*, vol. 148 (June 2023), p. 108989. DOI: 10.1016/j.ijepes.2023.108989.

[**DArco'13**] S. D'Arco and J. A. Suul. "Virtual synchronous machines - Classification of implementations and analysis of equivalence to droop controllers for microgrids". en. In: *2013 IEEE Grenoble Conference*. Grenoble, France: IEEE, June 2013, pp. 1–7. DOI: 10.1109/PTC.2013.6652456.

[**DArco'14**] S. D'Arco and J. A. Suul. "Equivalence of virtual synchronous machines and frequency-droops for converter-based microgrids". In: *IEEE Transactions on Smart Grid*, vol. 5. no. 1 (2014), pp. 394–395.

[**DArco'15**] S. D'Arco, J. A. Suul, and O. B. Fosso. "A Virtual Synchronous Machine implementation for distributed control of power converters in SmartGrids". In: *Electric Power Systems Research*, vol. 122 (2015), pp. 180–197.

[**Diez-Maroto'17**] L. Diez-Maroto, L. Vanfretti, M. S. Almas, G. M. Jónsdóttir, and L. Rouco. "A WACS exploiting generator Excitation Boosters for power system transient stability enhancement". In: *Electric Power Systems Research*, vol. 148 (2017), pp. 245–253.

[**Díez-Maroto'19**a] L. Díez-Maroto, J. Renedo, L. Rouco, and F. Fernández-Bernal. "Lyapunov stability based wide area control systems for excitation boosters in synchronous generators". In: *IEEE Transactions on Power Systems*, vol. 34. no. 1 (2019), pp. 194–204.

[**Díez-Maroto'19**b] L. Díez-Maroto, L. Rouco, and F. Fernández-Bernal. "Modeling, sizing and control of an excitation booster for enhancement of synchronous generators fault ride through capability: experimental validation". In: *IEEE Transactions on Energy Conversion*, vol. 31. no. 4 (2019), pp. 1304–1314.

[**Díez-Maroto'20**] L. Díez-Maroto, J. Renedo, L. Rouco, and F. Fernández-Bernal. "Wide area controllers for excitation boosters for transient stability improvement". In: *Electric Power Systems Research*, vol. 189. no. 106622 (2020), pp. 1–6.

[**DIgSILENT'22**] DIgSILENT. *Grid-forming Converter Templates. Droop Controlled Converter, Synchronverter, Virtual Synchronous Machine.* Tech. rep. Germany: PowerFactory - Technical Reference, 2022.

[**Du'19**] W. Du, K. P. Schneider, F. K. Tuffner, Z. Chen, and R. H. Lasseter. "Modeling of Grid-Forming Inverters for Transient Stability Simulations of an all Inverter-based Distribution System". In: *2019 IEEE Power & Energy Society Innovative Smart Grid Technologies Conference (ISGT)*. Feb. 2019, pp. 1–5. DOI: 10.1109/ISGT.2019.8791620.

[**Eskandari'20**] M. Eskandari and A. V. Savkin. "On the impact of fault ride-through on transient stability of autonomous microgrids: Nonlinear analysis and solution". In: *IEEE Transactions on Smart Grid* (2020), pp. 1–12. DOI: 10.1109/TSG.2020.3030015.

[**Fan'22**a] B. Fan, T. Liu, F. Zhao, H. Wu, and X. Wang. "A review of current-limiting control of grid-forming inverters under symmetrical disturbances". In: *IEEE Open Journal of Power Electronics*, vol. 3. no. xxx (2022), pp. 955–969. DOI: 10.1109/OJPEL.2022.3227507.

[**Fan'22**b] B. Fan and X. Wang. "Fault recovery analysis of grid-forming inverters with priority-based current limiters". In: *IEEE Transactions on Power Systems* (2022), pp. 1–10. DOI: 10.1109/TPWRS.2022.3221209.

[**Fuchs'14**] A. Fuchs, M. Imhof, T. Demiray, and M. Morari. "Stabilization of Large Power Systems Using VSC–HVDC and Model Predictive Control". en. In: *IEEE Transactions on Power Delivery*, vol. 29. no. 1 (Feb. 2014), pp. 480–488. DOI: 10.1109/TPWRD.2013.2280467.

[**Gomez-Exposito'17**] A. Gomez-Exposito, A. J. Conejo, and C. Canizares. *Electric Energy Systems: Analysis and Operation*. en. CRC Press, Dec. 2017.

[**Groß'19**] D. Groß, M. Colombino, J.-S. Brouillon, and F. Dörfler. "The Effect of Transmission-Line Dynamics on Grid-Forming Dispatchable Virtual Oscillator Control". en. In: *IEEE Transactions on Control of Network Systems*, vol. 6. no. 3 (Sept. 2019), pp. 1148–1160. DOI: 10.1109/TCNS.2019.2921347.

[**Guerrero'11**] J. M. Guerrero, J. C. Vasquez, J. Matas, L. G. de Vicuna, and M. Castilla. "Hierarchical Control of Droop-Controlled AC and DC Microgrids—A General Approach Toward Standardization". In: *IEEE Transactions on Industrial Electronics*, vol. 58. no. 1 (Jan. 2011), pp. 158–172. DOI: 10.1109/TIE.2010.2066534.

[**Guerrero'13**a] J. M. Guerrero, M. Chandorkar, T.-L. Lee, and P. C. Loh. "Advanced Control Architectures for Intelligent Microgrids—Part I: Decentralized and Hierarchical Control". In: *IEEE Transactions on Industrial Electronics*, vol. 60. no. 4 (Apr. 2013), pp. 1254–1262. DOI: 10.1109/TIE.2012.2194969.

[**Guerrero'13**b] J. M. Guerrero, P. C. Loh, T.-L. Lee, and M. Chandorkar. "Advanced Control Architectures for Intelligent Microgrids—Part II: Power Quality, Energy Storage, and AC/DC Microgrids". In: *IEEE Transactions on Industrial Electronics*, vol. 60. no. 4 (Apr. 2013), pp. 1263–1270. DOI: 10.1109/TIE.2012.2196889.

[**Haque'04**] M. H. Haque. "Improvement of first swing stability limit by utilizing full benefit of shunt FACTS devices". In: *IEEE Transactions on Power Systems*, vol. 19. no. 4 (2004), pp. 1894–1902.

[**Hatziargyriou'20**a] N. Hatziargyriou, J. V. Milanović, C. Rahmann, V. Ajjarapu, C. Canizares, I. Erlich, D. Hill, I. Hiskens, I. Kamwa, B. Pal, P. Pourbeik, J. J. Sanchez-Gasca, A. Stanković, T. Van Cutsem, V. Vittal, and C. Vournas. "Definition and classification of power system stability - revisited and extended". In: *IEEE Transactions on Power Systems*, vol. doi: 10.1109/TPWRS.2020.3041774 (2020), pp. 1–12.

[**Hatziargyriou'20**b] N. Hatziargyriou, J. Milanović, C. Rahmann, V. Ajjarapu, C. Cañizares, I. Erlich, D. Hill, I. Hiskens, I. Kamwa, B. Pal, P. Pourbeik, J. Sanchez- Gasca, A. Stanković, T. Van Cutsem, V. Vittal, and C. Vournas. *Stability definitions and characterization of dynamic behavior in systems with high penetration of power electronic interfaced technologies*. English. Tech. rep. IEEE / F.R.S.-FNRS - Fonds de la Recherche Scientifique, Apr. 2020.

[**He'22**] X. He, S. Pan, and H. Geng. "Transient Stability of Hybrid Power Systems Dominated by Different Types of Grid-Forming Devices". In: *IEEE Transactions on Energy Conversion*, vol. 37. no. 2 (June 2022), pp. 868–879. DOI: 10.1109/TEC.2021.3113399.

[**Kanakesh'21**] V. K. Kanakesh and Y. Guangya. *Effects of current limit for grid forming converters on transient stability: analysis and solution.* arXiv preprint, June 2021. URL: http://arxiv.org/abs/2106.13555 (visited on 12/28/2023).

[**Kanakesh'23**] V. K. Kanakesh, S. Mohan, G. Yang, and W. Xu. "Comparative assessment of typical control realizations of grid forming converters based on their voltage source behaviour". en. In: *Energy Reports*, vol. 9 (Dec. 2023), pp. 6042–6062. DOI: 10.1016/j.egyr.2023.05.073.

[**Kundur'04**] P. Kundur, J. Paserba, V. Ajjarapu, G. Andersson, A. Bose, C. Canizares, N. Hatziargyriou, D. Hill, A. Stankovic, C. Taylor, T. Van Cutsem, and V. Vittal. "Definition and classification of power system stability IEEE/CIGRE joint task force on stability terms and definitions". In: *IEEE Transactions on Power Systems*, vol. 19. no. 3 (2004), pp. 1387–1401.

[**Kundur'94**] P. Kundur. *Power system stability and control.* McGraw Hill Education, 1994.

[**L2EP-LILLE'20**] L2EP-LILLE. "VSC_Lib: Grid forming models for Matlab/SimPowerSystem". In: vol. https://github.com/l2ep-epmlab/ (accessed 08-07-2020) (2020).

[**Laba'23**] Y. Laba, A. Bruyère, F. Colas, and X. Guillaud. "Virtual Power-Based Technique for Enhancing the Large Voltage Disturbance Stability of HV Grid-Forming Converters". en. In: *2023 25th European Conference on Power Electronics and Applications (EPE'23 ECCE Europe).* Aalborg, Denmark: IEEE, Sept. 2023, pp. 1–8. DOI: 10.23919/EPE23ECCEEurope58414.2023.10264486.

[**Lee'86**] D. C. Lee and P. Kundur. "Advanced excitation controls for power system stability enhancement". In: *CIGRE.* Vol. 38-01. 1986.

[**Markovic'21**] U. Markovic, O. Stanojev, P. Aristidou, E. Vrettos, D. Callaway, and G. Hug. "Understanding Small-Signal Stability of Low-Inertia Systems". In: *IEEE Transactions on Power Systems*, vol. 36. no. 5 (Sept. 2021), pp. 3997–4017. DOI: 10.1109/TPWRS.2021.3061434.

[**Mauricio'20**] J. M. Mauricio and A. E. Leon. "Improving Small-Signal Stability of Power Systems With Significant Converter-Interfaced Generation". In: *IEEE Transactions on Power Systems*, vol. 35. no. 4 (July 2020), pp. 2904–2914. DOI: 10.1109/TPWRS.2020.2968422.

[**Milano'10**] F. Milano. *Power System Modelling and Scripting*. Power Systems ISSN 1612-1287. Berlin, Heidelberg: Springer, 2010. DOI: 10.1007/978-3-642-13669-6.

[**Milano'18**] F. Milano, F. Dörfler, G. Hug, D. J. Hill, and Verbǐc. "Foundations and challenges of low-inertia systems". In: *Proc. Power systems computation conference (PSCC), dublin, ireland*. 2018, pp. 1–25.

[**Mo'17**] O. Mo, S. D'Arco, and J. A. Suul. "Evaluation of Virtual Synchronous Machines With Dynamic or Quasi-Stationary Machine Models". en. In: *IEEE Transactions on Industrial Electronics*, vol. 64. no. 7 (July 2017), pp. 5952–5962. DOI: 10.1109/TIE.2016.2638810.

[**Ogata'10**] K. Ogata. *Ingeniería de control moderna*. Quinta edición. Madrid (España): Pearson Education, 2010.

[**Olivares'14**] D. E. Olivares, A. Mehrizi-Sani, A. H. Etemadi, C. A. Canizares, R. Iravani, M. Kazerani, A. H. Hajimiragha, O. Gomis-Bellmunt, M. Seedifard, R. Palma-Behnke, A. Jiménez-Estévez, and N. Hatziargyriou. "Trends in microgrid control". In: *IEEE Transactions on Smart Grid*, vol. 5. no. 4 (2014), pp. 1905–1919.

[**Pagola'06**] F. L. Pagola. *Regulación automática: 25*. Español. Madrid (España): Universidad Pontificia Comillas, 2006.

[**Pan'19**] D. Pan, X. Wang, F. Liu, and R. Shi. "Transient stability impact of reactive power control on grid-connected converters". In: *Proc. IEEE energy conversion congress and exposition (ECCE), baltimore, MD, USA*. 2019, pp. 4311–4316.

[**Pan'20**] D. Pan, X. Wang, F. Liu, and R. Shi. "Transient stability of voltage-source converters with grid-forming control: A design-oriented study". In: *IEEE Journal of Emerging and Selected Topics in Power Electronics*, vol. 8. no. 2 (2020), pp. 1019–1033.

[**Paolone'20**] M. Paolone, T. Gaunt, X. Guillaud, M. Liserre, S. Meliopoulos, A. Monti, T. Van Cutsen, V. Vittal, and C. Vournas. "Fundamentals of power systems modelling in the presence of converter-interfaced generation". In: *Electric Power Systems Research*, vol. 189. no. 106811 (2020), pp. 1–33.

[**Paquette'15**] A. D. Paquette and D. M. Divan. "Virtual impedance current limiting for inverters in microgrids with synchronous generators". In: *IEEE Transactions on Industry Applications*, vol. 51. no. 2 (2015), pp. 1630–1638. DOI: 10.1109/TIA.2014.2345877.

[**Pereira'20**] G. S. Pereira, V. Costan, A. Bruyére, and X. Guillaud. "Simplified approach for frequency dynamics assessment of 100% power electronics-based systems". In: *Electric Power Systems Research*, vol. 188. no. 106551 (2020), pp. 1–8.

[**Qoria'18**a] T. Qoria, Q. Cossart, C. Li, X. Guillaud, F. Colas, F. Gruson, and X. Kestelyn. *WP3-Control and Operation of a Grid with 100% Converter-Based Devices. Deliverable 3.2: Local control and simulation tools for large transmission systems*. Tech. rep. MIGRATE Project, 2018.

[**Qoria'18**b] T. Qoria, F. Gruson, F. Colas, X. Guillaud, M.-S. Debry, and T. Prevost. "Tuning of cascaded controllers for robust grid-forming Voltage Source Converter". In: *Proc. Power systems computation conference (PSCC), dublin, ireland*. 2018, pp. 1–8.

[**Qoria'19**] T. Qoria, F. Gruson, F. Colas, G. Denis, T. Prevost, and X. Guillaud. "Inertia effect and load sharing capability of grid forming converters connected to a transmission grid". In: *15th IET int. Conf. on AC and DC power transmission (ACDC), coventry, UK*. 2019, pp. 1–6.

[**Qoria'20**a] T. Qoria, F. Gruson, F. Colas, G. Denis, T. Prevost, and X. Guillaud. "Critical clearing time determination and enhancement of grid-forming converters embedding virtual impedance as current limitation algorithm". In: *IEEE Journal of Emerging and Selected Topics in Power Electronics*, vol. 8. no. 2 (2020), pp. 1050–1061.

[**Qoria'20**b] T. Qoria, F. Gruson, F. Colas, X. Kestelyn, and X. Guillaud. "Current limiting algorithms and transient stability analysis of grid-forming VSCs". In: *Electric Power Systems Research*, vol. 189. no. 106726 (2020), pp. 1–8.

[**Qoria'20**c] T. Qoria, E. Rokrok, A. Bruyere, B. Francois, and X. Guillaud. "A PLL-Free grid-forming control with decoupled functionalities for high-power transmission system applications". In: *IEEE access* no. 106765 (2020), pp. 197363–197378.

[**Qoria'22**] T. Qoria, H. Wu, X. Wang, and I. Colak. "Variable virtual impedance-based overcurrent protection for grid-forming inverters: Small-signal, large-signal analysis and improvement". In: *IEEE Transactions on Smart Grid* (2022), pp. 1–1. DOI: 10.1109/TSG.2022.3232987.

[**Ramasubramanian'18**] D. Ramasubramanian, E. Farantatos, S. Ziaeinejad, and A. Mehrizi-Sani. "Operation paradigm of an all converter interfaced generation bulk power system". en. In: *IET Generation, Transmission & Distribution*, vol. 12. no. 19 (2018), pp. 4240–4248. DOI: 10.1049/iet-gtd.2018.5179.

[**Renedo'17**] J. Renedo, A. García-Cerrada, and L. Rouco. "Reactive-power coordination in VSC-HVDC multi-terminal systems for transient stability improvement". In: *IEEE Transactions on Power Systems*, vol. 32. no. 5 (2017), pp. 3758–3767.

[**Rocabert'12**] J. Rocabert, A. Luna, F. Blaabjerg, and P. Rodríguez. "Control of power converters in AC microgrids". In: *IEEE Transactions on Power Electronics*, vol. 27. no. 11 (2012), pp. 4734–4749.

[**Rodríguez-Cabero'20**] A. Rodríguez-Cabero, J. Roldán-Pérez, and M. Prodanovic. "Virtual impedance design considerations for virtual synchronous machines in weak grids". In: *IEEE Journal of Emerging and Selected Topics in Power Electronics*, vol. 8. no. 2 (2020), pp. 1477–1489. DOI: 10.1109/JESTPE.2019.2912071.

[**RodriguezA'21**] J. L. Rodriguez Amenedo, S. A. Gomez, J. Alonso-Martinez, and M. G. De Armas. "Grid-Forming Converters Control Based on the Reactive Power Synchronization Method for Renewable Power Plants". In: *IEEE Access*, vol. 9 (2021), pp. 67989–68007. DOI: 10.1109/ACCESS.2021.3078078.

[**Rokrok'20**] E. Rokrok, T. Qoria, A. Bruyere, B. Francois, and X. Guillaud. "Classification and dynamic assessment of droop-based grid-forming control schemes: Application in HVDC systems". In: *Electric Power Systems Research*, vol. 189. no. 106765 (2020), pp. 1–7.

[**Rokrok'21**] E. Rokrok, T. Qoria, A. Bruyere, B. Francois, and X. Guillaud. "Transient stability assessment and enhancement of grid-forming converters embedding current reference saturation as current limiting strategy". In: *IEEE Trans. Power Systems* (2021), pp. 1–12. DOI: 10.1109/TPWRS.2021.3107959.

[**Roldán-Pérez'19**] J. Roldán-Pérez, A. Rodríguez-Cabero, and M. Prodanovic. "Design and analysis of virtual synchronous machines in inductive and resistive weak grids". In: *IEEE Transactions on Energy Conversion*, vol. 34. no. 2 (2019), pp. 1818–1828.

[**Sadeghkhani'17**] I. Sadeghkhani, M. E. Hamedani Golshan, J. M. Guerrero, and A. Mehrizi-Sani. "A current limiting strategy to improve fault ride-through of inverter interfaced autonomous microgrids". In: *IEEE Transactions on Smart Grid*, vol. 8. no. 5 (2017), pp. 2138–2148. DOI: 10.1109/TSG.2016.2517201.

[**Shuai'18**] Z. Shuai, C. Shen, X. Liu, Z. Li, and Z. J. Shen. "Transient angle stability of virtual synchronous generators using lyapunov's direct method". In: *IEEE Transactions on Smart Grid*, vol. 10. no. 4 (2018), pp. 4648–4661.

[**Si'23**] W. Si and J. Fang. "Transient Stability Improvement of Grid-Forming Converters Through Voltage Amplitude Regulation and Reactive Power Injection". en. In: *IEEE Transactions on Power Electronics*, vol. 38. no. 10 (Oct. 2023), pp. 12116–12125. DOI: 10.1109/TPEL.2023.3290170. URL: https://ieeexplore.ieee.org/document/10167833/ (visited on 01/24/2024).

[**Sigrist'12**] L. Sigrist, I. Egido, and L. Rouco. "A Method for the Design of UFLS Schemes of Small Isolated Power Systems". In: *IEEE Transactions on Power Systems*, vol. 27. no. 2 (May 2012), pp. 951–958. DOI: 10.1109/TPWRS.2011.2174448.

[**Sigrist'15**] L. Sigrist, F. Echavarren, L. Rouco, and P. Panciatici. "A fundamental study on the impact of HVDC lines on transient stability of power systems". en. In: *2015 IEEE Eindhoven PowerTech*. Eindhoven, Netherlands: IEEE, June 2015, pp. 1–6. DOI: 10.1109/PTC.2015.7232474.

[**Singh'11**] M. Singh and S. Santoso. *Dynamic Models for Wind Turbines and Wind Power Plants*. en. Technical Report NREL/SR-5500-52780, 1028524. National Renewable Energy Lab. (NREL), Golden, CO (United States), Oct. 2011, NREL/SR–5500–52780, 1028524. DOI: 10.2172/1028524.

[**Tielens'16**] P. Tielens and D. Van Hertem. "The relevance of inertia in power systems". en. In: *Renewable and Sustainable Energy Reviews*, vol. 55 (Mar. 2016), pp. 999–1009. DOI: 10.1016/j.rser.2015.11.016.

[**Wang'15**] X. Wang, Y. W. Li, F. Blaabjerg, and P. C. Loh. "Virtual-Impedance-Based Control for Voltage-Source and Current-Source Converters". In: *IEEE Transactions on Power Electronics*, vol. 30. no. 12 (Dec. 2015), pp. 7019–7037. DOI: 10.1109/TPEL.2014.2382565.

[**Wang'20**] Y. Wang, Y. Zhou, K. Zhou, T. Wang, Z. Xu, and X. Li. "Study on Transient Stability of Power System Containing Non-Synchronous Machine Sources Based on PSCAD/EMTDC". In: *2020 4th International Conference on HVDC (HVDC)*. Nov. 2020, pp. 276–281. DOI: 10.1109/HVDC50696.2020.9292769.

[**Watson'19**] J. Watson, Y. Ojo, I. Lestas, and C. Spanias. "Stability of power networks with grid-forming converters". In: *2019 IEEE Milan PowerTech*. June 2019, pp. 1–6. DOI: 10.1109/PTC.2019.8810506.

[**Xin'16**] H. Xin, L. Huang, L. Zhang, Z. Wang, and J. Hu. "Synchronous instability mechanism of P-f droop-controlled voltage source converter caused by current saturation". In: *IEEE Transactions on Power Systems*, vol. 31. no. 6 (2016), pp. 5206–5207.

[**Xiong'21**a] X. Xiong, C. Wu, P. Cheng, and F. Blaabjerg. "An optimal damping design of virtual synchronous generators for transient stability enhancement". In: *IEEE Transactions on Power Electronics*, vol. 36. no. 10 (2021), pp. 11026–11030.

[**Xiong'21**b] X. Xiong, C. Wu, and F. Blaabjerg. "An Improved Synchronization Stability Method of Virtual Synchronous Generators Based on Frequency Feedforward on Reactive Power Control Loop". en. In: *IEEE Transactions on Power Electronics*, vol. 36. no. 8 (Aug. 2021), pp. 9136–9148. DOI: 10.1109/TPEL.2021.3052350. URL: https://ieeexplore.ieee.org/document/9328607/ (visited on 01/24/2024).

[**Yu'16**] M. Yu, A. J. Roscoe, C. D. Booth, A. Dysko, R. Ierna, J. Zhu, N. Grid, and H. Urdal. "Use of an inertia-less Virtual Synchronous Machine within future power networks with high penetrations of converters". In: *2016 Power Systems Computation Conference (PSCC)*. June 2016, pp. 1–7. DOI: 10.1109/PSCC.2016.7540926.

[**Zhang'10**] L. Zhang, L. Harnefors, and H.-P. Nee. "Power-Synchronization Control of Grid-Connected Voltage-Source Converters". In: *IEEE Transactions on Power Systems*, vol. 25. no. 2 (May 2010), pp. 809–820. DOI: 10.1109/TPWRS.2009.2032231.

[**Zhang'15**] F. Zhang, Y. Sun, L. Cheng, X. Li, J. H. Chow, and W. Zhao. "Measurement and modeling of delays in wide-area closed-loop control systems". In: *IEEE Transactions on Power Systems*, vol. 30. no. 1 (2015), pp. 2426–2433.

[**Zhao'20**a] X. Zhao and D. Flynn. "Freezing Grid-Forming Converter Virtual Angular Speed to Enhance Transient Stability Under Current Reference Limiting". In: *2020 IEEE 21st Workshop on Control and Modeling for Power Electronics (COMPEL)*. ISSN: 1093-5142. Nov. 2020, pp. 1–7. DOI: 10.1109/COMPEL49091.2020.9265733.

[**Zhao'20**b] X. Zhao and D. Flynn. "Transient Stability Enhancement with High Shares of Grid-Following Converters in a 100% Converter Grid". In: *2020 IEEE PES Innovative Smart Grid Technologies Europe (ISGT-Europe)*. Oct. 2020, pp. 594–598. DOI: 10.1109/ISGT-Europe47291.2020.9248794.

[**Zhao'22**] X. Zhao and D. Flynn. "Grid-Forming Converter Angular Speed Freezing to Enhance Transient Stability in 100% Grid-Forming and Mixed Power Systems". en. In: *IFAC-PapersOnLine*, vol. 55. no. 9 (2022), pp. 425–430. DOI: 10.1016/j.ifacol.2022.07.074.

[**Zhong'11**] Q.-C. Zhong and G. Weiss. "Synchronverters: Inverters that mimic synchronous generators". In: *IEEE Transactions on Industrial Electronics*, vol. 58. no. 4 (2011), pp. 1259–1267.

Appendix A

Test systems

A.1 GFM-VSC connected to an infinite grid

Figure A.1 illustrates a GFM-VSC connected to an infinite bus.

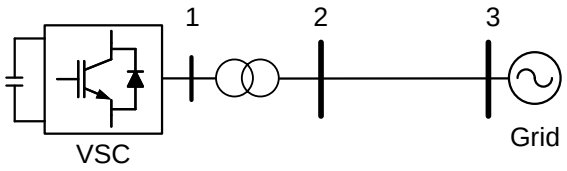

Figure A.1: GFM-VSC connected to an infinite bus.

Figure A.2 illustrates the equivalent model of a GFM-VSC connected to the grid. Data of the grid-forming VSC-1 are provided in Table A.1. Nominal voltage and frequency of the system are 220 kV and 50 Hz, respectively. Parameters of line 2-3 are $r = 0.01$ pu, $x = 0.1$ pu (base values for pu: 220 kV and 100 MVA).

- Load at the bus Nº 2: 5 MW.

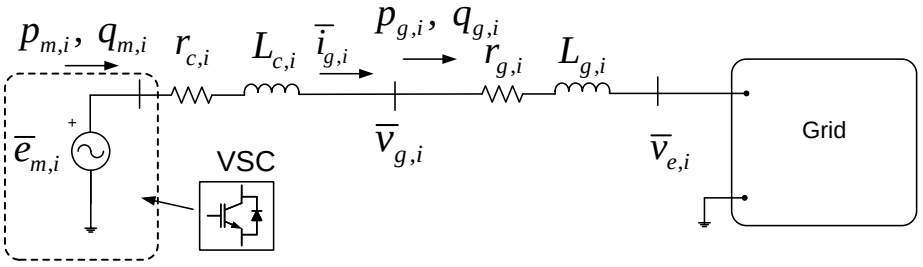

Figure A.2: Equivalent model of a Grid-Forming Voltage Source Converter GFM-VSC connected to the grid.

Table A.1: Parameters of the VSCs

Parameters VSC's rating are base values for pu	
Rating VSC, DC voltage, AC voltage	100 MVA, ±640 kV, 400 kV
Max. current	1.20 pu (equal priority for $d-q$ axes)
Transformer resistance ($r_{c,i}$)/reactance ($x_{c,i}$) (100 MVA 400/320 kV transformer)	0.005 pu / 0.15 pu
Inner prop./int. control ($K_{C,P,i}/K_{C,I,i}$)	1.0027 pu / 1.0743 pu/s
Emulated inertia ($H_{GFM,i}$) the VSC	5 s
Primary freq. controller ($K_{PFR,i}/T_{PFR,i}$)	20 pu / 1 s
Primary freq. controller limit ($\Delta p_{g,i}^{max}$)	1 pu

A.2 Kundur's two-area test system

Kundur's two-area test system in Figure A.3 has been used to validate the performance of the control strategies in Chapters 4, 5 and 6 (FVB strategies, HCL strategies and P strategies). The Kundur's two-area test system [**Kundur'94**] is implemented with 100% of grid-forming VSC-based generation by means of electromagnetic-type simulation in Matlab + Simulink + SimPowerSystems. Electromagnetic-type models (EMT) have been used to represent the elements of the power system. Specifically, converters have been modelled using electromagnetic-type averaged models, including converter limitations such as current and voltage limits. System elements such as lines and loads, and controllers have been simulated in detail whereas

converters have been modelled using electromagnetic-type averaged models, including converter limitations such as current and voltage limits.

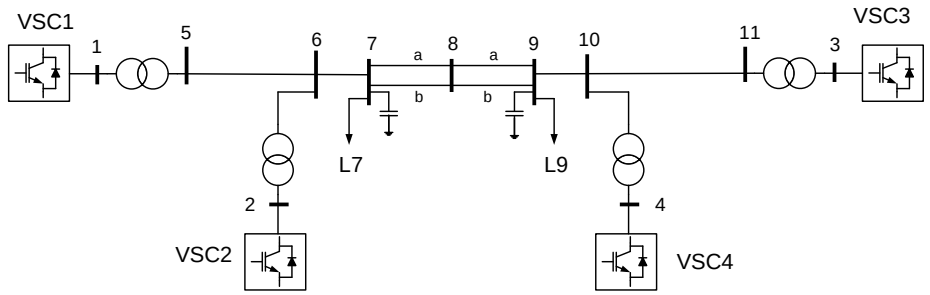

Figure A.3: Kundur's two-area test system with 100% GFM-VSC-based generation.

Table A.2 shows the results of the steady-state initial operating point.

Table A.2: Initial operating point.

VSC	$v_{g,i}$ (pu)	$\delta_{g,i}$ (deg)	$P_{g,i}$ (MW)	$Q_{g,i}$ (MVAr)
VSC 1	1.0475	0.44	693.00	0.00
VSC 2	1.0309	0.45	693.00	90.00
VSC 3	0.9900	0.00	642.60	-69.93
VSC 4	0.9738	0.16	693.00	180.00

Table A.4 depicts the data of the grid-forming VSCs. The data of the original two-area Kundur's test system can be found in [**Kundur'94**]. In this work the same conditions of [**Ávila-Martínez'22**] were considered: (Load at bus 7: 917 MW & 100 MVAr; load at bus 9: 1817 MW & 100 MVAr). Nominal frequency is 50 Hz.

Table A.3: Fault description

	Short circuit at line $i-j$	close to bus	clearing
Fault I	7-8a	7	Disconnect 7-8a
Fault II	5-6	5	short circuit cleared (line not disconnected)
Fault III	10-11	11	short circuit cleared (line not disconnected)
Fault IV	8-9a	8	Disconnect 8-9a

Data of the grid-forming VSCs are provided in Table A.4. Data of the original two-area Kudur's test system can be found in [**Kundur'94**]. Nominal voltage of the transmission grid and the nominal frequency (230 kV and 60 Hz, respectively) were changed to 220 kV and 50 Hz in this study. Loads were modelled as constant impedances for dynamic simulation. Besides, a critical case for transient stability was achieved by increasing the power transfer from Area 1 to Area 2:

- Loads: bus 7: 917 MW & 100 MVAr; bus 9: 1817 MW & 100 MVAr.

Figure A.4 presents the equivalent model of a Grid-Forming Voltage Source Converter (GFM-VSC) connected to the rest of the system through an LC filter used in all converters of the Kudur's two-area test system.

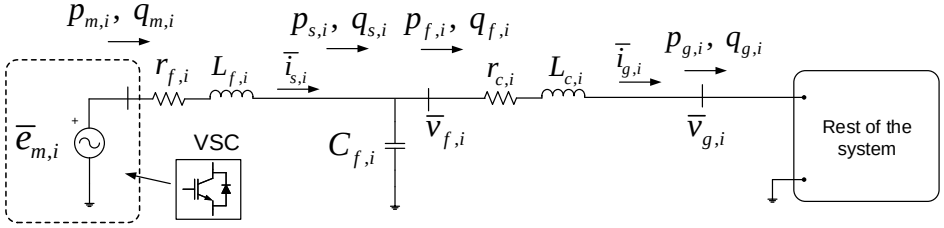

Figure A.4: Equivalent model of a Grid-Forming Voltage Source Converter GFM-VSC connected to the res of the system via a LC filter

Parameters of the FVBs

- FVB-L: $v_{A,i} = 0.5$ pu, $v_{B,i} = 0.9$ pu, $\omega_{thres,i} = 10^{-3}$ pu, $\Delta v_{f,i}^{max} = 0.15$ pu.
- FVB-WACS: $K_{FVB,i} = 50$ pu, $T_{f,i} = 0.1$ s, $T_{W,i} = 10$ s, $\Delta v_{f,i}^{max} = 0.15$ pu and $\epsilon_i = 10^{-3}$ pu.

Parameters of the current limiters

- CSA: $i_{s,i}^{max} = 1.25$ pu (equal priority for $d-q$ axes).
- VI-CL: $i_{VI,i}^{max} = 1.0$ pu, $k_{p_{rVI}} = 0.098$ pu, $\sigma_{x/r} = 5$..
- HCL: Parameters of CSA and VI-CL are used.

Parameters of the TSPs

- TSP-L: $v_{A,i} = 0.50$ pu, $v_{B,i} = 0.9$ pu, $\omega_{thres,i} = 10^{-3}$ pu, $\Delta p_{g,i}^{max} = 0.15$ pu.
- TSP-WACS: $K_{TSP,i} = 100$ pu, $T_{f,i} = 0.1$ s, $T_{W,i} = 10$ s, $\Delta p_{g,i}^{max} = 0.15$ pu and $\epsilon_i = 10^{-3}$ pu.
- TSP-TDM: $K_{TDM,i} = 100$ pu, $T_{f,i} = 0.1$ s, $T_{W,i} = 10$ s, $\Delta p_{g,i}^{max} = 0.15$ pu and $\epsilon_i = 10^{-3}$ pu.

Table A.4: Parameters of the VSCs

Parameters VSC's rating are base values for pu	
Rating VSC, DC voltage, AC voltage	900 MVA, ±320 kV, 300 kV
Max. current	1.25 pu (equal priority for $d-q$ axes)
Max. modulation index ($m_i^{max} = \sqrt{\frac{3}{2}} \cdot \frac{V_{dc,B}}{2V_{ac,B}}$)	1.31 pu
Series filter resistance ($r_{f,i}$)/reactance ($x_{f,i}$)	0.005 pu / 0.15 pu
Shunt filter capacitance ($C_{f,i}$)	0.0660 pu
Transformer resistance ($r_{c,i}$)/reactance ($x_{c,i}$) (900 MVA 300/220 kV transformer)	0.005 pu / 0.15 pu
Inner prop./int. control ($K_{C,P,i}/K_{C,I,i}$)	0.73 pu / 1.19 pu/s
Outer prop./int. control ($K_{V,P,i}/K_{V,I,i}$)	0.52 pu / 1.16 pu/s
Virtual transient resistance ($r_{V,i}/T_{VR,i}$)	0.09 pu / 0.0167 s
Emulated inertia ($H_{GFM,i}$) of VSCs 1 and 2	4.5 s / 4.5 s
Emulated inertia ($H_{GFM,i}$) of VSCs 3 and 4	4.175 s / 6.175 s
Primary freq. controller gain. ($D_{VSC,i}$)	20 pu